

# Morphological Analysis of H I Features. II. Wavelet-Based Multifractal Formalism

A. Khalil<sup>1,2,3</sup>, G. Joncas<sup>1</sup>, F. Nekka<sup>4,5</sup>, P. Kestener<sup>6</sup>, A. Arneodo<sup>7</sup>

akhalil@jax.org

## ABSTRACT

The 2D Wavelet Transform Modulus Maxima (WTMM) method is used to obtain quantitative information on the fractal/multifractal nature and anisotropic structure of Galactic atomic hydrogen (H I) from the Canadian Galactic Plane Survey. Five mosaics were analyzed in the second quadrant of the Milky Way, corresponding to the Local, Perseus, and Outer spiral arms, as well as two “inter-arm” regions located between these three spiral arms. A monofractal signature is found for all five mosaics. An anisotropic signature is detected: the root mean square (rms) roughness fluctuations of the mosaics in the latitude direction differ from those in the longitude direction. This anisotropy is scale-independent for the inter-arm regions while it is scale-dependent for the spiral arms. The longitudinal matter distribution of H I structure is similar for all five mosaics while the latitudinal distribution is smoother in the spiral arms. These results hold for all physical length scales studied, from  $\sim 2$  pc in the Local arm to  $\sim 44$  pc in the Outer arm. Several hypotheses are investigated to provide a physical explanation: the scale-height gradient, the density wave, star formation activity, photo-levitation of dusty clouds, random motion of H I clouds, corrugation, and turbulence.

---

<sup>1</sup>Département de Physique, Génie Physique et d’Optique, and Observatoire du Mont-Mégantic, Université Laval, Québec, Qc, CANADA G1K 7P4

<sup>2</sup>Institute for Molecular Biophysics, The University of Maine / Jackson Laboratory, 600 Main St, Bar Harbor, ME, USA 04609

<sup>3</sup>Current Address: Department of Mathematics & Statistics, The University of Maine, Orono, ME, USA 04469

<sup>4</sup>Faculté de Pharmacie, Université de Montréal, Montréal, Qc, CANADA H3C 3J7

<sup>5</sup>Centre de Recherche en Mathématiques, Université de Montréal, Montréal, Qc, CANADA H3C 3J7

<sup>6</sup>CEA Saclay, DSM/DAPNIA/SEDI, F-91191 Gif-sur-Yvette, FRANCE

<sup>7</sup>Laboratoire de Physique, École Normale Supérieure de Lyon, 46 allée d’Italie, 69364 Lyon cédex 07, FRANCE

*Subject headings:* ISM: clouds — ISM: structure — technique: image processing  
— methods: data analysis — Galaxy: structure

## 1. INTRODUCTION

The Galactic H I has a very complex structure. At small scales, around singular objects (WR stars, SNRs, and H II regions), the H I is driven by winds, dissociation, and shock fronts which induce chaotic, filamentary structures of varying complexity (Khalil, Joncas & Nekka (2004), henceforth called Paper I). At the largest scale, the H I is approximately axisymmetric in longitude with a vertical distribution (along  $b$ ) often characterized by a Gaussian / exponential distribution (Lockman 1984), although a few localized structures like chimneys, for example, and the warp of the Galactic plane are well known (Binney & Merrifield 1998). But at the intermediate scale (e.g. portions of spiral arms), one may wonder whether the structure of the gas is affected by singular objects and/or by the push and pull of random motions and gravity on clouds or any other kinds of oscillations, i.e. corrugation (Spicker & Feitzinger 1986).

### 1.1. Fractals & Multifractals

Mandelbrot coined the term *fractal* more than twenty years ago to qualify geometrically complex objects that could be characterized by a non-integer dimension (Mandelbrot 1974a,b, 1977, 1982). A better description for these originally called “pathological mathematical monsters” (Hausdorff 1919; Besicovitch 1935) is that they possess details at every scale.

The Hausdorff dimension (Hausdorff 1919), a usually non-integer value expressing the complexity of fractal sets, is practically impossible to calculate by way of simple algorithms (see Li, Arneodo & Nekka (2004) for a review and the development of a new technique). To circumvent this difficulty, a more practical definition of the dimension of a set is generally used (Kolmogorov 1958). The fractal dimension,  $d_F$  (or capacity), can be calculated with many algorithms: box-counting algorithms<sup>1</sup>, fixed-mass and fixed-size correlation algorithms. For rough surfaces which are well described by self-affine<sup>2</sup> fractals (Mandelbrot 1977, 1982;

---

<sup>1</sup>Probably the first usual definition of box-counting dimension was given in Pontrjagin & Schnirelman (1932).

<sup>2</sup>Objects satisfying self-similarity conditions, but with different scalings in different directions, are said

Peitgen & Saupe 1988), different methods of estimating  $d_F$ , such as the perimeter-area relation, divider, box, triangle, slit-island, power spectral, variogram and distribution methods (for a thorough review, see Decoster (1999)) were shown to give different results (see Lea-Cox & Wang (1993) for a discussion). Limited resolution as well as finite-size effects are well known to introduce biases on the estimate of  $d_F$ , which are indeed method dependent (Dubuc et al. 1989; Schmittbuhl, Violette & Roux 1995; Scotti, Meneveau & Saddoughi 1995). An alternative strategy consists in computing the Hurst exponent,  $H$ , also called “roughness exponent” (Mandelbrot 1977, 1982; Feder 1988). This scaling exponent is supposed (for monofractal surfaces) to be related to the fractal dimension by  $d_F = d - H$ , where  $d$  is the Euclidean dimension of the space in which the surface is embedded. Again, many algorithms are available to estimate  $H$ : height-height correlation function, variance and power spectral methods, detrended fluctuation analysis, first-return and multi-return probability distributions (see Decoster (1999) and the references therein). But again, a number of artifacts may pollute the estimate of the roughness exponent (Schmittbuhl, Violette & Roux 1995) and the simultaneous use of different tools is highly recommended in order to appreciate in a quantitative way the level of confidence in the measured exponent.

In the nineties, the use of the fractal dimension in the study of the interstellar medium (ISM) was widespread. It has often been used to characterize the complexity of structures. Most studies on interstellar clouds show that the fractal dimension is more or less universal, with a value in the interval 2.2 to 2.5. Such studies were done for molecular clouds (Bazell & Désert 1988; Scalo 1990; Falgarone, Phillips & Walker 1991; Elmegreen & Falgarone 1996) as well as for H I (Vogelaar & Wakker 1994; Stanimirovic et al. 1998; Westpfahl et al. 1999). A universal fractal dimension can inform us on the underlying physical processes that are morphing the gas. For example, some find an analogy with the 4/3 exponent expected to characterize the dependence of the variance of pressure fluctuations with spatial separation in an atmosphere obeying Kolmogorov’s theory of incompressible, homogeneous, isotropic turbulence (Dickman, Horwath & Margulis 1990), and suggest turbulence as a major physical process involved in interstellar cloud structure (Scalo 1987; Falgarone 1989; Falgarone & Phillips 1990).

However, if one is in the presence of a multifractal geometrical object which is, simply put, a structure which is best described by a spectrum of fractal dimensions (Feder (1988); Vicsek (1989)), most methods will not detect it since generically, they can only provide the user with a single exponent. Hence, one must keep in mind that  $d_F$  and  $H$  are global quantities which do not characterize the local regularity of a signal or a surface.

---

to be self-affine.

The eighties were a very fruitful period for the development of the multifractal formalism (Parisi & Frisch 1985; Halsey et al. 1986), either by way of the so-called ( $D(h)$  or  $f(\alpha)$ ) singularity spectrum or the generalized fractal dimensions  $D_q$  (Badii & Politi 1985), with applications in physics as well as in other fundamental sciences: Feder (1988); Vicsek (1989); West (1990); Frisch (1995); Arneodo et al. (1995a); Sornette (2000).

Chappell & Scalo (2001) used a box-counting multifractal formalism to analyze several molecular cloud regions using IRAS maps. Since multifractal processes are likely to be related to multiplicative cascades, a multifractal signature can be interpreted as evidence of a hierarchical structure. Such evidence would be a confirmation of the widely accepted hypothesis that molecular clouds are “clumpy” (large clumps are divided into smaller clumps). The box-counting technique used by Chappell & Scalo (2001) was developed for the analysis of multifractal singular measures. However, since the H I is diffuse and distributed everywhere in the Galactic disk, it is more likely to be considered as a “continuous” mathematical function whose graph defines a rough surface. As pedagogically described by Muzy, Bacry & Arneodo (1994), the box-counting technique is not appropriate to analyze continuous functions (it actually yields a trivial estimate of the scaling exponents  $\alpha = d$ ) and one must use instead wavelet techniques where the analyzing wavelets will play the role of “generalized oscillating boxes”.

## 1.2. The Wavelet Transform and the WTMM Method

Introduced by Morlet and Grossman for the analysis of seismic signals (Grossmann & Morlet 1984; Goupillaud, Grossmann, & Morlet 1984), the wavelet transform (WT) is a mathematical tool consisting in the decomposition of a signal on a set of functions characterized by parameters of position and scale. For the study of the ISM, the WT has been used as an analysis tool (Gill & Henriksen 1990; Gill 1993; Langer, Wilson & Anderson 1993), a filtering method, (Abergel et al. 1996; Miville-Deschênes et al. 2003), and for image reconstruction (Maisinger, Hobson & Lasenby 2003).

The term “mathematical microscope” was coined by Arneodo et al. (1995a) to describe the advantages of the multi-scale analysis of the WT coupled with the positional information, making it the perfect tool to analyze the scale-invariance properties of fractal objects (Arneodo, Grasseau & Holschneider 1988; Arneodo 1996; Flandrin, Abry & Goncalvès 2002).

The Wavelet-Transform Modulus Maxima (WTMM) method is a wavelet-based multifractal formalism introduced by Arneodo, in collaboration with Bacry and Muzy (Muzy, Bacry & Arneodo 1991; Bacry, Muzy & Arneodo 1993; Muzy, Bacry & Arneodo 1993, 1994;

Arneodo, Bacry & Muzy 1995), where the different dilations of the analyzing wavelet act as “generalized oscillating boxes” to reveal quantitative information at every scale considered. Replacing the boxes used in the standard multifractal formalism by wavelets, gets rid of possible smooth behavior that either mask singularities or perturb the estimation of their strength. The other fundamental advantage of using wavelets is that the skeleton defined by the wavelet transform modulus maxima (Mallat & Zhong 1992; Mallat & Hwang 1992) provides an adaptive space-scale partitioning from which one can extract the  $D(h)$  singularity spectrum via the scaling exponents  $\tau(q)$  of some partition functions defined from the WT skeleton (see §3.3). For practical purposes, the WTMM method does not have the drawbacks of the structure function approach (Monin & Yaglom 1975; Frisch 1995) or of the box-counting techniques. While the latter only applies to singular measures, the former generally fails to fully characterize the multifractal properties since from the scaling behavior of the positive  $q$ -order moments of the increments of the function under consideration, only the strongest singularities can be captured (Muzy, Bacry & Arneodo 1993, 1994; Arneodo, Bacry & Muzy 1995). Applications of the WTMM method to 1D signals have already provided insight into a wide variety of problems (Arneodo et al. 1995a, 2002).

The WTMM method was generalized from 1D to 2D in Arneodo, Decoster & Roux (1999, 2000) and Decoster, Roux & Arneodo (2000), where the formalism was first developed and tested on isotropic and anisotropic monofractal and multifractal rough surfaces, and where the possible applications for edge detection and de-noising were presented. In Roux, Arneodo & Decoster (2000), the authors analyzed high-resolution (LANDSAT) satellite images of (earth) cloud structure, where the intermittent nature of the clouds confirmed the relevance of the multifractal description. Furthermore, the 2D WTMM method proved very efficient to characterize the anisotropic structure induced by the convective rolls in the clouds. The detection and characterization of anisotropic structures will be discussed in great detail in the present work.

### 1.3. Application of the 2D WTMM Method to H I

This paper presents the results of an intermediate-scale structural analysis of H I in the Galactic Plane using the 2D WTMM method. A region of about 45 by 8 degrees was covered in the analysis, with five different collapsed velocity intervals corresponding to the Local, Perseus and Outer Arms and to the two “inter-arm” regions in between. Our objective is to obtain a quantitative characterization of the fractal, multifractal, and anisotropic properties of the internal structure of the H I analyzed in both spiral and inter-arms, and then to draw conclusions on the turbulent nature and stratified structure of the gas. A further goal is

to generate models of rough surfaces where the fractal properties as well as some structural anisotropy that we detected will be incorporated in order to “mimic” the H I as best as possible (for the range of scales studied). The work presented here aims to complement the study of Paper I, where the Metric Space Technique was used to analyze the small-scale structure of H I features associated to galactic objects of known origin. Although the two tools are very different and do not provide the same kind of output (different methods applied to different objects), we hope that both contributions will provide a better understanding of the evolution of the ISM in our Galaxy. However, one should keep in mind that any image analysis tool is subject to resolution limitations and finite-size effects. The work presented here is no exception.

The data are presented in §2. The 2D WTMM method is described in §3. The construction and analysis of synthetic isotropic monofractal and multifractal surfaces, as well as anisotropic monofractal surfaces are dealt with in §4. The results for the H I mosaics are reported in §5, while the analysis and discussion are in §6. The paper ends with the conclusion in §7.

## 2. DATA

The data come from the Canadian Galactic Plane Survey (CGPS), where the observations were taken with the Dominion Radio Astrophysical Observatory (DRAO) synthesis telescope (Penticton, BC, Canada). A detailed description of the CGPS is given in Taylor et al. (2003). The velocity channels are separated by  $0.842 \text{ km s}^{-1}$ . According to declination, the rms noise varies from 2.1 to 3.2 K in an empty channel.

The CGPS H I data cubes (193 synthesis pointings) were assembled in five large H I mosaics: the Local spiral arm, the Perseus spiral arm, the Outer arm, and two “inter-arm” regions respectively located between the Local and Perseus arm, henceforth called “Inter I”, and between the Perseus and Outer arm, henceforth called “Inter II”. The five mosaics are presented in Figure 1. These five H I column density mosaics result from the integration of the cubes over the velocity range relevant to each structure according to galactic longitude (Table 1). Unlike the Local, Inter I, and Perseus mosaics, the velocity intervals vary significantly as a function of longitude for Inter II and Outer (Simonson 1976). The arms and interarms were isolated in velocity using Simonson (1976) and longitude-velocity plots made from the Canadian Galactic Plane Survey data (Gibson & Stil 2002). Interarms boundaries were chosen when the column density was less than 20% of the peak value of the adjacent arms. This value is pretty constant for the Local arm and Inter I but varies by  $\pm 2\text{-}3\%$  around that value for the other features. The Perseus arm has a definite

gradient in  $l - v$  plots and the Outer arm has less contrast and is more “sketchy” in  $l$ ,  $b$  and  $v$  as is obvious from the many segments appearing in Table 1.

The analysis requested the mosaics to be cut-up in subregions (white boxes in Figure 1). The pattern was governed to avoid extra-galactic and galactic absorption sources, by “edge-effects”, by defects due to image construction and manipulation, and by the need to avoid artificial and anti-symmetric anisotropic signatures. A detailed discussion now follows.

Each one of the five mosaics was divided into 32 ( $1024 \times 1024$ ) overlapping sub-images. These sub-images were cut up in such a way that the border of the central  $512 \times 512$  parts of each coincided with the border of its neighbors central  $512 \times 512$  parts. Only the  $512 \times 512$  central parts are kept for analysis (edge effects), although in some cases however, portions of only 256 or 384 pixels were available (see following discussion). By proceeding in this way, we were able to cover over 90% of the mosaics with the  $1024 \times 1024$  images. Only the top, bottom, left, and right “borders” (for a total of less than 10%) of each mosaic ended up being rejected, which is where the noise level is most elevated (see Taylor et al. (2003)’s description of the CGPS).

Now, in an ideal situation, all 32 images would have been analyzed (for each mosaic). However, several locations contained absorption sources, which correspond to large negative values (in  $\text{K km s}^{-1}$ ) and affect drastically the values of the wavelet transform. The sub-images containing absorption sources were therefore systematically rejected. Some of these sources were extra-galactic, which means that the corresponding sub-regions had to be rejected for all mosaics, while some were galactic, which means that only some (closer) mosaics were affected. Not only the (negative) value of the pixels has to be taken into account as a criterion for rejection, but also the number of pixels associated to the absorption sources. For example, a single pixel with a value of  $-250 \text{ K km s}^{-1}$  does not have the same effect on the wavelet transform as an area of 25 square pixels with values in the range  $[-50, -15] \text{ K km s}^{-1}$ . Comparisons were therefore made from the analysis of synthetic surfaces with simulated absorption sources of different values and sizes in pixels, thus quantifying their effects on the wavelet analysis (data not shown). Rejection was based on these quantitative comparisons. We rejected images containing  $\gtrsim 10$  square pixel areas of negative values. The construction and analysis of synthetic surfaces generated with the aim of calibrating the present wavelet approach in terms of highly singular small structures (e.g. absorption sources), different levels of saturation (often found in scanned biomedical images), and other general image artifacts are the subject of ongoing work (Khalil 2006).

For the Inter 2 and Outer mosaics, image construction and manipulation was more complicated since in some areas, two neighboring pixels corresponded to a collapse of different velocity intervals. In some cases, this created vertical transition lines in the mosaics, which

could even be detected by visual inspection. By examining the effects that these vertical lines had on the values of the wavelet transform, it was relatively easy to decide whether to keep or reject the corresponding sub-images, and many were indeed rejected, especially for the Inter 2 mosaic. Indeed, the discontinuous nature of these vertical lines is associated to a very specific fractal parameter value, i.e., when the so-called Hölder exponent (see definition below) equals 0. An image segmentation routine was therefore performed to determine whether such discontinuities occurred and thus reject the juxtaposed sub-image accordingly. This routine was based on preliminary results showing no such discontinuities within any of original sub-images (i.e. the pre-juxtaposed images).

The rejection of sub-regions imply different coverages for each of the five mosaics. The differing coverages do not affect the large-scale analysis of the data (i.e. the anisotropy measures). They limit however our capacity to compare the sub-regions within mosaics of the comparisons of spiral arms. After rejecting the sub-regions for the reasons stated above, there remained another dilemma. By analyzing whole mosaics corresponding to Perseus, Inter 2, and Outer, one would have been analyzing the large-scale structure of the Galactic Disk itself, and not the inside structure of the Disk. Indeed, the last thing that we wanted to show was that the Galactic Plane is distributed longitudinally (i.e., that it is, in fact, a plane or a disk). Obviously, anyone can come to that conclusion simply by looking at most standard  $l$ - $b$  graphs. Instead, the goal of this paper is to show that the material “composing” the Plane is itself anisotropically distributed (and derive its fractal properties).

Therefore, by analyzing sub-regions that contained, in one sub-image, some material that belongs to the spiral (or inter) arm as well as the areas located above and/or below, one would inevitably obtain an artificial, usually anti-symmetric, anisotropic signature, since the values of the wavelet transform corresponding to the “edge”, or “border” between spiral (or inter) arm and upper and lower material would dominate the calculations. This would result in an artificial anisotropic signature and would inevitably lead one to conclude that the Galactic Plane is indeed a Disk.

Results using wavelets of different orders can be used to confirm this statement, but were not compiled nor presented in the paper<sup>3</sup>. Indeed, a few sub-areas were rejected for presenting anisotropic signatures where the results changed from the order-1 and order-3 wavelet analysis, which is interpreted as being caused by the “latitudinal gradient” from the “disk non-disk” transition. Only the sub-areas where results from the order-1 and order-3 wavelets coincided were kept, i.e., where the uncertainty intervals overlap ( $\sigma = 0.03$ ).

---

<sup>3</sup>The reader is invited to consult the several other points of discussions regarding the use of the order-1 vs. order-3 wavelets in this paper, especially the section on the DRAO noise analysis (§5.1).

So this is indeed where some subjectivity (for Perseus, Inter 2, and Outer), i.e., some a priori knowledge of the analyzed objects, was used. But this decision was made only after realizing that the analysis of whole spiral arms yielded an “artificial” anisotropic signature. More importantly, this decision ensures that the quantitative differences found between spiral and inter arm is indeed valid.

Finally, in Simonson (1976), one can note a “spur” of H I, most likely associated with the Perseus Arm. As one can see from Table 1, material associated to velocities between  $-50$  and  $-64$  km s $^{-1}$  was therefore rejected as a member of the Inter 2 mosaic.

### 3. THE 2D WAVELET-TRANSFORM MODULUS MAXIMA METHOD

The 2D WTMM method (Arneodo, Decoster & Roux 2000) is primordially a multifractal analysis tool which provides a way to estimate the so-called  $D(h)$  spectrum of singularities, i.e. the fractal (Hausdorff) dimension of the set of points in the 2D surface which are characterized by a specific local roughness (Hölder) exponent  $h$ , or, in the case of a monofractal signature, by a global Hurst exponent  $H$ . Moreover, an anisotropic structure can also be easily detected from the directional information provided by the continuous 2D wavelet transform.

Here, the wavelet transform acts as a mathematical microscope to obtain quantitative structural information (fractal, multifractal, and anisotropy) at all scales studied. In the following description of the 2D WTMM method, comments are included regarding the drawbacks of using either a box-counting multifractal formalism (Chappell & Scalo 2001), or the structure function approach (Parisi & Frisch 1985), and how the 2D WTMM method generically avoids these drawbacks.

#### 3.1. The Continuous Wavelet Transform and the Analyzing Wavelets

Let us consider two wavelets that are, respectively, the partial derivatives with respect to  $x$  and  $y$  of a 2D smoothing (Gaussian) function,

$$\phi_{\text{Gau}}(x, y) = e^{-(x^2+y^2)/2} = e^{-|\mathbf{x}|^2/2}, \quad (1)$$

namely

$$\psi_1(x, y) = \partial\phi_{\text{Gau}}(x, y)/\partial x \quad \text{and} \quad \psi_2(x, y) = \partial\phi_{\text{Gau}}(x, y)/\partial y. \quad (2)$$

For any function  $f(x, y) \in L^2(\mathbf{R})$  (where  $L^2(\mathbf{R})$  consists of all square integrable functions), the continuous wavelet transform of  $f$  with respect to  $\psi_1$  and  $\psi_2$  is expressed as a vector

(Mallat & Zhong 1992; Mallat & Hwang 1992):

$$\begin{aligned} \mathbf{T}_\psi[f](\mathbf{b}, a) &= \begin{pmatrix} T_{\psi_1}[f] = a^{-2} \int d^2\mathbf{x} \psi_1(a^{-1}(\mathbf{x} - \mathbf{b}))f(\mathbf{x}) \\ T_{\psi_2}[f] = a^{-2} \int d^2\mathbf{x} \psi_2(a^{-1}(\mathbf{x} - \mathbf{b}))f(\mathbf{x}) \end{pmatrix}, \\ &= \nabla\{T_{\phi_{\text{Gau}}}[f](\mathbf{b}, a)\} = \nabla\{\phi_{\text{Gau},\mathbf{b},a} * f\}. \end{aligned} \quad (3)$$

Thus, Eq. (3) amounts to define the 2D wavelet transform as the gradient vector of  $f(\mathbf{x})$  smoothed by dilated versions of  $\phi_{\text{Gau}}(a^{-1}\mathbf{x})$  of the Gaussian filter.

In Figures 2a and 2b are shown the first-order analyzing wavelets  $\psi_1$  and  $\psi_2$ , where the smoothing function  $\phi_{\text{Gau}}$  is the Gaussian function defined in Eq. (1). In Figures 2c and 2d are shown the third-order analyzing wavelets obtained from the Mexican hat smoothing function

$$\phi_{\text{Mex}}(\mathbf{x}) = (2 - \mathbf{x}^2)e^{-|\mathbf{x}|^2/2}. \quad (4)$$

Using higher order wavelets, where the number  $n_\phi$  of vanishing moments of  $\phi$  conditions the order of the analyzing wavelets,  $n_\psi = n_\phi + 1$ , provides the WTMM method with the capability of characterizing the roughness, not only of the function under study, but also of its derivatives (a capability that is absent from the box-counting and structure function approaches) (Muzy, Bacry & Arneodo 1993, 1994; Arneodo et al. 1995a; Arneodo, Decoster & Roux 2000). In this paper, the third-order analyzing wavelets will be used to verify the authenticity of the anisotropic signature found in the five analyzed mosaics (§5). Indeed, when using a wavelet of order  $n$ , one needs to confirm the robustness of the results by repeating the analysis with a wavelet of a superior order (e.g. order  $n + 2$ ). Therefore, if the results obtained with an order-1 wavelet are confirmed with an order-3 wavelet, then it is a confirmation of the relevance of the results. If there is a change when going from order-1 to order-3, for e.g. in the study of earth clouds in Roux, Arneodo & Decoster (2000), this means that the analyzed data (or some components, for example a polynomial or sinusoidal distribution hidden in the data) are not self-similar and that some physical phenomenon should be responsible for this departure from self-similarity (for earth clouds, it was the large-scale smooth structure of the convective rolls).

The wavelet transform can be written in terms of its modulus and argument

$$\mathbf{T}_\psi[f](\mathbf{b}, a) = (\mathcal{M}_\psi[f](\mathbf{b}, a), \mathcal{A}_\psi[f](\mathbf{b}, a)), \quad (5)$$

where

$$\mathcal{M}_\psi[f](\mathbf{b}, a) = \sqrt{(T_{\psi_1}[f](\mathbf{b}, a))^2 + (T_{\psi_2}[f](\mathbf{b}, a))^2}, \quad (6)$$

and

$$\mathcal{A}_\psi[f](\mathbf{b}, a) = \mathbf{Arg}(T_{\psi_1}[f](\mathbf{b}, a) + iT_{\psi_2}[f](\mathbf{b}, a)). \quad (7)$$

### 3.2. Global and Local Regularity Properties of Rough Surfaces: Hurst and Hölder Exponents

In this section, the term rough surface is defined, and the notions of Hurst exponent, used to characterize the global scale invariance properties of monofractal surfaces, and Hölder exponent, used to characterize the local scale invariance properties of multifractal surfaces, are also presented.

A *rough surface* refers to a surface that can be correctly described by a single-valued self-affine function satisfying:  $\forall \mathbf{x}_0 = (x_0, y_0) \in \mathbf{R}^2, \forall \mathbf{x} = (x, y) \in \mathbf{R}^2$  in the neighborhood of  $\mathbf{x}_0$ ,  $\exists H \in \mathbf{R}$ , such that, for any  $\lambda > 0$ , one has (Mandelbrot 1977, 1982; Peitgen & Saupe 1988):

$$f(x_0 + \lambda x, y_0 + \lambda^\alpha y) - f(x_0, y_0) \sim \lambda^H [f(x_0 + x, y_0 + y) - f(x_0, y_0)]. \quad (8)$$

If  $f$  is a stochastic process, then this identity holds in law for a fixed  $\lambda$  and  $\mathbf{x}_0$ . Depending on the value of  $\alpha$ ,  $f$  will display either isotropic scale invariance ( $\alpha = 1$ ) or anisotropic scale invariance ( $\alpha \neq 1$ ) (Schertzer & Lovejoy 1985, 1987; Schmittbuhl, Violette & Roux 1995; Schertzer et al. 1997). For self-affine functions (i.e. the monofractal case), the *Hurst exponent*  $H$  characterizes the global regularity of the function  $f$  under consideration. Note that if  $H < 1$  (which is the case in most applications), then  $f$  is nowhere differentiable and generally, a more singular surface  $f$  will be characterized by a smaller  $H$ . Note that an uncorrelated Brownian surface is characterized by  $H = 1/2$ . For this class of functions, the Hurst exponent is related to the usual definition of the fractal dimension  $d_f = d - H$ , where  $d$  represents the dimension of the space where the surface is embedded.

However, fractal functions often display *multi-affine* properties in the sense that their roughness fluctuates from point to point (i.e. the multifractal case) (Muzy, Bacry & Arneodo 1991, 1994; Arneodo, Bacry & Muzy 1995). The definition of the Hurst exponent in Eq. (8) must be changed in order to describe these multifractal functions, so that it becomes a local quantity  $h(\mathbf{x}_0)$  (Arneodo, Decoster & Roux 2000). We define the *Hölder exponent* (the strength of a singularity of a function  $f$  at the point  $\mathbf{x}_0$ ) by the largest exponent  $h(\mathbf{x}_0)$  such that there exists a polynomial of degree  $n < h(\mathbf{x}_0)$  and a constant  $C > 0$ , so that for any point  $\mathbf{x}$  in the neighborhood of  $\mathbf{x}_0$ , one has:

$$|f(\mathbf{x}_0) - P_n(\mathbf{x} - \mathbf{x}_0)| \leq C |\mathbf{x} - \mathbf{x}_0|^{h(\mathbf{x}_0)}. \quad (9)$$

Therefore, the roughness of  $f$  at the point  $\mathbf{x}_0$  is characterized by  $h(\mathbf{x}_0)$ . Like the Hurst exponent  $H$ , the higher the exponent  $h(\mathbf{x}_0)$ , the more regular the function  $f$ , except that the characterization is only valid for the point  $\mathbf{x}_0$ . In this work, we will mainly consider fractal functions of two variables that possess cusp singularities only. (We refer the reader to Jaffard & Meyer (1996) for rigorous mathematical results concerning 2D oscillating singularities, or

chirps.) But as previously pointed out, the situation is a little more tricky in 2D than in 1D depending whether the scale invariance is under isotropic or anisotropic dilations.

A very efficient way to perform point-wise regularity analysis is to use the wavelet transform modulus maxima (Mallat & Zhong 1992; Mallat & Hwang 1992). At a given scale  $a > 0$ , the *wavelet transform modulus maxima* (WTMM) are defined by the positions  $\mathbf{b}$  where the wavelet transform modulus  $\mathcal{M}_\psi[f](\mathbf{b}, a)$  (Eq. (6)) is locally maximum in the direction  $\mathcal{A}_\psi[f](\mathbf{b}, a)$  (Eq. (7)) of the gradient vector  $\mathbf{T}_\psi[f]$  (Eq. (5)). When analyzing rough surfaces, these WTMM lie on connected chains henceforth called *maxima chains* (Arrault et al. 1997; Arneodo, Decoster & Roux 1999, 2000). Actually, one only needs to record the position of the local maxima of  $\mathcal{M}_\psi$  along the maxima chains together with the value of  $\mathcal{M}_\psi[f]$  and  $\mathcal{A}_\psi[f]$  at the corresponding locations. At each scale  $a$ , the wavelet analysis thus reduces to store those WTMM maxima (WTMMM) only. They indicate locally the direction where the signal has the sharpest variation. These WTMMM are disposed along connected curves across scales called *maxima lines* (Arneodo, Decoster & Roux 1999, 2000). The *wavelet transform skeleton* is defined as the set of maxima lines that converge to the  $(x, y)$ -plane in the limit  $a \rightarrow 0^+$ . This WT skeleton contains a priori all the information about the local Hölder regularity properties of the function  $f$  under consideration. Indeed, one can show that along a maxima line  $\mathcal{L}_{\mathbf{x}_0}$  that points to  $\mathbf{x}_0$  in the limit  $a \rightarrow 0^+$ , the wavelet transform modulus behaves as a power law with exponent  $h(\mathbf{x}_0)$ :

$$\mathcal{M}_\psi[f][\mathcal{L}_{\mathbf{x}_0}(a)] \sim a^{h(\mathbf{x}_0)}, \quad (10)$$

provided the order of the analyzing wavelet  $n_\psi > h(\mathbf{x}_0)$ . The reader is referred to Arneodo, Decoster & Roux (2000) where the properties and behavior of the maxima lines are presented on four specific examples which clearly illustrate the singularity detection and processing ability of the continuous wavelet transform.

### 3.3. The 2D WTMM Method

Let  $f$  be a rough surface and  $S_h$  the set of all points  $\mathbf{x}$  where the Hölder exponent (Eq.(9)) of  $f$  at  $\mathbf{x}$  is  $h$ . The *singularity spectrum*  $D(h)$  of  $f$  is the function which associates with any  $h$ , the fractal dimension,  $d_F$ , of  $S_h$ :

$$D(h) = d_F\{\mathbf{x} \in \mathbf{R}^2 : h(\mathbf{x}) = h\}. \quad (11)$$

The maxima lines defined from the WTMMM computed at different scales can be used to detect the positions where singularities are located as well as the estimation of their strength  $h$  (Eq. (10)).

The characteristic feature of fractal functions is the existence of a hierarchical distribution of singularities (Arneodo et al. 1995a; Mallat 1998). Locally, the Hölder exponent  $h(\mathbf{x}_0)$  is then governed by the singularities which accumulate at  $\mathbf{x}_0$ . This results in unavoidable oscillations around the expected power-law behavior of the wavelet transform modulus along the maxima lines (Eq. (10)) (Muzy, Bacry & Arneodo 1994; Arneodo, Bacry & Muzy 1995). The estimation of the strength of a singularity located at  $\mathbf{x}_0$  is biased by the singularities located in the neighborhood of  $\mathbf{x}_0$ . Therefore, the exact determination of  $h$  from log-log plots on a finite range of scales is uncertain and must be avoided (Bacry et al. 1991; Vergasola et al. 1993). Hence, the determination of statistical quantities like the  $D(h)$  singularity spectrum (Eq. (11)) requires a method which is more feasible and more appropriate than a systematic investigation of the wavelet transform local scaling behavior along the maxima lines that define the wavelet transform skeleton.

### 3.3.1. Partition Function

The 2D WTMM method relies upon the space-scale partitioning given by the wavelet transform skeleton. This skeleton is defined by the set of maxima lines that point to the singularities of the considered function and therefore contains all the information concerning the fluctuations of point-wise Hölder regularity. Let us define  $\mathcal{L}(a)$  as the set of all maxima lines that exist at the scale  $a$  and which contain maxima at any scale  $a' \leq a$ . The WTMM method consists in defining the following partition functions directly from the WTMM that belong to the wavelet transform skeleton:

$$\mathcal{Z}(q, a) = \sum_{\mathcal{L} \in \mathcal{L}(a)} \left( \sup_{(\mathbf{x}, a') \in \mathcal{L}, a' \leq a} \mathcal{M}_\psi[f](\mathbf{x}, a') \right)^q, \quad (12)$$

where  $q \in \mathbf{R}$ . As compared to classical box-counting techniques discussed in §1 and in Chappell & Scalo (2001), the analyzing wavelet  $\psi$  plays the role of a generalized “oscillating box”, the scale  $a$  defines its size, while the WTMM skeleton indicates how to position our oscillating boxes to obtain a partition at the considered scale. Without the “sup” in equation (12), one would have implicitly considered a uniform covering with wavelets of the same size  $a$ . As emphasized for example in Muzy, Bacry & Arneodo (1994), the “sup” can be regarded as a way of defining a “Hausdorff like” scale-adaptive partition which will prevent divergences to show up in the calculation of  $\mathcal{Z}(q, a)$  for  $q < 0$ .

Now, from the deep analogy that links the multifractal formalism to thermodynamics (Halsey et al. 1986; Arneodo, Bacry & Muzy 1995), one can define the scaling exponent  $\tau(q)$  from the power-law behavior of the partition function:

$$\mathcal{Z}(q, a) \sim a^{\tau(q)}, \quad a \rightarrow 0^+, \quad (13)$$

where  $q$  and  $\tau(q)$  play respectively the role of the inverse temperature and the free energy. The main result of the wavelet-based multifractal formalism is that in place of the energy and the entropy (i.e. the variables conjugated to  $q$  and  $\tau$ ), one has the Hölder exponent  $h$  (Eq. (9)) and the singularity spectrum  $D(h)$  (Eq. (11)). This means that the  $D(h)$  singularity spectrum of  $f$  can be determined from the Legendre transform of the partition function scaling exponent  $\tau(q)$ :

$$D(h) = \min_q (qh - \tau(q)). \quad (14)$$

From the properties of the Legendre transform, it is easy to convince oneself that monofractal functions that involve singularities of unique Hölder exponent  $h = H$  are characterized by a  $\tau(q)$  spectrum which is a *linear* function of  $q$  of slope  $H$ . On the contrary, a *nonlinear*  $\tau(q)$  curve is the signature of functions that display *multifractal* properties, in the sense that the Hölder exponent  $h (= \partial\tau/\partial q)$  is a quantity that fluctuates depending on the spatial position  $\mathbf{x}$ .

Let us note that the exponents  $\tau(q)$  are much more than simply some intermediate quantities of a rather easy experimental access. For some specific values of  $q$ , they have well known meaning (Muzy, Bacry & Arneodo 1994):

- $q = 0$ : In full analogy with standard box-counting arguments,  $-\tau(0)$  can be identified to the fractal dimension of the set of singularities of  $f$ :

$$-\tau(0) = d_F\{\mathbf{x}, h(\mathbf{x}) < +\infty\}. \quad (15)$$

- $q = 1$ :  $\tau(1)$  is related to the fractal dimension (capacity) of the rough surface  $\mathcal{S}$  defined by the function  $f$ . More precisely:

$$d_F(\mathcal{S}) = \max(2, 1 - \tau(1)). \quad (16)$$

- $q = 2$ :  $\tau(2)$  is intimately related to the scaling exponent  $\beta$  of the spectral density ( $\hat{f}$  is the Fourier transform of  $f$ ):

$$S(k) = \frac{1}{2\pi} \int d\theta |\hat{f}(k, \theta)|^2 \sim k^{-\beta}, \quad (17)$$

where

$$\beta = 4 + \tau(2). \quad (18)$$

In order to avoid numerical drawbacks related to the Legendre transform (Eq. (14)), one can avoid directly performing it by considering the quantities  $h$  and  $D(h)$  as mean quantities

defined in a canonical ensemble (Arneodo, Bacry & Muzy 1995), i.e., with respect to their Boltzmann weights computed from the WTMMM:

$$W_\psi[f](q, \mathcal{L}, a) = \frac{|\sup_{(\mathbf{x}, a') \in \mathcal{L}, a' \leq a} \mathcal{M}_\psi[f](\mathbf{x}, a')|^q}{\mathcal{Z}(q, a)}, \quad (19)$$

where  $\mathcal{Z}(q, a)$  is the partition function defined in equation (12). Then one computes the expectation values (Arneodo, Decoster & Roux 2000):

$$h(q, a) = \sum_{\mathcal{L} \in \mathcal{L}(a)} \ln \left| \sup_{(\mathbf{x}, a') \in \mathcal{L}, a' \leq a} \mathcal{M}_\psi[f](\mathbf{x}, a') \right| W_\psi[f](q, \mathcal{L}, a), \quad (20)$$

and

$$D(q, a) = \sum_{\mathcal{L} \in \mathcal{L}(a)} W_\psi[f](q, \mathcal{L}, a) \ln(W_\psi[f](q, \mathcal{L}, a)), \quad (21)$$

from which one extracts

$$\begin{aligned} h(q) &= \lim_{a \rightarrow 0^+} h(q, a) / \ln a, \\ D(q) &= \lim_{a \rightarrow 0^+} D(q, a) / \ln a, \end{aligned} \quad (22)$$

and therefore the  $D(h)$  singularity spectrum.

Finally, one should note that, a priori, there is no indication for any two realizations of a given stochastic process to have the same  $D(h)$  curve. This has been a topic of discussion in Arneodo, Decoster & Roux (2000) and many of the references therein. That is why any multifractal analysis must be performed on several realizations of the same process with a well-defined averaging protocol. Two averaging methods can be used: quenched and annealed. For the former, the  $\tau(q)$  curve is extracted from averaging  $\langle \ln \mathcal{Z}(q, a) \rangle$  over the number of images,

$$e^{\langle \ln \mathcal{Z}(q, a) \rangle} \sim a^{\tau(q)}, \quad a \rightarrow 0^+, \quad (23)$$

while for the latter,  $\tau(q)$  can be computed after averaging the partition function obtained for each image,

$$\langle \mathcal{Z}(q, a) \rangle \sim a^{\tau(q)}, \quad a \rightarrow 0^+. \quad (24)$$

For example, Arneodo, Decoster & Roux (2000) have empirically demonstrated that in order to have access to a rather large range of  $q$ -values, it was necessary to average the results over 32 images of  $1024 \times 1024$ , where both averaging mechanism gave similar results. The quenched averaging method is used here.

### 3.3.2. Probability Density Functions

From the definition of the partition function in equation (12), one can transform the discrete sum over the WTMMM into a continuous integral over  $\mathcal{M}_\psi[f]$ :

$$\mathcal{Z}(q, a)/\mathcal{Z}(0, a) = \langle \mathcal{M}^q \rangle (a) = \int d\mathcal{M} \mathcal{M}^q P_a(\mathcal{M}), \quad (25)$$

where  $\mathcal{M}$  is a condensed notation for  $\sup_{(\mathbf{x}, a') \in \mathcal{L}, a' \leq a} \mathcal{M}_\psi[f](\mathbf{x}, a')$  and  $P_a(\mathcal{M}) = \int d\mathcal{A} P_a(\mathcal{M}, \mathcal{A})$ , where  $P_a(\mathcal{M}, \mathcal{A})$  is the joint probability density function of the modulus and argument of the WTMMM computed at scale  $a$ . The multifractal description thus consists in characterizing how the moments of the probability density function (pdf)  $P_a(\mathcal{M})$  of  $\mathcal{M}$  behave as a function of the scale parameter  $a$ . The power-law exponents  $\tau(q)$  in equation (13) therefore quantify the evolution of the shape of the  $\mathcal{M}$  pdf across scales. At this point, let us remark that one of the main advantages of using the wavelet transform skeleton is the fact that, by definition,  $\mathcal{M}$  is different from zero and consequently that  $P_a(\mathcal{M})$  generally decreases to zero at zero. This observation is at the heart of the WTMM method since, for this reason, one can not only compute the  $\tau(q)$  spectrum for  $q > 0$  but also for  $q < 0$  (Muzy, Bacry & Arneodo 1991, 1993, 1994). From the Legendre transform of  $\tau(q)$  (Eq. (14)), one is thus able to compute the whole  $D(h)$  singularity spectrum, i.e. its increasing left part ( $q > 0$ ) as well as its decreasing right part ( $q < 0$ ). Furthermore, the well-defined shape of the  $P_a(\mathcal{M})$  plots is a confirmation of a sufficient amount of statistics to allow for a proper convergence in the calculation of the partition functions. Showing the  $P_a(\mathcal{M})$  plots for many scales can tell us whether or not there is a lack of statistics starting from a certain (large) scale. If one is interested in, say, the large scale iso/anisotropic information gathered from the plots of the pdf of the arguments,  $P_a(\mathcal{A}) = \int d\mathcal{M} P_a(\mathcal{M}, \mathcal{A})$ , one should also make sure that the information holds for a sufficient amount of statistics by observing a well-defined shape in the  $P_a(\mathcal{M})$  plot for the corresponding scale. As discussed later in Section 4.1.4 and in Figure 8, the behavior of  $P_a(\mathcal{M})$  at small values of  $\mathcal{M}$  (i.e., how  $P_a(\mathcal{M})$  decreases to 0 at  $\mathcal{M} = 0$ ) characterizes the behavior of the  $\tau(q)$  spectrum (Eq. (13)) for negative  $q$ -values.

## 4. TEST APPLICATIONS OF THE 2D WTMM METHOD

Introduced by Mandelbrot & Van Ness (1968), fractional Brownian motion (fBm) has become a very popular modeling tool used in signal and image (2D and 3D) analysis. It has been used to calibrate the WTMM method in 2D (Arneodo, Decoster & Roux 2000). Construction of fBm models for the ISM were presented in Stutzki et al. (1998). Miville-Deschênes, Levrier & Falgarone (2003) analyzed the effects of the projection of simulated

3D fBm fields in 2D in order to characterize the effects of projection in ISM maps. Non-fBm methods were also used to model the ISM (Hetem & Lépine 1993).

In this section, the analysis of synthetic fBm isotropic monofractal and multifractal 2D surfaces will demonstrate the accuracy and robustness of the 2D WTMM method. Furthermore, we will see how the 2D WTMM method can easily characterize anisotropic structures by analyzing synthetic anisotropic rough surfaces.

#### 4.1. Isotropic Fractional Brownian Surfaces

In this section a review of the definition of 2D fBm is presented. Afterwards, the 2D WTMM methodology described in §3 is tested on several realizations of 2D fBm, for three different Hurst exponent values (Arneodo, Decoster & Roux 2000).

A 2D fBm  $B_H(\mathbf{x})$  indexed by  $H \in ]0, 1[$ , is a process with stationary zero-mean Gaussian increments whose correlation function is given by (Peitgen & Saupe 1988):

$$\langle B_H(\mathbf{x})B_H(\mathbf{y}) \rangle = \frac{\sigma^2}{2} (|\mathbf{x}|^{2H} + |\mathbf{y}|^{2H} - |\mathbf{x} - \mathbf{y}|^{2H}), \quad (26)$$

where  $\langle \dots \rangle$  represents the ensemble mean value and  $\mathbf{x}, \mathbf{y} \in \mathbf{R}^2$ . The variance of such a process is

$$\text{var}(B_H(\mathbf{x})) = \sigma^2 |\mathbf{x}|^{2H} \quad (27)$$

for any  $\mathbf{x} \in \mathbf{R}^2$ . 2D fBm's are self-affine processes that are statistically invariant under isotropic dilations:

$$B_H(\mathbf{x}_0 + \lambda \mathbf{u}) - B_H(\mathbf{x}_0) \simeq \lambda^H [B_H(\mathbf{x}_0 + \mathbf{u}) - B_H(\mathbf{x}_0)], \quad (28)$$

where  $\mathbf{u}$  is a unitary vector and  $\simeq$  stands for the equality in law. The index  $H$  corresponds to the Hurst exponent. But since equation (28) holds for any  $\mathbf{x}_0$  and any direction  $\mathbf{u}$ , this means that almost all realizations of the fBm process are continuous, everywhere non-differentiable, isotropically scale-invariant as characterized by a unique Hölder exponent  $h(\mathbf{x}) = H, \forall \mathbf{x}$ . Thus fBm surfaces are the representation of homogeneous stochastic (mono)fractal functions characterized by a singularity spectrum which reduces to a single point

$$\begin{aligned} D(h) &= 2 && \text{if } h = H, \\ &= -\infty && \text{if } h \neq H. \end{aligned} \quad (29)$$

By Legendre transforming  $D(h)$  according to equation (14), one gets the following expression for the partition function exponent (Eq. (13)):

$$\tau(q) = qH - 2. \quad (30)$$

$\tau(q)$  is a linear function of  $q$ , the signature of monofractal scaling, with a slope given by the index  $H$  of the fBm. The relationship between  $H$  and the power spectral index,  $\beta$  (Eqs. (17) and (18)) is given by

$$\beta = 4 + \tau(2) = 2 + 2H, \quad (31)$$

where  $\beta = \lim_{k \rightarrow \infty} -\frac{\log(S(|\mathbf{k}|))}{\log(|\mathbf{k}|)}$  (in Fourier space) (Eq. (17)).

The 2D WTMM method described in §3 was tested (Arneodo, Decoster & Roux 2000) on isotropic fBm surfaces generated by the so-called Fourier transform filtering method (Ffm) (Peitgen & Saupe 1988). This particular synthesis method is used because of the simplicity of its implementation. Indeed it amounts to a fractional integration of a 2D “white noise” and therefore it is expected to reproduce quite faithfully the isotropic scaling invariance properties. By looking at Figures 3a ( $H = 0.2$ ), 3b ( $H = 0.5$ ) and, 3c ( $H = 0.8$ ), one can see that the fBm surfaces become less and less irregular when increasing the index  $H$ .

#### 4.1.1. Fourier Analysis

The Fourier analysis of 32 ( $1024 \times 1024$ ) images of  $B_{H=0.2}(\mathbf{x})$  is presented in Figure 4. Figure 4a presents some contour plots of the 2D Fourier spectrum that do not display any significant departure from radial symmetry (except along the  $k_x$  and  $k_y$  axes as the consequence of the periodization introduced by the discrete Fast-Fourier Transform). Isotropic scaling is confirmed in Figure 4b where the power spectral density is shown to behave like a power-law as a function of the wavevector modulus  $|\mathbf{k}|$  with an exponent  $\beta = 2.40$ , which is in perfect agreement with equation (31).

#### 4.1.2. Wavelet Analysis

We have wavelet transformed these 32 ( $1024 \times 1024$ ) images of  $B_{H=0.2}(\mathbf{x})$  with a first-order analyzing wavelet (Figs. 2a and 2b). To avoid edge effects, only the  $512 \times 512$  central part of the wavelet transform of each image is kept for analysis. Figure 5 illustrates the computation of the maxima chains and the WTMM for an individual image at three different scales. Figure 5b is the convolution of the original image (Fig. 5a) with the isotropic Gaussian smoothing filter  $\phi_{\text{Gau}}$  (§3.1).

According to the definition of the wavelet transform modulus maxima, the maxima chains correspond to well defined edge curves of the smoothed image (Fig. 5b). The local maxima of  $\mathcal{M}_\psi$  along these curves are located at the points where the sharpest intensity variation is observed. The corresponding arrows clearly indicate that locally, the gradient

vector points in the direction (as given by  $\mathcal{A}_\psi$ ) of maximum change of the intensity surface. When going from large scale (Fig. 5d) to small scale (Fig. 5c), the characteristic average distance between two nearest neighbour WTMMM decreases like  $a$ . This means that the number of WTMMM and in turn, the number of maxima lines, proliferates across scales like  $a^{-2}$ . One thus recovers the theoretical result that the support of the singularities of a 2D fBm (i.e., the set of points where the maxima lines that define the wavelet transform skeleton converge in the limit  $a \rightarrow 0^+$ , ) as a dimension  $d_F = 2$  (Eq. (15)). Note that some maxima chains do not have any WTMMM. The reason is that some chains are monotonic. The only minimum (resp. maximum) that they possess is at an extremity. WTMMM corresponding to these extremities are not kept for analysis.

#### 4.1.3. Numerical Computation of the $\tau(q)$ and $D(h)$ Spectra

The results obtained from the computation of the  $\tau(q)$  and  $D(h)$  spectra using the 2D WTMM method described in §3.3 are presented in Figure 6. In Figure 6a, the partition function  $\mathcal{Z}(q, a)$  (over 32 images of  $B_{H=0.5}(\mathbf{x})$ ) displays a remarkable scaling behavior over more than 3 octaves when plotted versus  $a$  in a logarithmic representation, where  $a$  is expressed in  $\sigma_W$  units. Throughout this paper,  $\sigma_W = 13$  pixels is the width of the analyzing wavelet at the smallest scale where it is still well enough resolved (the highest resolution accessible to our wavelet transform microscope). Moreover, for a wide range of values of  $q \in [-4, 4]$ , the data are in good agreement with the theoretical  $\tau(q)$  spectrum (Eq. (30)). When proceeding to a linear regression fit of the data over the first two octaves as recommended by Audit et al. (2002), one gets the  $\tau(q)$  spectra shown in Figure 6c for three values of the fBm index  $H = 0.2, 0.5, \text{ and } 0.8$ . Whatever  $H$ , the data systematically fall on a straight line, the signature of monofractal scaling properties. However, the slope of this straight line provides a slight underestimate of the corresponding Hurst exponent  $H$ , namely  $H = 0.19, 0.48, \text{ and } 0.77$  respectively. This behavior is also seen in Figures 6a and 6b for the  $\mathcal{Z}(q, a)$  and  $h(q, a)$  functions for individual  $q$  values. Let us point out that a few percent underestimate has also been reported when performing similar analysis of 1D fBm. Theoretical investigation of finite-size effects and statistical convergence has been recently performed to explain this experimental observation (Audit et al. 2002).

#### 4.1.4. Probability Density Functions

In Figure 7 are shown the pdfs  $P_a(\mathcal{M})$  and  $P_a(\mathcal{A})$ , computed at four different values of the scale parameter for  $B_{H=0.2}(\mathbf{x})$ . As seen in Figure 7a,  $P_a(\mathcal{M})$  is not a Gaussian, but

decreases to zero at zero. This explains that when concentrating on the wavelet transform skeleton, the discrete sum in the r.h.s. of equation (12) does not diverge when considering negative  $q$  values. This critical remark is at the heart of the 2D WTMM method: By allowing us to compute the  $\tau(q)$  spectrum for negative as well as positive  $q$  values, the 2D WTMM method is a definite step beyond the 2D structure function method which is simply undefined for negative  $q$  values (the increment pdf being maximum at zero) and is therefore intrinsically restricted to positive  $q$  values, which correspond only to the strongest singularities of the analyzed surfaces.

The corresponding pdfs  $P_a(\mathcal{A})$  are represented in Figure 7b.  $P_a(\mathcal{A})$  clearly does not evolve across scales. Moreover, except for some small amplitude fluctuations observed at the largest scale,  $P_a(\mathcal{A}) = 1/2\pi$  is a flat distribution as expected for statistically isotropic scale-invariant rough surfaces. Moreover, as discussed in §3.3, the well-defined shape of  $P_a(\mathcal{M})$  at the scales shown is a confirmation of the appropriate number of statistics.

Let us now consider the problem of statistical convergence of the  $\tau(q)$  and  $D(h)$  spectra, i.e. the statistical convergence of the partition function  $\mathcal{Z}(q, a)$ . According to equation (25),  $\mathcal{Z}(q, a)$  is the integral of  $\mathcal{M}^q P_a(\mathcal{M})$ . One can show that the monofractal self-similarity relationships yield the following rescaling properties (Arneodo, Decoster & Roux 2000):

$$a^{-qH} \mathcal{M}^q P_a(\mathcal{M}) = \mathcal{F}_q(\mathcal{M}/a^H), \quad (32)$$

where  $\mathcal{F}_q$  are  $q$ -dependent functions that do not depend upon the scale parameter  $a$ . The validity of the above equation has been discussed in detail in Arneodo, Decoster & Roux (2000) and is addressed here in Figure 8 for  $q \in [-3, 4]$ . The data collected at different scales actually collapse on a single distribution whose shape clearly depends upon  $q$ , in good agreement with equation (32). Because of the progressive lack of statistics when one increases  $a$ , the distributions obtained at the largest scales become more and more noisy (especially for large values of  $|q|$ ). This means that the integral of these distributions, i.e.  $\mathcal{Z}(q, a)$ , is less and less accurately estimated at large scales. This explains the requirement of estimating the Hurst exponent of 2D fBm over a rather narrow range of scales at small scales (Audit et al. 2002). To quantitatively and objectively determine the range of acceptable  $q$ -values in the present study, only the  $q$ -values where the difference in area under the curves is  $\leq 10\%$  were kept.

#### 4.1.5. Multifractal Rough Surfaces

At the referee's request, the authors removed the content of this section since multifractality was not found in the H I data. However, tests were performed and the WTMM method

would have detected such quality if it were present. Figures 4b, 6e, and 6f correspond to the analysis of synthetic multifractal surfaces generated with the so-called Fractionally Integrated Singular Cascade (FISC) algorithm presented in Decoster, Roux & Arneodo (2000), where theoretical expressions are given for both the  $\tau(q)$  and  $D(h)$  spectra as well as the relationship the roughness exponents and the power spectral exponent.

## 4.2. Anisotropic Surfaces

Standard 2D fBm models are not always sufficient in fully characterizing real world surfaces (Arneodo, Decoster & Roux 2000). Allowing spatial fluctuations in the local Hölder regularity, i.e., multifractality, gives more flexibility to these models. Another limitation is the isotropy, which is rather idealistic in the case of real textures. In this section we address the issue of anisotropic rough surfaces (Schertzer & Lovejoy 1985, 1987; Peitgen & Saupe 1988; Schmittbuhl, Violette & Roux 1995; Schertzer et al. 1997).

A natural way of introducing some anisotropy in the fast Fourier transform filtering surface synthesis method is to use different fractional integration orders in two orthogonal directions of space. However, although the concept of 2D anisotropic fBm is well-defined mathematically, it has never been validated numerically (to the best of our knowledge). Recent progress has been accomplished in the study of fractional Brownian “sheets” (fBs),  $B_{H_x, H_y}(\mathbf{x})$  where the main difference between the two lies in the homogeneity of the initial conditions of the random process. For a technical description, see Pesquest-Popescu & Lévy Véhel (2002) and Montseny (2004). Let us mention that an alternative method was proposed by Makse et al. (1996) motivated by the generation of long-range correlations in large systems.

We introduce the exponents  $H_x$  and  $H_y$  to describe the global Hurst regularity in the  $x$  and  $y$  directions respectively<sup>4</sup>. An anisotropic surface is thus described as a self-affine two-dimensional function where  $H_x \neq H_y$ .

Two methods are used here to estimate the individual Hurst exponents  $H_x$  and  $H_y$ . The first method consists in a simple 1D Fourier analysis of  $x$ -directional and  $y$ -directional cuts (estimation of the directional power spectral indices<sup>5</sup>,  $\beta_x 2H_x + 1$  and  $\beta_y = 2H_y + 1$ ),

---

<sup>4</sup>Only the horizontal ( $x$ ) and vertical ( $y$ ) directions are considered here to avoid over-crowding this text. More generally, anisotropic structure can be defined in any direction, where the individual Hurst exponents would be defined as  $H_\theta$  and  $H_{\theta+\pi/2}$ .

<sup>5</sup>Note that Eq. (31) can be generally written as  $\beta = 2H + d$ , where  $d$  is the Euclidean dimension.

and the second, explained below in §4.2.4, consists in the analysis of the horizontal and vertical wavelet transform components,  $T_{\psi_1}$  and  $T_{\psi_2}$  (see §3.1). Note that the introduction and characterization of the  $H_x$  and  $H_y$  exponents, where both are in the interval  $[0, 1]$ , is novel.

#### 4.2.1. Fourier Analysis

We have generated 32 ( $1024 \times 1024$ ) images (fBs) of  $B_{H_x=0.10, H_y=0.50}(\mathbf{x})$  where the regularity in the  $x$ -direction,  $H_x = 0.10$ , differs significantly from the regularity in the  $y$ -direction,  $H_y = 0.50$ . The Fourier analysis is presented in Figure 9. Figure 9a presents some contour plots of the 2D Fourier spectrum, where the anisotropic signature is translated as a preference in the  $x$  direction in the  $(k_x, k_y)$  plane. The log-log plot of the 2D power spectrum shown in Figure 9b reveals the relation between the beta index (Eq. (31)) and the minimal Hurst exponent  $H = \min(H_x, H_y) = H_x$ , i.e.  $\beta = 2H_x + 2$ . The actual value of the fitted slope is given by  $\beta = 2.26 \pm 0.06$ , a slight over-estimation<sup>6</sup>. The individual spectral indices calculated from the 1D cuts in Figures 9c and 9d, are  $\beta_x = 1.22 \pm 0.01$  and  $\beta_y = 1.97 \pm 0.01$ . These values are also slightly over (resp. under) estimated, which is expected for such a large difference between the theoretical values  $\beta_x = 2H_x + 1 = 1.20$  and  $\beta_y = 2H_y + 1 = 2.00$  (Montseny 2004).

#### 4.2.2. Wavelet Analysis

We have wavelet transformed these 32 ( $1024 \times 1024$ ) images of  $B_{H_x=0.10, H_y=0.50}(\mathbf{x})$  with a first-order analyzing wavelet (Figs. 2a and 2b). From a visual inspection of Figure 10, one can see that the maxima chains show a vertical tendency, which becomes more and more pronounced when going to small values of  $a$ . In the meantime, the WTMMM proliferate like  $a^{-2}$ , with a characteristic evolution of the corresponding arrows towards a general alignment to the  $x$ -direction ( $\mathcal{A}_\psi$  converges to 0 and  $\pm\pi$ ), i.e., to the direction that corresponds to the most singular behavior as characterized by  $H = \min(H_x, H_y)$ .

---

Therefore, for 1D cuts, one has  $\beta = 2H + 1$ .

<sup>6</sup>The presented uncertainties for  $\beta$ ,  $\beta_x$ , and  $\beta_y$  correspond to the errors from the fitted slopes, over the range  $1 < \log_2(k)$ ,  $\log_2(k^{(x)})$ ,  $\log_2(k^{(y)}) < 8$ .

#### 4.2.3. Numerical Computation of the $\tau(q)$ and $D(h)$ Spectra

In Figure 11 are reported the results of the computation of the  $\tau(q)$  and  $D(h)$  spectra using the 2D WTMM method described in §3. As shown in Figure 11a, the partition function  $\mathcal{Z}(q, a)$  over 32 (1024 x 1024) images, displays a well defined scaling behavior over the range of scales  $1 \leq a \leq 6$  (in  $\sigma_W$  units) when using the first-order wavelet. A linear regression fit of the data for  $-4 \leq q \leq 4$  yields the numerical  $\tau(q)$  spectrum shown in Figure 11c. All the data points fall on a straight line of slope  $H_x = 0.12 \pm 0.01$ , which is in agreement with the estimated  $\beta_x$  just above (§4.2.1). Indeed, the data are well fitted by  $\tau(q) = 0.12 (\pm 0.01) q - 1.96 (\pm 0.04)$ , which confirms that the anisotropic fBs are singular almost everywhere ( $d_F = -\tau(0) \approx 2$ , Eq. (15)). As shown in Figure 11b, one recovers the exponent  $H = \min(H_x, H_y) = H_x$  from the scaling of the expectations values  $h(q, a)$  (Eq. (20)) in the limit  $a \rightarrow 0^+$ . Note that one observes some cross-over at large scales to a scaling behavior with exponent  $H = \max(H_x, H_y) = H_y$  for significantly negative values of  $q$ .

When completing this analysis by computing  $D(q)$  from the scaling behavior of  $D(q, a)$  (Eq. (21)), one gets to the conclusion that the  $D(h)$  singularity spectrum reduces to a single point  $D(h = 0.12 \pm 0.01) = 1.96 \pm 0.04$  ( $D(h) = -\infty$  elsewhere). These results demonstrate that, up to finite-size effects, the 2D WTMM method is powerful enough to account quantitatively for the homogeneous (monofractal) anisotropic scaling properties of rough surfaces, where the minimal directional Hurst exponent corresponding to the most singular direction is detected.

#### 4.2.4. Probability Density Functions

In Figures 7c and 7d are reported the results of the computation of the pdfs  $\mathcal{P}_a(\mathcal{M})$  and  $\mathcal{P}_a(\mathcal{A})$ , from the same set of 32 (1024 x 1024) images of anisotropic rough surfaces ( $B_{H_x=0.10, H_y=0.50}(\mathbf{x})$ ). Both pdfs are shown for four different values of the scale parameter  $a$ . In contrast to what was observed for isotropic monofractal rough surfaces in the previous sections,  $\mathcal{P}_a(\mathcal{A})$  becomes more and more sharply peaked (Fig. 7d) at two values  $\mathcal{A} = 0$  and  $\pm\pi$ , in the limit  $a \rightarrow 0^+$ . These values correspond to the  $x$ -direction associated with the smallest scaling exponent  $H = \min(H_x, H_y) = H_x = 0.10$ . There are also small peaks at  $\pm\pi/2$  which are the signature of the existence of a different scaling exponent  $H_y = 0.50 > H_x$ , but which get smaller and smaller in the limit  $a \rightarrow 0^+$ .

When considering smaller and smaller scales, it turns out that what is happening in the most singular direction, i.e., in the  $x$ -direction of the rough surfaces under study, ultimately governs their scale invariance properties. This explains why both global analysis tools used

just above (the exponents  $\beta$  and  $H$ ), yielded the minimal value of the directional roughness exponents (resp.  $\beta_x$  and  $H_x$ ).

In fact, the two components of the 2D continuous wavelet transform behave as:

$$T_{\psi_1}[f](\mathbf{b}, a) \sim a^{H_x}, \quad (33)$$

and

$$T_{\psi_2}[f](\mathbf{b}, a) \sim a^{H_y}, \quad (34)$$

and this, independently of the specific spatial location  $\mathbf{b}$ . As shown in Figure 12, one recovers this anisotropic scaling behavior on the WTMMM. Indeed, when restricting the computation of the pdfs of  $T_{\psi_1}$  and  $T_{\psi_2}$  to the wavelet transform skeleton, one obtains the following remarkable self-similarity properties:

$$P\left(T_{\psi_1}[f](\mathcal{L}(a))\right) = \mathcal{P}_1\left(T_{\psi_1}[f](\mathcal{L}(a))/a^{H_x}\right), \quad (35)$$

and

$$P\left(T_{\psi_2}[f](\mathcal{L}(a))\right) = \mathcal{P}_2\left(T_{\psi_2}[f](\mathcal{L}(a))/a^{H_y}\right), \quad (36)$$

where  $\mathcal{P}_1$  and  $\mathcal{P}_2$  are two universal functions that do not depend upon the scale parameter  $a$ . When going back to the (modulus, angle) representation, one gets

$$\mathcal{M}_\psi[f](\mathcal{L}(a)) \sim (A_\psi a^{2H_x} + B_\psi a^{2H_y})^{1/2} \sim a^{\min(H_x, H_y)} \sim a^{H_x} \quad (37)$$

where  $A_\psi$  and  $B_\psi$  are wavelet dependent prefactors. In fact, in the limit  $a \rightarrow 0^+$ , one thus finds that the local Hölder regularity is governed by  $H_x = 0.10 = \min(0.10, 0.50) = \min(H_x, H_y)$ . These results corroborate the conclusions derived from the computation of the  $\tau(q)$  and  $D(h)$  spectra in Figure 11. The anisotropic random surface generated in Figure 10a, is a homogeneous (monofractal) rough surface which is invariant with respect to anisotropic dilations. Its local Hölder regularity is the same at each spatial point and is governed by the scaling behavior properties in the direction of minimal regularity. According to equations (33) and (34), one gets

$$\tan \mathcal{A}_\psi[f](\mathcal{L}(a)) = T_{\psi_2}[f](\mathcal{L}(a))/T_{\psi_1}[f](\mathcal{L}(a)) \sim a^{H_y - H_x} \quad (38)$$

which confirms that  $\mathcal{A}_\psi \rightarrow 0$  or  $\pm\pi$  along each maxima line in the limit  $a \rightarrow 0^+$ . This explains the evolution of  $\mathcal{P}_a(\mathcal{A})$  in Figure 7d. To conclude, let us emphasize that, beyond its ability to characterize statistically the Hölder regularity properties, the 2D WTMM method also accounts for possible departure from isotropic scaling. In the case under study in this section, both scaling exponents  $H_x = 0.11 \pm 0.01$  and  $H_y = 0.49 \pm 0.01$  have been numerically estimated with high accuracy (as compared to the results obtained from the Fourier analysis) from the collapse of the  $T_{\psi_1}$  and  $T_{\psi_2}$  pdfs according to equations (35) and (36) in Figures 12c and 12d.

#### 4.2.5. Sensitivity Tests

The sensitivity of our two techniques (directional analyses of the  $x$  and  $y$  components for the Fourier analysis and wavelet transform) must now be tested for smaller values of  $|H_y - H_x|$ . In what follows, a quick overview of a supplemental study will demonstrate more precisely the limitations of both techniques.

Two sets of 32 ( $1024 \times 1024$ ) anisotropic surfaces (fBs) were generated with  $(H_x, H_y) = (0.41, 0.44)$  and  $(H_x, H_y) = (0.45, 0.52)$  respectively. The Fourier analysis of both  $B_{H_x=0.41, H_y=0.44}(\mathbf{x})$  and  $B_{H_x=0.45, H_y=0.52}(\mathbf{x})$  yields the following individual power spectral exponents  $\beta_x = 1.82 \pm 0.01$ ,  $\beta_y = 1.89 \pm 0.01$  and  $\beta_x = 1.90 \pm 0.02$ ,  $\beta_y = 2.01 \pm 0.02$ , while the global (2D) spectral exponents are  $\beta = 2.84 \pm 0.03$  and  $\beta = 2.90 \pm 0.03$  respectively (data not shown).

The computation of the partition functions  $\mathcal{Z}(q, a)$  and expectation values  $h(q, a)$  with the 2D WTMM method yields  $\tau(q)$  and  $D(h)$  spectra which are in good agreement with the theoretical values. From the  $\tau(q)$  spectra, one obtains  $H = 0.40 \pm 0.01$  and  $H = 0.45 \pm 0.01$  respectively, where both values correspond to the minimal Hurst exponent ( $H = \min(H_x, H_y)$ ). The  $D(h)$  singularity spectra reduce to single points:  $D(h = 0.40) = 2.04 \pm 0.04$  and  $D(h = 0.45) = 1.98 \pm 0.04$  (data not shown).

The original and rescaled pdfs of the individual components of the wavelet transform are shown in Figure 13 for  $B_{H_x=0.41, H_y=0.44}(\mathbf{x})$ . The individual Hurst exponents are recovered with very high accuracy. Indeed, one finds  $H_x = 0.41 \pm 0.01$  and  $H_y = 0.44 \pm 0.01$ . Similar accurate estimates,  $H_x = 0.45 \pm 0.01$  and  $H_y = 0.52 \pm 0.01$  are also obtained for  $B_{H_x=0.45, H_y=0.52}(\mathbf{x})$  (data not shown). This quick study shows that our techniques are capable of analyzing anisotropic surfaces with  $|H_y - H_x|$  down to about 0.03. Figure 14, which corresponds to the rescaled pdfs of  $T_{\psi_1}$  by different neighboring values of  $H_x$ , confirms the choice of the uncertainty,  $\sigma = 0.01$ .

## 5. RESULTS

### 5.1. Noise Analysis and Filtering

The 2D WTMM method was used to analyze the five mosaics presented in §2 (see also Figure 1 and Table 1). However, the impact of noise behavior in the CGPS data must be addressed. Originally discussed in Miville-Deschênes et al. (2003), the images obtained from DRAO exhibit a granular structure which is attributed to instrumental noise. A thorough analysis of the noise itself, of its effects on the mosaics, and a filtering method are presented in this section.

### 5.1.1. Noise Analysis from the DRAO Empty Channels

The 2D WTMM analysis presented in this subsection will demonstrate the differences between noise mosaics constructed from some empty channels of the 21-cm data cubes (henceforth called the “DRAO noise”) and synthetic pure white noise (henceforth called “synthetic noise”). For the latter, an isotropic monofractal behavior is expected, with  $D(h = -1) = 2.0$ .

Figure 15 shows a sample of each of the two noise mosaics, with the DRAO noise (Fig. 15a) and the synthetic noise (Fig. 15b). In order to make an adequate comparison, the number of (empty) velocity channels used to construct the DRAO noise mosaics was chosen to be similar to the average number of velocity channels used to construct the five mosaics. A simple visual inspection of Figure 15 clearly shows differences between the DRAO and synthetic noise images. By definition, the synthetic noise is a totally uncorrelated surface, where at the smallest scale, each pixel is randomly different from its neighbor, and at larger scales, no correlated structure exists. However, from the DRAO noise surface, one can clearly see that at the smallest scales, two neighboring pixels are not necessarily uncorrelated. Indeed, the “granularity” seen at the smallest scales of the DRAO noise (black components on a white background) are composed of many pixels. Therefore, any two neighboring pixels on one of these components (or grains) are extremely correlated. At the largest scales, a careful inspection of the DRAO noise surface shows a correlation caused by the so-called “honeycomb structure”, a signature of the effects of the choice of the synthesis telescope pointings (Taylor et al. 2003).

A Fourier analysis similar to what was done in §4 is presented in Figure 16, except that the results presented here correspond to an averaging over the central  $512 \times 512$  parts of 16 (instead of 32)  $1024 \times 1024$  DRAO ( $\diamond$ ) and synthetic ( $\bullet$ ) noise surfaces<sup>7</sup>, where the variance of the synthetic noise was imposed to be equal to the variance of the DRAO noise. The contour plot shown in Figure 16a, corresponding to the synthetic noise, seems perfectly random. Indeed, this is to be expected since all pixels are totally uncorrelated at all scales: no preferred scale exists where more power would be represented. This evenly distributed power translates as a flat 2D power spectrum (Fig. 16b,  $\bullet$ ). The same is true for the analysis of the 1D  $x$  and  $y$ -cuts (Figs. 16c and 16d respectively,  $\bullet$ ). On the other hand, although the power spectra obtained from the 2D surfaces (Fig. 16b) and 1D  $x$  and  $y$  cuts

---

<sup>7</sup>A detailed analysis of the expected level of uncertainty versus the number of images used as well as the size of images is presented in Arneodo, Decoster & Roux (2000), where it is shown that a greater uncertainty is expected for 16 rather than 32 images, but that sub-image numbers in the range 9-18 (which corresponds to the mosaics analyzed here) will yield similar uncertainty levels (see Figure 23 from Arneodo, Decoster & Roux (2000).)

(Figs. 16c and 16d respectively) from the DRAO noise ( $\diamond$ ) show a relatively flat slope for the intermediate scales, one can clearly see a tangible steepening of the slope at large scales (low values of the wave vector  $k$ ) and a steepening of the slope at small scales (large  $k$ ). This is in agreement with the above discussion, i.e., the large scale honeycomb structure, and the extremely correlated small scale granularity. Finally, note that there is no indication of a directional preference (anisotropy) from the power spectral analysis of the 1D cuts.

The computation of the  $\tau(q)$  and  $D(h)$  spectra for both the DRAO ( $\diamond$ ) and synthetic ( $\bullet$ ) noise surfaces are shown in Figure 17. Figure 17 yields the estimation of the Hurst exponents for the synthetic noise surfaces ( $\bullet$ ), i.e.,  $D(h = -1.00) = 2.01 \pm 0.02$ , as well as the DRAO noise surfaces ( $\diamond$ ), i.e.,  $D(h = -1.06) = 2.02 \pm 0.04$ . The behavior of the expectation values for the DRAO noise surfaces ( $\diamond$ ) shown in Figure 17b is in agreement with the above discussion, namely that the surfaces tend to be more correlated respectively at small and large scales, which translates as a higher value for the Hurst exponent,  $H$ , and thus a more positive (or rather, less negative) slope for  $h(q, a)$ .

The probability density functions  $P_a(\mathcal{M})$  and  $P_a(\mathcal{A})$  for the DRAO noise are shown in Figure 18. Unlike the modulus pdfs analyzed in §4, the  $P_a(\mathcal{M})$  pdfs shown in Figure 18a, where a first-order analyzing wavelet was used, show a widening of the curves with decreasing scale. This is caused by a negative ( $H = -1$ ) Hurst exponent.

In Figure 18b, there are small oscillations in the pdfs of the arguments,  $P_a(\mathcal{A})$ , of comparable size to what was observed for isotropic fBm surfaces (§4.1) for the smallest scales (full line and  $\diamond$ ). However, for the largest scales ( $\triangle$  and  $\square$ ), there are two clear peaks at 0 and  $\pm\pi$ . The peaks are caused by the large scale correlations discussed above: the honeycomb effect. Since these DRAO noise surfaces were cut-up in a systematic and similar way for all 16 analyzed surfaces, the position of the honeycomb lattice is similar, and in fact, accentuated when averaging over the 16 surfaces. One way to get rid of the anisotropic signature would be to construct a large DRAO noise mosaic similar to the spiral and inter-arm mosaics presented in Figure 1. Instead, one can use the third-order analyzing wavelet, which is blind to linear and quadratic behaviors<sup>8</sup>. The third-order analyzing wavelet was thus used in Figure 18d, where one can clearly see the dampening of the large scale peaks from Figure 18b. This is a spectacular demonstration of the strength of the 2D WTMM method. Indeed, the large scale anisotropy is easily dealt with and one can be certain that the honeycomb structure will not affect the results presented in this paper.

As will be shown in what follows, another, perhaps equally important topic that should

---

<sup>8</sup>In fact, an  $n$ -order analyzing wavelet is blind to polynomial behaviors of degree  $n - 1$  (Arneodo, Decoster & Roux 2000).

be emphasized, is that the values of the modulus of the wavelet transform (range of  $x$  values in Figures 18a and 18c) is quite small compared to the values of the modulus of the five analyzed mosaics. This means that even if there were an anisotropic structure in the DRAO noise surfaces, corresponding to an artificial (instrumental) anisotropic signature, its contribution to the mosaics would be so small as to have absolutely no effect on the results.

### 5.1.2. Filtering

In order to deal as best as possible with the granularity of the DRAO data, the filtering method presented in Miville-Deschênes et al. (2003), based on the wavelet-based “à trous” algorithm, was used here to filter the five mosaics. The method consists in the decomposition of the images on a wavelet basis. In order to improve the signal to noise ratio, only the wavelet coefficients satisfying a threshold condition relative to the amplitude of the noise are kept in the reconstruction algorithm. The effects of the filtering on the Local arm mosaic are shown in Figure 19 for the 2D (Fig. 19b) and 1D (Figs. 19c and 19d) Fourier analysis. With the unfiltered data, the wavelet analysis reaches areas of only  $\sim 2^{1.4}\sigma_W \approx 34$  pixels in diameter. Filtering improves the scale span down to areas of  $\sim 2^{0.9}\sigma_W \approx 24$  pixels in diameter only ( $\approx 7$  arc minutes). In the upcoming sections, we limited the analysis of the data to a scale just preceding the slope change seen in Fig. 19b. This value changes somewhat for the different mosaics. The position of the slope change has been calculated for each mosaic. These positions are respectively  $2^{1.1}$ ,  $2^{1.0}$ , and,  $2^{0.9}$ , for the Local, Perseus, and Outer arms and  $2^{1.0}$  and  $2^{1.0}$  for the Inter I and Inter II mosaics (in  $\sigma_W$  units, where  $\sigma_W = 13$  pixels).

## 5.2. The Three Spiral Arms

### 5.2.1. Fourier Analysis

The Fourier analysis of the subregions outlined in white in Figures 1a, 1c, and 1e are presented in Figure 19.

Figure 19a presents a contour plot of the 2D Fourier spectrum of the Local arm subregions, where a circle was added to help the reader see the slight ellipticity of the contours, which is also present in the 2D Fourier spectra of the Perseus and Outer arm subregions (data not shown). As was done for the synthetic surfaces (§4.1 and 4.2), where the analysis was performed by averaging over the 32 central  $512 \times 512$  parts of the original  $1024 \times 1024$  images, all results presented here correspond to an averaging over all white subregions presented in Figure 1. From the log-log plot of the 2D power spectrum shown in Figure 19b, the

beta index was estimated to be  $\beta = 2.95 \pm 0.05$ ,  $2.97 \pm 0.04$ , and  $2.94 \pm 0.05$  for the Local, Perseus, and Outer arms respectively<sup>9</sup>. The range of the fits correspond to the length of the straight lines located above the log-log plots. A further Fourier analysis was performed by calculating the power spectrum on the  $x$  and  $y$  one-dimensional cuts of each mosaic. The fact that the values obtained for the exponent  $\beta_x = 1.82 \pm 0.04$ ,  $1.91 \pm 0.05$ , and  $1.76 \pm 0.06$  are strictly less than those extracted for  $\beta_y = 1.97 \pm 0.10$ ,  $2.03 \pm 0.05$ , and  $1.94 \pm 0.05$  is in agreement with the slightly elliptical shape of the contours found in Figure 19a. This could be interpreted as a first indication that an anisotropic structure is present in these three mosaics. However, one cannot solidly quantify this affirmation with the Fourier analysis alone.

### 5.2.2. Wavelet Analysis

We have wavelet transformed the subregions of the Local, Perseus, and Outer arms with a first-order analyzing wavelet (Figures 2a and 2b). Again, to avoid edge effects, only the central parts of the wavelet transform of each  $1024 \times 1024$  image, which are represented by the white subregions in Figures 1a, 1c, and 1e, are kept for analysis. All of these subregions are  $\leq 512 \times 512$ . Figure 20 illustrates the computation of the maxima chains and the WTMMM for an individual image of the Local arm at three different scales. Figure 20b shows the convolution of the original image (Fig. 20a) with the isotropic Gaussian smoothing filter  $\phi_{\text{Gau}}$  (Eq. (1)).

As seen for the study of synthetic surfaces in §4.1 and 4.2, the maxima chains correspond to well defined edge curves of the smoothed image. The local maxima of  $\mathcal{M}_\psi$  along these curves are located at the points where the sharpest intensity variation is observed. The corresponding arrows clearly indicate that locally, the gradient vector points in the direction (as given by  $\mathcal{A}_\psi$ ) of maximum change of the intensity surface. Going from large scale (Fig. 20d) to small scale (Fig. 20c), the characteristic average distance between two nearest neighbour WTMMM decreases like  $a$ . This means that the number of WTMMM and in turn, the number of maxima lines, proliferates across scales like  $a^{-2}$ , like isotropic fBm and anisotropic fBs monofractal surfaces. This is an indication that the Local arm mosaic is a rough surface which is likely to be singular almost everywhere ( $-\tau(0) = d_F = 2$ ). For the sake of concision the corresponding results for the Perseus and Outer arms are not shown as they are qualitatively similar to those obtained in Figure 20 for the Local arm.

---

<sup>9</sup>The presented uncertainties for  $\beta$ ,  $\beta_x$ , and  $\beta_y$  correspond to the errors from the fitted slopes.

### 5.2.3. Numerical Computation of the $\tau(q)$ and $D(h)$ Spectra

The results obtained from the computation of the  $\tau(q)$  and  $D(h)$  spectra using the 2D WTMM method described in §3.3 are presented in Figure 21. In Figures 21a and 21b the partition functions  $\mathcal{Z}(q, a)$  and the expectation values  $h(q, a)$  for the Local ( $\diamond$ ), Perseus ( $\square$ ), and Outer ( $\circ$ ) arms display excellent scaling behavior over the range  $a \in [2^{0.9}\sigma_W, 2^{3.0}\sigma_W]$  when plotted versus  $a$ , for the range of values of  $q \in [-1, 3]$ . Although the mosaics were filtered to minimize the noise, the wavelet analysis is restricted to the scales larger than  $a = 2^{0.9}\sigma_W = 24$  pixels ( $\sigma_W = 13$  pixels).

When proceeding to a linear regression fit of the data over the ranges  $a \in [2^{1.1}, 2^{2.6}]$ ,  $a \in [2^{1.0}, 2^{2.6}]$ , and  $a \in [2^{0.9}, 2^{2.6}]$  respectively (in  $\sigma_W$  units) for each spiral arm, one gets the  $\tau(q)$  spectra shown in Figures 21c, 21d, and 21e. The data fall on straight lines, reflecting the signature of monofractal scaling properties. The slopes of these straight lines correspond to the Hurst exponents  $H = 0.52 \pm 0.03$ ,  $H = 0.53 \pm 0.03$ , and  $H = 0.51 \pm 0.03$  respectively for the Local, Perseus, and Outer arms, when averaged over all subregions. Accordingly, the  $D(h)$  singularity spectra shown in Figures 21f, 21g, and 21h collapse to single points  $D(h = 0.52) = 2.02 \pm 0.03$ ,  $D(h = 0.53) = 2.01 \pm 0.03$ , and  $D(h = 0.51) = 2.03 \pm 0.03$ , a remarkably precise result considering the relatively small amount of available data. This is a quantitative confirmation that the Local, Perseus, and Outer mosaics are “almost everywhere” singular.

### 5.2.4. Probability Density Functions

In Figure 22 are shown the pdfs  $P_a(\mathcal{M})$  and  $P_a(\mathcal{A})$  for the Local arm, computed for four different values of the scale parameters  $a = 2^{1.0}$ ,  $2^{1.5}$ ,  $2^{2.0}$ , and  $2^{2.5}$  (in  $\sigma_W$  units, where  $\sigma_W = 13$  pixels). As seen in Figure 22a, where a first-order wavelet was used,  $P_a(\mathcal{M})$  is not a Gaussian, but decreases to zero at zero, an expected property which was discussed in §4.1. The corresponding pdfs  $P_a(\mathcal{A})$  are represented in Figure 22b.  $P_a(\mathcal{A})$  is clearly peaked at  $\pm\pi/2$  and the observed maxima seem to slightly depend on the scale parameter  $a$ . This is a solid confirmation that the mosaics exhibit an anisotropic signature. In Figures 22c and 22d are shown the pdfs  $P_a(\mathcal{M})$  and  $P_a(\mathcal{A})$  using a third-order wavelet. A zoom-in on the left peak of  $P_a(\mathcal{A})$  is included in Figure 22d, showing the scale dependence. For the smallest and largest scales shown in the zoom-in window, average values are clearly different even within uncertainty:  $0.206 \pm 0.005$  for the smallest scale and  $0.247 \pm 0.015$  for the largest.

The fact that the peaks in  $P_a(\mathcal{A})$  do not fade when going from the first-order to the third-order wavelet is a confirmation that the anisotropy is not caused by a large-scale structure in the mosaic (Roux, Arneodo & Decoster 2000). The anisotropic signature detected in

the mosaics is not caused by the large-scale shape of the galactic disk and the anisotropy is therefore inherent to the analyzed H I structure. As seen in §4.2 with the synthetic anisotropic surfaces, having many more WTMMM pointing towards  $\pm\pi/2$  tells us that the direction of greatest intensity variation is vertical. This should be interpreted as a situation where the fluctuations in the vertical direction have a greater variability than the fluctuations in the horizontal direction, as characterized by Hurst exponent values  $H_x > H_y$ . However, this is surprisingly and interestingly not the case here. An explanation is given in the next paragraphs.

The corresponding pdfs for the Perseus and Outer arms are shown in Figure 23 (only the ones computed with the third-order analyzing wavelet are illustrated). They display qualitatively the same characteristics as those previously observed for the Local arm except that fact that the  $P_a(\mathcal{M})$  curves are wider for the Perseus mosaics (Fig. 23a) than for the two other spiral arms (Figs. 22c and 23c). This is simply the signature of the intensity levels being much more variable in the Perseus mosaic than in the two others (see Figure caption 1). Again, a zoom-in on the left peak of  $P_a(\mathcal{A})$  is included in Figure 23d, showing the scale dependence. Here again, average values are also different even within uncertainty:  $0.199 \pm 0.005$  for the smallest scale and  $0.224 \pm 0.013$  for the largest.

In Figures 24a and 24b are shown the pdfs of the  $x$  and  $y$  components of the wavelet transform of the Local arm in logarithmic form:  $\ln(P_a(T_{\psi_1}))$  vs  $T_{\psi_1}$  and  $\ln(P_a(T_{\psi_2}))$  vs  $T_{\psi_2}$ . Unlike the results obtained from Figures 12 and 13, for the synthetic anisotropic surfaces (§4.2), the  $T_{\psi_2}$  curves in Figure 24b are wider than those in Figure 24a, even though we expect to have  $H_x > H_y$ . Indeed, when calculating the individual Hurst exponents by rescaling these curves by  $a^{H_x}$  and  $a^{H_y}$  in Figures 24c and 24d, we find  $H_x = 0.42 \pm 0.03$  and  $H_y = 0.52 \pm 0.03$  respectively. Therefore, the global Hurst exponent found in §5.2.3, namely  $H = 0.52$  is not equal to  $\min(H_x, H_y)$  but is rather equal to  $\max(H_x, H_y)$ . The analysis of the rescaled pdfs using the third-order wavelet in Figures 24e and 24f confirms these results:  $H_x = 0.41 \pm 0.03$  and  $H_y = 0.52 \pm 0.03$ . The uncertainty ( $\sigma = 0.03$ ) on the values of  $H_x$  and  $H_y$  was determined as in §4.2.5 (Fig. 14). As mentioned above, the uncertainty level is inversely proportional to the number of images over which the results were obtained, but is considered to be similar from one mosaic to another (Arneodo, Decoster & Roux 2000).

Quite similar estimates of  $H_x$  and  $H_y$  were obtained with the first-order analyzing wavelet for the Perseus arm ( $H_x = 0.42 \pm 0.03$ ,  $H_y = 0.52 \pm 0.03$ ) and the Outer arm ( $H_x = 0.43 \pm 0.03$ ,  $H_y = 0.52 \pm 0.03$ ) (data not shown). The use of the third-order analyzing wavelet confirms the robustness of these estimates for the Perseus arm ( $H_x = 0.40 \pm 0.03$ ,  $H_y = 0.50 \pm 0.03$ ) as well as for the Outer arm ( $H_x = 0.41 \pm 0.03$ ,  $H_y = 0.48 \pm 0.03$ ). The results are summarized in Table 2.

The difference between the width of the curves of  $\ln(P_a(T_{\psi_2}))$  vs  $T_{\psi_2}$  and  $\ln(P_a(T_{\psi_1}))$  vs  $T_{\psi_1}$  is significant. The behavior of the wavelet transform is much more variable in  $T_{\psi_2}$  than in  $T_{\psi_1}$ , explaining the larger width of the former compared to the latter. This phenomenon affects the estimate of the Hurst exponent when calculated with the 2D WTMM methodology (§3.3). In effect, since the global  $H$  is obtained from the scaling behavior of  $\mathcal{M} = (T_{\psi_1}^2 + T_{\psi_2}^2)^{1/2} \sim a^H$  (Eq. (37)), the contribution to  $\mathcal{M}$  from  $T_{\psi_2}$  is so strong that it dominates the scaling law behavior over the accessible range of scales. Since  $T_{\psi_2} \sim a^{H_y}$  (Eq. (34)), the estimate of the global Hurst exponent on this range of scales is thus governed by the  $y$  component of the wavelet transform, i.e.,  $H = H_y = \max(H_x, H_y) = 0.52 \pm 0.03$ . Furthermore, since the noise restrains us from having access to the smallest scales, where the notions of Hölder and Hurst exponents are valid (i.e., when  $a \rightarrow 0^+$ , see §3.1), it is not unequivocal that the measured global Hurst exponent should be the minimal value of  $H_x$  and  $H_y$ . If one could have access to the smallest range of scales ( $a \rightarrow 0^+$ ), the global Hurst exponent would be equal to the minimum of the  $x$  and  $y$  components, i.e.,  $H = \min(H_x, H_y) = H_x = 0.42 \pm 0.03$ , as seen for the synthetic anisotropic surfaces in §4.2.

Note that any other fractal or multifractal analysis tool would have misleadingly detected  $\max(H_x, H_y)$  as the global Hurst exponent of these mosaics, a clear evidence demonstrating how the wavelet transform is the perfect analysis tool for anisotropic fractal analyses.

Now, physical and/or instrumental processes must exist to explain these two phenomena (the mere presence of an anisotropic signature and the fact that  $\mathcal{M}$  scales with  $\sim a^{\max(H_x, H_y)}$  instead of  $\sim a^{\min(H_x, H_y)}$  on the range of scales available to the analysis). Such a discussion is postponed to §6.2.

This section concludes with the analysis of the statistical convergence of the partition functions for the mosaics, where, as in §4.1.4, the criteria follow those previously validated in Arneodo, Decoster & Roux (2000). As an example, Figure 25, corresponding to the Local arm, validates the choice for the range of acceptable values for  $q \in [-1, 3]$  for all mosaics. The data collected at different scales collapse on a single distribution whose shape depends on  $q$ . This is a confirmation that the WTMM analysis is affected by the fact that the number of sub-regions in the mosaics does not total  $32\,1024 \times 1024$  images and, perhaps more importantly, the fact that the smallest scales (where the WTMM are found in greatest numbers:  $N_{\text{WTMM}} \sim a^{-2}$ ) are unavailable due to the noise.

### 5.3. The Two Inter-Arms

#### 5.3.1. Fourier Analysis

The Fourier analysis of the subregions outlined in white in Figures 1b and 1d for the two inter-arms are presented in Figure 26. The  $\beta$  exponents obtained from the log-log plots of the corresponding 2D power spectra shown in Figure 26b are  $\beta^{\text{I}} = 2.93 \pm 0.05$  and  $\beta^{\text{II}} = 2.94 \pm 0.05$  for the Inter I and Inter II mosaics respectively. The individual beta indices are  $\beta_x^{\text{I}} = 1.90 \pm 0.04$ ,  $\beta_x^{\text{II}} = 1.85 \pm 0.06$  and  $\beta_y^{\text{I}} = 1.89 \pm 0.03$ ,  $\beta_y^{\text{II}} = 1.89 \pm 0.04$ . The differences between  $\beta_x$  and  $\beta_y$  for the inter-arms are not as significant as for the spiral arms (§5.2.1). Anisotropy may be present but the calculated uncertainties prevent any firm statement. Therefore, from the Fourier analysis alone, one cannot compare the roughness nor the strength of this anisotropic signature with those of the three spiral arms.

#### 5.3.2. Wavelet Analysis

The wavelet analysis for the subregions of the Inter I and Inter II mosaics with a first-order analyzing wavelet gives qualitatively similar results to those illustrated in Figure 20 for the Local arm subregions. As already seen for the study of synthetic surfaces in §4.1 and 4.2, as well as the study of the three spiral arms in §5.2, the maxima chains correspond to well defined edge curves of the smoothed image. The number of WTMMM and in turn, the number of maxima lines that define the wavelet transform skeleton, proliferates across scales like  $a^{-2}$ , a behavior that indicates that the inter-arm mosaics are rough surfaces that are likely to be everywhere singular ( $-\tau(0) = d_F \approx 2$ , Eq. (15)).

#### 5.3.3. Numerical Computation of the $\tau(q)$ and $D(h)$ Spectra

The results obtained from the computation of the  $\tau(q)$  and  $D(h)$  spectra for the Inter I and Inter II mosaics are presented in Figure 27. In Figures 27a and 27b, the partition functions  $\mathcal{Z}(q, a)$  and the expectation values  $h(q, a)$  display excellent scaling behaviors over the range  $a \in [2^{0.9}\sigma_W, 2^{3.0}\sigma_W]$  when plotted versus  $a$ , where the range of values of  $q$  is  $q \in [-1, 3]$ .

When proceeding to a linear regression fit of the data over the ranges  $a \in [2^{1.0}, 2^{2.5}]$  and  $a \in [2^{1.0}, 2^{3.0}]$  for the Inter I and Inter II mosaics respectively (in  $\sigma_W = 13$  units), one gets the  $\tau(q)$  spectra shown in Figures 27c and 27d. The first difference between the spiral arms and the inter-arm mosaics is that the data for the latter do not fall exactly on straight lines.

However, the departure from linearity is very slight. Many more data, and less noisy mosaics would be needed to have access to values of  $q$  outside of the range  $[-1, 3]$  that would allow us to diagnose some departure from monofractal scaling (see Fig. 6e). Therefore, one can only say that there is a slight possibility that the two inter-arm mosaics display multifractal scaling, and they will thus be considered as monofractal.

The slopes of the  $\tau(q)$  spectra in Figures 27c and 27d correspond to the following Hurst exponent values  $H = 0.44 \pm 0.03$  and  $H = 0.45 \pm 0.03$  respectively for the Inter I and Inter II mosaics. Accordingly, the  $D(h)$  singularity spectra shown in Figures 27e and 27f reduce to a single point  $D(h = 0.44) = 2.00 \pm 0.03$  and  $D(h = 0.45) = 2.03 \pm 0.03$  respectively (note that one can notice some evidence of a parabolic behavior as a possible signature of multifractal scaling, see Fig. 6f). The inter-arm mosaics are thus everywhere singular.

#### 5.3.4. Probability Density Functions

In Figures 28a and 28b are shown the pdfs  $P_a(\mathcal{M})$  and  $P_a(\mathcal{A})$  of the Inter I subregions, computed with the first-order analyzing wavelet (Figs. 2a and 2b) for four different values of the scale parameters  $a = 2^{1.0}$ ,  $2^{1.5}$ ,  $2^{2.0}$ , and  $2^{2.5}$  (in  $\sigma_W = 13$  units). Again,  $P_a(\mathcal{A})$  is clearly peaked at  $\pm\pi/2$ , a behavior very similar to what was observed in Figures 22 and 23 for the three spiral arms. This is a solid confirmation that, even though the study of the individual beta indices ( $\beta_x$  and  $\beta_y$ ) did not exhibit clear anisotropic information, the mosaics do have an anisotropic structure. In Figures 28c and 28d are shown the pdfs  $P_a(\mathcal{M})$  and  $P_a(\mathcal{A})$  using a third-order analyzing wavelet. The fact that the peaks in  $P_a(\mathcal{A})$  do not fade when going from the first-order to the third-order wavelet is a confirmation that the anisotropy is not caused by a large-scale structure in the mosaic, a confirmation that the anisotropic signature, like the one found in the spiral arms, is inherent to the analyzed H I structure. However, there is a major difference from the argument pdfs obtained for the spiral arms. As seen in Figure 28d, the zoomed-in section shows that average results now overlap within uncertainty:  $0.215 \pm 0.010$  for the smallest scale and  $0.231 \pm 0.015$  for the largest.  $P_a(\mathcal{A})$  for the Inter I subregions does not display any significant scale dependence which strongly suggests that as previously guessed from the Fourier analysis, the two scaling (Hurst) exponents  $H_x \approx H_y$ . Similar scale independent pdfs are observed for the Inter II subregions (data not shown).

A analysis of the behavior of the pdfs of the  $x$  and  $y$  components of the wavelet transform of the Inter I subregions in logarithmic form:  $\ln(P_a(T_{\psi_1}))$  vs  $T_{\psi_1}$  and  $\ln(P_a(T_{\psi_2}))$  vs  $T_{\psi_2}$  was performed. Like the pdfs of the  $x$  and  $y$  components for the spiral arms (Fig. 24), the  $T_{\psi_2}$  curves for the inter-arms are wider than the  $T_{\psi_1}$  curves (data not shown). When calculating

the individual Hurst exponents by rescaling these curves by  $a^{H_x}$  and  $a^{H_y}$  respectively, we find  $(H_x, H_y) = (0.45, 0.44)$  and  $(H_x, H_y) = (0.42, 0.45)$  ( $\pm\sigma = 0.03$ ) respectively for the Inter I and Inter II mosaics (data not shown). The analysis of the rescaled pdfs using the third-order analyzing wavelet yields  $(H_x, H_y) = (0.41, 0.43)$  and  $(H_x, H_y) = (0.42, 0.45)$  ( $\pm\sigma = 0.03$ ) respectively for the Inter I and Inter II mosaics (data not shown). Therefore from the first and third-order wavelet analysis of the rescaled pdfs, one cannot determine whether  $H_x < H_y$  or  $H_x > H_y$  (within  $1\sigma$ ). This confirms that for both inter-arm regions, the global Hurst exponent found from the Fourier is the same as the directional Hurst exponents, i.e.,  $H \sim H_x \sim H_y \sim 0.43 \pm 0.03$ .

However, the inter-arm mosaics do display some scale independent anisotropy since the pdfs of the arguments ( $P_a(\mathcal{A})$ ) are not flat like the ones for the isotropic monofractal fBm surfaces (Fig. 7b). Indeed, there is no doubt that the  $P_a(\mathcal{A})$  curves for the inter-arm mosaics are peaked at  $\pm\pi/2$  (Figs. 28b and 28d). How then, can one have  $H_x = H_y$ ? The answer comes from the very important fact that the  $T_{\psi_2}$  curves are wider than the  $T_{\psi_1}$  curves. The strong contribution from  $T_{\psi_2}$  to  $\mathcal{M} = (T_{\psi_1}^2 + T_{\psi_2}^2)^{1/2}$  causes the presence of these peaks. This means that the strength of the preferred direction of the WTMMM (along the  $y$ -axis), i.e.  $\pm\pi/2$ , does not change with scale.

Therefore, there are two types of anisotropy. First, there is a scale independent anisotropic signature (inter-arms) caused only by the greater variability of the  $y$  component of the wavelet transform ( $T_{\psi_2}$ ). The second is a scale dependent anisotropic signature (spiral arms) caused by different directional scaling exponents, i.e.,  $H_x \neq H_y$  (smaller the scale, stronger the anisotropy). In other words, the ratio of the number of horizontal versus vertical arrows does not change with scale for the inter-arms mosaics, while this ratio does change with scale for the spiral arms (Fig. 20).

## 6. ANALYSIS AND DISCUSSION

A summary of the results obtained from the 2D WTMM analysis is presented in Table 2. Before starting the analysis, the reader must be reminded that the regions examined here were chosen very carefully. It has been known for some time (see Burton (1976)) that the calculation of the column density is affected by regions where the opacity is  $\geq 1$ . Therefore, areas with strong absorption features were avoided. Since the galactic plane is sampled, optical thinness is not claimed for every pixel! However, the sampled area ( $101^\circ \leq l \leq 145^\circ, |b| \lesssim 2^\circ$ ) is especially simple and favorable. The spiral arms are arranged in such a way that lines of constant spiral phase are approximatively lines of constant radial velocity as well. Hence the column density maps combine both velocity field fluctuations

and density fluctuations as sources of  $T_B$  variations (Rohlfs 1974).

Albeit these attenuating circumstances, one cannot rule out that our results are affected by the presence of some degree of optical thickness in any given pixel. Lazarian & Pogosyan (2004) have argued that measuring a power law slope of  $-\beta = -3$ , as found here, could be the indication that absorption is affecting power spectrum calculations. The best way to test if the results presented here are affected would be to calculate the power spectra on an increasing sum of velocity channels starting with one, then the sum of two, etc. for each subregion. Such calculations were done in Stanimirovic & Lazarian (2001) where the power law slope was shown to change as the velocity slice thickness increased. However, given that the DRAO observations have a noise level three times higher than the Stanimirovic & Lazarian (2001) data, the statistical analysis of small portions of the mosaics may not enable the detection of significant changes in  $\beta$  and  $H$  as a function of velocity thickness. Green (1993) calculated the slopes of the power spectra of galactic plane data obtained with the DRAO telescope. He studied the variation of the slopes for adjacent sums of three velocity channels (the minimum number of channels to render noise manageable). Green indeed found differing slopes for the power spectra but most were identical within the, sometimes large, uncertainties. Green’s work is indicative that our current data may not provide conclusive evidence on the effect of absorption. Nevertheless, Green’s results and the referee’s prodding encouraged us to make the calculations. The results are shown in Tables 3 and 4 where  $\beta$  was calculated for an ever increasing number of channels (1 to 26, 0.82 to 21.4 km s<sup>-1</sup>) for 11 portions of the Local spiral arm (i.e., the subregions outlined in Figure 1). The power law slopes were calculated for the same scale range of 2.8 to 22.3 parsecs (i.e.  $1 \lesssim \log_2(k) \lesssim 4$ ) for proper comparison. The smaller scales were strongly affected by the noise for small sums of channels. Table 3 contains the slopes calculated from the mean power law of the 11 regions of the Local arm mosaic and the mean slope from the 11 individual power laws with the accompanying standard deviation. The results for every region are not shown since the variation of  $\beta$  from region to region remains within the uncertainties. Figure 29 illustrates the slopes behavior with increasing number of channels. The power law slope remains constant within the uncertainties, contrary to what was found by Stanimirovic & Lazarian (2001) where the slope increased with velocity slice thickness. One must be aware that the latter observations dealt with the Small Magellanic Cloud and a scale range of 30 to 4000 parsecs.

To better test the predictions of Lazarian & Pogosyan (2004), trends were looked for to smaller scales (1.4 pc, i.e.  $1 \lesssim \log_2(k) \lesssim 5$ ) using only sums of 11 channels or more, where the noise level was low enough. Again the slopes remain constant within the uncertainties as shown in the upper part ( $\triangle$ ) of Figure 29 (see also Table 4). These results are at odds with similar calculations done from observations of the SMC (Stanimirovic & Lazarian 2001), LMC (Elmegreen, Kim & Stavely-Smith 2001) and M81 (Elmegreen, Elmegreen & Leitner

2003). The difference may come from the domination of the power measured at very large scales (hundreds of parsecs). Elmegreen, Kim & Stavely-Smith (2001) even suggested that such behavior was related to the finite thickness of a galaxy’s disk. However, Dickey et al. (2001) used data from the Southern Galactic Plane Survey to calculate the power spectra for two regions of the fourth galactic quadrant very similar in extent and scales to each of our 11 regions ( $\approx 1.4^\circ$ ). Their region 2 is on the galactic plane and shows a power spectra slope behavior with velocity thickness almost identical to our 11 regions. This similarity is very interesting considering that the velocity gradient along the line of sight caused by the differential Galactic rotation is different. One may therefore be limited in the ability to identify varying physical conditions in the Galactic plane using only power spectra slopes. Either the predictions of Lazarian & Pogosyan (2004) cannot be confirmed with the data presented in this paper or HI self-absorption dominates at so many scales that the search for velocity-density correlations in the framework of turbulence study cannot be done in the Galactic plane.

The following general analysis is presented in two parts. A recap of the results presented in §5 together with the differences and similarities between the results obtained from the spiral and inter-arm mosaics are presented in §6.1, and the astrophysical discussion is presented in §6.2.

### 6.1. Spiral vs Inter Arms

The global Hurst exponents found from the slope of the linear  $\tau(q)$  spectra computed with the 2D WTMM method for the inter-arm mosaics ( $H = 0.44 \pm 0.03$  and  $H = 0.45 \pm 0.03$ ) are strictly less (within uncertainty) than those of the Local, Perseus, and Outer spiral arms ( $H = 0.52 \pm 0.03$ ,  $H = 0.53 \pm 0.03$ , and  $H = 0.51 \pm 0.03$ ) for the physical scales shown in Table 2. Therefore, the H I from the spiral arms looks smoother than the H I from the inter-arm regions. Note that the Fourier analysis alone cannot give such precise quantitative information. Indeed, the power spectra analysis gives essentially the same slope whether considering the arms (§5.2.1) or inter-arms (§5.3.1), i.e.  $-\beta \sim -3.0$  (corresponding to  $H \sim 0.5$ ). However, within each arm or inter-arm, the slopes vary significantly from one region to the next (Table 5). The standard deviations of the mean slopes for all regions are larger than the uncertainties. Again, the Perseus arm has the larger variations. No trends were found between individual slopes and longitude. The overall slope of  $-\beta \sim -3.0$  confirms the results of Crovisier & Dickey (1983) and Dickey et al. (2001) but for a much larger section of the Milky Way. These authors observed one 3.2 and two 1.5 square degree areas of the inner Galaxy respectively. Green (1993) analyzed a section of the second quadrant

( $l = 140^\circ, b = 0^\circ$ ) located in our survey, using a different technique. Green worked directly with the  $uv$ -plane visibilities. His power-law indices are smaller:  $-\beta = -2.4, -2.4, -2.8$  for the Local, Perseus, and Outer spiral arms and  $-2.5, -3.0$  for the inter-arms, and with larger uncertainties ( $\pm 0.1$  to  $\pm 0.3$ ). Hence Green (1993) found a steepening of the slope for the further H I (Inter II and the Outer arm). The results presented here do not follow a similar trend, either in our complete sample or for the regions corresponding to Green’s fields. This could be explained by the higher sensitivity of the CGPS data and the different scales that were used to derive the slopes (we were very careful not to include the noise affected small scales, see the first paragraph of §5 and Miville-Deschênes et al. (2003)).

Two types of anisotropic structures are detected. For all mosaics (spiral arms and inter-arms), the contribution from the  $y$  component of the wavelet transform ( $T_{\psi_2}$ ) is so great that it dominates the value of the modulus  $\mathcal{M}$ . This greater variability of  $T_{\psi_2}$ , compared to the variability of  $T_{\psi_1}$ , is a first indication of the presence of a structural anisotropy. The study of the directional Hurst exponents for the inter-arms mosaics,  $H_x \sim H_y \sim 0.43$ , implies that these mosaics are rough surfaces with anisotropic properties that do not depend on the scales. In contrast, the spiral arms display anisotropic *scaling* since the directional Hurst exponents are strictly unequal ( $H_x \sim 0.40$  and  $H_y \sim 0.50$ ). Indeed, unlike the study of the synthetic anisotropic surfaces in §4.2 which showed that  $\mathcal{M} \sim a^{\min(H_x, H_y)}$ , the results for the spiral arms show that  $\mathcal{M} \sim a^{\max(H_x, H_y)}$  as the consequence of the greater variability of  $T_{\psi_2}$  as compared to  $T_{\psi_1}$ . (On the range of accessible scales, the scaling behavior of  $\mathcal{M}$  is governed by the power law behavior of  $T_{\psi_2} \sim a^{H_y}$ .) The physical phenomena possibly responsible for the greater fluctuations variability in the vertical ( $y$ ) direction are discussed in §6.2.1.

There is a possibility, albeit small, that the inter-arm regions exhibit multifractal scaling (Figure 27). Some comparisons could be made with the microcalcification aggregates found in dense human breast tissues (Kestener et al. 2001; Kestener 2003). In effect, these latter exhibit a slight departure from monofractality. The 2D WTMM method was used to show that these surfaces consisted of fractal aggregates superposed on a dense background. Such a geometry could be present in the two inter-arm regions. A further study on H I aggregates, possibly corresponding to new star-forming regions, from the two inter-arm regions is required and shall be pursued in the near future.

## 6.2. Astrophysical Discussion

### 6.2.1. Scale-Height Relation

One is tempted to look for a correlation between the results presented here and the scale-height gradient of the Galaxy. In fact, a logical approach would consist in the construction and analysis of synthetic surfaces where such a gradient would be present. For example, the H I vertical distribution from Lockman (1984) could be combined to a monofractal isotropic surface (§4.1). However, the function given in Lockman (1984) consists in the sum of two gaussians and an exponential. Therefore, the “Lockman” function is infinitely differentiable and its roughness (or rather, its smoothness) is thus represented by a Hurst exponent of  $H = \infty$ . The combination of such a function to a 2D fBm surface (where  $H$  is usually  $\in [0, 1]$ ) will not affect calculations of the WTMMM, provided one uses an analyzing wavelet with a sufficiently large number of zero moments, and therefore, will not cause an anisotropic signature.

This does not necessarily mean that the anisotropic signature is not caused by the scale-height (vertical) gradient of the galactic H I. It could very well be. However, it would mean that its distribution could not be given by such a smooth function as the “Lockman” function, but rather by a much more singular mathematical function characterized by a Hurst exponent,  $H$ , in the interval  $[0, 1]$  instead of  $H = \infty$ .

Furthermore, the scale-height gradient could be responsible for the greater variability of the  $y$  (vertical) component of the wavelet transform, which causes the widening of the pdfs of  $T_{\psi_2}$  for all mosaics, and as seen in §5.2.4 and 5.3.4, causes the modulus of the wavelet transform ( $\mathcal{M}$ ) to scale (on the range of accessible scales) like  $\sim a^{\max(H_x, H_y)}$  instead of the theoretically expected  $\sim a^{\min(H_x, H_y)}$ . However, this effect should therefore be expected to increase with distance, which is not the case here.

### 6.2.2. Anisotropy

This study is an attempt at objectively quantifying the global structure of the H I distribution in our Milky Way. Lengths and widths of spiral features, varying from 1 kpc and 35 pc (Local arm) to 7 kpc and 220 pc (Outer arm) were analyzed. However, the Local arm is close enough that the sampled scales may be too small to properly study latitudinal behavior. This may be offset by the finding of Porcel et al. (1998) that the Local arm is more than 70 pc over the plane, probably explaining the similarity of the results shown in Table 2. The following relates the findings on the anisotropy to the gravitational theory of

spiral structure proposed by Lin & Shu (1964, 1966).

It can be demonstrated that interstellar clouds respond strongly to the imposed spiral potential from a density wave (Roberts 1972). An eloquent illustration of this effect can be found in Figure 7b from Toomre (1977), where harmonic oscillations are exposed to a traveling sinusoidal force. The gas particles are neatly piled up at positions imposed by the frequency of the traveling wave. A galaxian density wave can thus be seen as an ordering mechanism since the spiral arms are the locus of lower shear and lower tidal forces from the background galaxy as compared to the inter-arms (Elmegreen 1992). This description falls in line with this paper’s results, where the spiral arms appear to be globally the smoother galactic features (for the accessible range of scales). In the inter-arms, clouds can be broken apart by the larger shear and tidal forces, giving rise to a more irregular latitudinal gas distribution. However, as mentioned in §6.1, the spiral arms display anisotropic *scaling*. The arms are smoother along  $b$  than along  $l$ . In fact, the directional Hurst exponent  $H_x$  (along  $l$ ) is  $\sim 0.4$  whether one considers the arms or the inter-arms. Moreover, the reader should keep in mind that the analysis of the smallest scales ( $a \rightarrow 0^+$ ), which were unavailable here because of the relatively high noise level, would yield similar global Hurst exponents for the arms and inter-arms, i.e.  $H = \min(H_x, H_y) \sim 0.4$  instead of  $H = \max(H_x, H_y)$ .

The roughness of the spiral arms along  $l$  may be explained simply by massive star formation activity and its consequence, supernovae. Indeed, the roughness exponent,  $H$  of the Perseus arm is smaller for values of  $l$  between  $104^\circ \leq l \leq 109^\circ$ , where five sites of active star formation are present (S139, S142, S146, S152, and S153) and the supernova CTB 109. Similarly for the Local arm, where the H II regions S185 and S187 and the supernovae G126.2+1.6 and G127.1+0.5 are coeval<sup>10</sup> within  $123^\circ \leq l \leq 129^\circ$ . Along  $l$ , lines of constant spiral phase are sampled. Therefore, the irregularities in the column density maps are caused either by the “radial” velocity field of galactic rotation or disturbances like supernovae. However, since the galactic rotation velocity field is very smooth, the latter hypothesis is retained as exemplified above.

The relative smoothness of the arms along  $b$  is not easily explained unless the density wave does its ordering role at least up to the scale height of the H I gas ( $\approx 200$  pc) and that the kinematic and density disturbances originating in star formation and supernovae are limited to a very thin portion of the disk. The H I layer being so thin, all the gas may follow an identical mean velocity streaming pattern (spiral arms). Lockman (1984) has shown that the mean velocity of the ISM above the plane lies near the circular speed at the

---

<sup>10</sup>The catalogs of Blitz, Fich & Stark (1982) and D.A. Green’s online catalogue (<http://www.mrao.cam.ac.uk/surveys/snrs/>) were consulted.

corresponding point in the plane for the inner galaxy. Only a process related to spiral arms can be invoked to explain the higher  $H_y$  value.

In addition to the global processes discussed above, there is a number of phenomena that can act on the vertical extent of the gas.

As mentioned in Dickey & Lockman (1990), the kinetic temperature of H I is too low to support it to its observed height against the galactic potential. It could be held up by the photo-levitation of small dusty clouds ( $N < 5 \times 10^{20} \text{ cm}^{-2}$ ) (Franco et al. 1991; Ferrara 1993). The radiation pressure is provided by the interstellar radiation field and would be stronger near star clusters. Hence, it is argued that this phenomena is most likely to occur in the inner galaxy. However, the decreasing galactic potential in the outer galaxy may partly offset this segregation.

Lockman & Gehman (1991) proposed that the random motion of H I clouds, similar to a turbulent pressure, would have enough kinetic energy to rise the H I above the plane. However, this result is not very sensitive to the exact form of the galactic gravitational potential. Again, the high diffusivity associated with this turbulent process cannot be used to explain the arm / inter-arm  $H_y$  difference.

A corrugation effect has been observed in the distribution of H I gas in the spiral arms (Quiroga 1974, 1977; Spicker & Feitzinger 1986). This effect is associated only with the arms and is observed along their length. Every young object is affected (OB stars, H II regions, H I) but not molecular clouds. Arms are displaced alternatively at both sides of the galactic plane. The data is somewhat scarce, but Spicker & Feitzinger (1986) estimate wave patterns at scales  $1 \text{ kpc} < \lambda < 2 \text{ kpc}$ ,  $4 \text{ kpc} < \lambda < 8 \text{ kpc}$ , and  $\lambda > 13 \text{ kpc}$ . None were found for  $\lambda < 1 \text{ kpc}$ . The amplitudes range between 145 and 350 pc, they increase with the thickness of the H I distribution. The physical process at the origin of this phenomenon is unknown. Gravitational instabilities of a galactic or extra-galactic nature, the excitation of the galactic warp, magnetic fields have been brought forward but, to our knowledge, no model has been presented. The scale of our observations (1 to 7 kpc in length) is similar to that of the corrugations. It may be the “smoothing factor” we are looking for if spiral arm kinematics have a minor influence on vertical motion.

Martos & Cox (1998) modeled the interarm-to-arm transition in the Galactic disk. They took a magnetohydrodynamical point of view since gas flows through the spiral perturbation. Under such a view hydraulic bores (jumps in height) ensue as long-lived phenomena since magnetic fields facilitate vertical perturbations. Their calculations predict that the arms will be thicker than the inflowing interarm gas with associated vertical and circulating motions. Their Fig. 15 is a very good illustration of the predicted phenomena. The midplane density

is not uniform showing ridges that may be caused by gravity waves. The difference in large scale anisotropy we measured may be the detection of this phenomena.

Finally, turbulence may have a role to play in the measured anisotropy. Numerous observational and theoretical studies propose the ubiquity of turbulence in the ISM. Its signature has been found in all phases of the ISM (Franco & Carramiñana 1999; Falgarone & Passot 2003) using a large set of different statistical tools (for example see Lazarian & Pogosyan (2004) and references therein). A few groups are tackling the numerical simulation of turbulence in a compressible, magnetized ISM (Mac Low (2003), Vázquez-Semadeni (2003), see also the reviews by Elmegreen & Scalo (2004) and Scalo & Elmegreen (2004) for a more complete list of the relevant literature). The Mexican group (e.g. Passot, Vázquez-Semadeni & Pouquet (1995) and Avila-Reese & Vázquez-Semadeni (2001)) is doing calculations closer to the theme of this paper, i.e., examining if large scale (1 kpc) turbulence (if present) plays a role in the current structure and evolution of the Galaxy. The answer is not definitive yet but results are encouraging and seem to support such a role. In a different work, Wada, Meurer & Norman (2002) have shown through 2D numerical calculations that gravity-driven turbulence in differentially rotating galactic disks reaches a quasi-steady state in a few rotational periods with the energy ( $E(k)$ ) cascade starting at  $\gtrsim 200$  pc. No energy feedback is needed (i.e. supernovae). Hence different studies come up with similar results. However many theoreticians favor shock dominated turbulence instead of a Kolmogorov-like energy cascade. For 2D Kolmogorov turbulence, the cascade follows a slope of  $-5/3$ ; the slope is  $-2$  for shock dominated turbulence. Hence adding supernovae to the Wada, Meurer & Norman (2002) calculations may change the slope and thus the scales at which the phenomena interacts with the gas. Interestingly, work by De Avillez & Mac Low (2002) on chemical mixing in a supernova-driven ISM has shown that turbulent mixing dominates at the same large scales as predicted by Wada, Meurer & Norman (2002), i.e.,  $\sim 100$  pc. If we accept that turbulence has an impact at large galactic scales (see also Scalo & Elmegreen (2004)) it is not clear yet how it would imprint anisotropy on the ISM. In recent papers (Esquivel et al. 2003; Cho & Lazarian 2003, 2005) have shown that the presence of a magnetic field in a turbulent medium would make the turbulent cascade anisotropic. This suggestion on the role of turbulence is an hypothesis that has to be verified since anisotropy has been measured on small scales but not large ones. For example, Roux, Arneodo & Decoster (2000) applied the WTMM method to terrestrial clouds and found exactly such a behavior. Terrestrial clouds have Reynolds numbers close to what we find in the ISM however they are multifractal; large convective roles dominate the large scale dynamic. The best way to test our hypothesis would be to apply the WTMM method to MHD turbulence simulations of the ISM.

Unfortunately, the noise level of the DRAO data is too strong to allow a thorough investigation of the smallest scales ( $a \rightarrow 0^+$ ) of the mosaics, where the number of statistics

(i.e. the number of WTMMM, which behave as  $\sim a^{-2}$ ) are plentiful enough to allow a study of individual sub-regions instead of the averaging methods presented here. With more, cleaner data, one could easily investigate the angle of anisotropy (from the position of the peaks in the pdfs  $P_a(\mathcal{A})$ ) as a function of the galactic longitude (from sub-region to sub-region). Such an analysis could confirm the presence or absence of the corrugation of the H I in the galactic plane.

## 7. CONCLUSION

### 7.1. The Galactic H I

The 2D WTMM method was used to analyze five H I column densities mosaics, corresponding to the Local, Perseus, and Outer spirals and the two inter-arm regions in between.

The formalism was first tested on synthetic surfaces. It was shown that the 2D WTMM method could quantitatively characterize isotropic monofractal and multifractal surfaces, as well as anisotropic monofractal surfaces with great accuracy. The characterization of anisotropic structures, by way of the directional Hurst exponents  $0 \leq H_x, H_y \leq 1$  is novel.

The results presented in this paper show that the roughness of the H I mosaics, as characterized by the global Hurst exponent,  $H$ , looks stronger in the inter-arm regions than in the spiral arms. However, having access to the smallest scales would yield similar global Hurst exponents for both arms and inter-arms. The main difference between arms and inter-arms is the discovery of two types of anisotropic structures. For the spiral arms, the anisotropic signature is scale-dependent while it is scale-independent for the inter-arms. Indeed, the spiral arms have different directional Hurst exponents ( $H_x \sim 0.4$  and  $H_y \sim 0.5$ ) while the inter-arms have similar directional Hurst exponents ( $H_x \sim H_y \sim 0.43$ ). The anisotropic signature found in the inter-arms is caused only by the vertical distribution of the H I, which is much more variable than the horizontal distribution.

Several hypotheses were investigated to provide a physical explanation: the scale-height gradient, the density wave, star formation activity, photo-levitation of dusty clouds, random motion of H I clouds, corrugation, and turbulence.

### 7.2. Future Work

The synthetic surfaces presented in §4 were only used to test and calibrate the 2D WTMM methodology. They are not presented as potential models of spiral or inter-arms.

However, a future study will be dedicated to the construction of algorithms capable of modelling the mosaics presented here. By imposing a greater variability (for the fluctuations) in the vertical ( $y$ ) direction than in the horizontal ( $x$ ) direction, one should be able to obtain  $\mathcal{M} \sim a^{\max(H_x, H_y)}$  on the same range of scales that were available here, while the analysis of the smallest scales ( $a \rightarrow 0^+$ ) would yield  $\mathcal{M} \sim a^{\min(H_x, H_y)}$ . Such an analysis will provide two very interesting models (spiral and inter arms) of column density mosaics. Furthermore, the study of these models could help understand the physical processes responsible for the quantitative fractal and anisotropic properties discussed in this paper.

The “Lockman” scale-height function should be investigated to find out whether or not it can be mathematically changed to a more singular (fractal) version, where  $H \in [0, 1]$ , instead of the actual, infinitely smooth version ( $H = \infty$ ). Such a new function could, at least partly, explain the anisotropic signature found in the H I mosaics.

An exploration of the recently observed “Cepheus flare” extension of the CGPS will yield very interesting complementary results for high-latitude H I structures ( $5^\circ \lesssim b \lesssim 17^\circ$ ).

Many thanks to M.A. Miville-Deschênes for providing us the IDL codes for the “à trous” filtering method and L. Nadeau for the production of the mosaics. A.K. and G.J. acknowledge support from the Natural Sciences and Engineering Council of Canada and the Fonds de Recherche sur la Nature et les Technologies du Québec. A.K. also acknowledges support from NASA prime contract task order number NMO710837 as well as NSF/EPSCoR 0132384.

## REFERENCES

- Abergel, A., Boulanger, F., Delouis, J. M., Dudziak, G., & Steindling, S. 1996, *A&A*, 309, 245
- Arneodo, A., Grasseau, G., & Holschneider, M. 1988, *Phys. Rev. Lett.*, 61, 2281
- Arneodo, A., Argoul, F., Bacry, E., Elezgaray, J., & Muzy, J.F. 1995a, *Ondelettes, Multifractales et Turbulences: de l'ADN aux croissances cristallines* (Paris: Didérot)
- Arneodo, A., Bacry, E., & Muzy, J.F. 1995, *Physica A*, 213, 232
- Arneodo, A. 1996, in *Wavelets: Theory and Applications*, eds. G. Erlebacher, M.Y. Hussaini, L.M. Jameson (Oxford: Oxford University Press), p. 349
- Arneodo, A., Decoster, N., & Roux, S.G. 1999, *Phys. Rev. Lett.*, 83, 1255
- Arneodo, A., Decoster, N., & Roux, S.G. 2000, *Eur. Phys. J. B*, 15, 567
- Arneodo, A., Audit, B., Decoster, N., Muzy, J.F., & Vaillant, C. 2002, in *Bunde et al. (2002)*, p.27
- Arrault, J., Arneodo, A., Davis, A., & Marshak, A. 1997, *Phys. Rev. Lett.*, 79, 75
- Audit, B., Bacry, E., Muzy, J.F., & Arneodo, A. 2002, *IEEE Trans. on Info. Theory*, 48, 2938
- Avila-Reese, V. & Vázquez-Semadeni, E. 2001, *ApJ*, 553, 645
- Bacry, E., Arneodo, A., Frisch, U., Gagne, Y., & Hopfinger, E. 1991 in *Turbulence and Coherent Structures*, eds. M. Lesieur, O. Metais (Dordrecht, Kluwer), p.203
- Bacry, E., Muzy, J.F., & Arneodo, A. 1993, *J. Stat. Phys.*, 70, 635
- Badii, R. & Politi, A. 1985, *J. Stat. Phys.*, 40, 725
- Bazell, D. & Désert, F.X. 1988, *ApJ*, 333, 353
- Besicovitch, A.S. 1935, *Mathematische Annalen*, 110, 321
- Binney, J., & Merrifield, M. 1998, *Galactic Astronomy* (Princeton : Princeton University Press)
- Blitz, L., Fich, M., & Stark, A.A. 1982, *ApJS*, 49, 183

- Burton, W.B. 1976, *ARA&A*, 14, 275
- Chappell, D. & Scalo, J. 2001, *ApJ*, 551, 712
- Cho, J. & Lazarian, A. 2003, *MNRAS*, 345, 325
- Cho, J. & Lazarian, A. 2005, *ApJ*, 631, 361
- Crovisier, J. & Dickey, J.M. 1983, *A&A*, 122, 282
- De Avillez, M.A. & Mac Low, M.M. 2002, *ApJ*, 581, 1047
- Decoster, N. 1999, Ph.D. Thesis, Université Bordeaux I
- Decoster, N., Roux, S.G., & Arneodo, A. 2000, *Eur. Phys. J. B*, 15, 739
- Dickey, J.M. & Lockman, F.J. 1990, *ARA&A*, 28, 215
- Dickey, J.M., McClure-Griffiths, N.M., Stanimirovic, S., Gaensler, B.M., & Green, A.J. 2001, *ApJ*, 561, 264
- Dickman, R.L., Horwath, M.A., & Margulis, M. 1990, *ApJ*, 365, 586
- Dubuc, B., Quiniou, J.F., Roques-Carmes, C., Tricot, C., & Zucher, S.W. 1989, *Phys. Rev. A*, 39, 1500
- Elmegreen, B.G. 1992, in *The Galactic Interstellar Medium*, eds. D. Pfenniger & P. Bartholdi (Berlin: Springer), 157
- Elmegreen, B.G., & Falgarone, E. 1996, *ApJ*, 471, 816
- Elmegreen, B.G., Kim, S. & Stavelly-Smith, L. 2001, *ApJ*, 548, 749
- Elmegreen, B.G., Elmegreen, D.M. & Leitner, S.N. 2003, *ApJ*, 590, 271
- Elmegreen, B.G., & Scalo, J. 2004, *ARA&A*, 42, 211
- Esquivel, A., Lazarian, A., Pogosyan, D. & Cho, J. 2003, *MNRAS*, 342, 325
- Falgarone, E. 1989, in *Structure and Dynamics of the Interstellar Medium*, eds. G. Tenorio-Tagle, M. Moles, & J. Melnick (Berlin: Springer), p.68
- Falgarone, E., & Phillips, T.G. 1990, *ApJ*, 359, 399
- Falgarone, E., Phillips, T.G., & Walker, C.K. 1991, *ApJ*, 378, 186

- Falgarone, E. & Passot, J. 2003, *Turbulence and Magnetic Fields in Astrophysics* (Berlin: Springer)
- Feder, J. 1988, *Fractals* (New York: Plenum Press)
- Ferrara, A. 1993, *ApJ*, 407, 157
- Flandrin, P., Abry, P., & Goncalvès, P. 2002, in *Lois d'Échelle, Fractales et Ondelettes*, eds. P. Abry, P. Goncalvès, & J. Lévy-Véhel (Paris: Hermès)
- Franco, J., Ferrini, F., Ferrara, A. & Barsella, B. 1991, *ApJ*, 366, 443
- Franco, J. & Carramiñana, A. 1999, *Interstellar Turbulence* (Cambridge: Cambridge University Press)
- Frisch, U. 1995, *Turbulence* (Cambridge: Cambridge University Press)
- Gibson, S. & Stil, J. 2002, *Bull. AAS*, 34, 1187
- Gill, A.G. & Henriksen, R.N. 1990, *ApJ*, 365, 27
- Gill, A.G. 1993, Ph.D. Thesis, Queens University, Kingston, Ontario, Canada
- Goupillaud, P., Grossmann, A., & Morlet, J. 1984, *Geoexploration* 23, 85
- Green, D.A. 1993, *MNRAS*, 262, 327
- Grossmann, A. & Morlet, J. 1984, *SIAM J. Math. Anal.*, 15, 723
- Halsey, T.C., Jensen, M.H., Kadanoff, L.P., Proccacia, I., & Shraiman, B.I. 1986, *Phys. Rev. A*, 33, 1141
- Hausdorff, F. 1919, *Mathematische Annalen*, 79, 157
- Hetem, A. & Lépine, J.R.D. 1993, *A&A*, 270, 451
- Jaffard, S. & Meyer, Y. 1996, *Memoirs A.M.S.*, 123, 587
- Kestener, P., Lina, J.M., Saint-Jean, P., & Arneodo, A. 2001, *Image Anal. Stereol.*, 20, 169
- Kestener, P. 2003, Ph.D. Thesis, Université de Bordeaux I.
- Khalil, A., Joncas, G., & Nekka, F. 2004, *ApJ*, 601, 352
- Khalil, A. 2006, in preparation

- Kolmogorov, A.N. 1958, Dokl. Akad. Nauka USSR, 119, 861
- Langer, W.D., Wilson, R.W., & Anderson, C.H. 1993, ApJ, 408, 45
- Lazarian, A. & Pogosyan, D. 2004, ApJ, 616, 943
- Lea-Cox, B. & Wang, J.S.Y. 1993, Fractals, 1, 87
- Li, J., Arneodo, A., & Nekka, F. 2004, to appear in December 2004 issue of Chaos: An Interdisciplinary Journal of Nonlinear Sciences
- Lin, C.C. & Shu, F.H. 1964, ApJ, 140, 646
- Lin, C.C. & Shu, F.H. 1966, Proc. Nat. Acad. Sci. USA, 55
- Lockman, F.J. 1984, ApJ, 283, 90
- Lockman, F.J. & Gehman, C.S. 1991, ApJ, 382, 182
- Mac Low, M.-M. 2003, Turbulence and Magnetic Fields in Astrophysics, ed. by Edith Falgarone and Thierry Passot (Berlin:Springer), 182
- Maisinger, K., Hobson, M.P., & Lasenby, A.N. 2003, MNRAS, 347, 339
- Makse, H.A., Havlin, S., Schwartz, M., & Stanley, H.E. 1996, Phys. Rev. E, 53, 5445
- Mallat, S. & Zhong, S. 1992, IEEE Trans. on Pattern Analysis and Machine Intelligence, 14, 710
- Mallat, S. & Hwang, W.L. 1992, IEEE Trans. on Information Theory, 38, 617
- Mallat, S. 1998, A Wavelet Tour of Signal Processing (New York: Academic Press)
- Mandelbrot, B.B. & Van Ness, J.W. 1968, SIAM Rev., 10, 422
- Mandelbrot, B.B. 1974a, C. R. Acad. Sci. Paris Ser. A, 278, 289, 355
- Mandelbrot, B.B. 1974b, J. Fluid Mech., 62, 331
- Mandelbrot, B.B. 1977, Fractals: Form, Chance and Dimensions (Freeman: San Francisco)
- Mandelbrot, B.B. 1982, The Fractal Geometry of Nature (Freeman: San Francisco)
- Martos, M.A. & Cox, D.P. 1998, ApJ, 509, 703
- Miville-Deschênes, M.A., Joncas, G., Falgarone, E., & Boulanger, F. 2003, A&A, 411, 109

- Miville-Deschênes, M.A., Levrier, F., & Falgarone, E. 2003, *ApJ*, 593, 831
- Monin, A.S. & Yaglom, A.M. 1975, *Statistical Fluid Mechanics*, Vol. 2 (Cambridge, MA: MIT Press)
- Montseny, G. 2004, in preparation
- Muzy, J.F., Bacry, E., & Arneodo, A. 1991, *Phys. Rev. Lett.*, 67, 3515
- Muzy, J.F., Bacry, E., & Arneodo, A. 1993, *Phys. Rev. E*, 47, 875
- Muzy, J.F., Bacry, E., & Arneodo, A. 1994, *Int. J. of Bifurcation and Chaos*, 4, 245
- Parisi, G. & Frisch, U. 1985, in *Turbulence and Predictability in Geophysical Fluid Dynamics and Climate Dynamics*, Proc. of Int. School, eds. M. Ghil, R. Benzi, & G. Parisi (Amsterdam: North-Holland), p.84
- Passot, T., Vázquez-Semadeni, E. & Pouquet, A. 1995, *ApJ*, 455, 536
- Peitgen, H.O. & Saupe, D. (eds) 1988, *The Science of Fractal Images* (New York: Springer-Verlag)
- Pesquet-Popescu, B. & Lévy Véhel, J. 2002, *IEEE Signal Processing Magazine*, 19, 5, 48
- Pontrjagin, L. & Schnirelman, L. 1932, *Annals of Math.*, 33, 156
- Porcel, C., Garzon, F., Jimenez-Vicente, J., & Battavier, E. 1998, *A&A*, 332, 71
- Quiroga, R.J. 1974, *Ap&SS*, 27, 323
- Quiroga, R.J. 1977, *Ap&SS*, 50, 281
- Roberts, W.W. 1972, *ApJ*, 173, 259
- Rohlfs, K. 1974, *A&A*, 35, 177
- Roux, S.G., Arneodo, A., & Decoster, N. 2000, *Eur. Phys. J. B*, 15, 765
- Scalo, J. 1987, in *Interstellar Processes*, eds. D. J. Hollenbach & H. A. Thronson (Dordrecht: Kluwer), p.349
- Scalo, J. 1990, in *Physical Processes in Fragmentation and Star Formation*, eds. R. Capuzzo-Dolcetta, C. Chiosi, & A. DiFazio (Dordrecht: Kluwer), p.151
- Scalo, J. & Elmegreen, B.G. 2004, *ARA&A*, 42, 275

- Schertzer, D. & Lovejoy, S. 1985, *Phys. Chem. Hyd. J.*, 6, 623
- Schertzer, D. & Lovejoy, S. 1987, *J. Geophys. Res.*, 92, 9693
- Schertzer, D., Lovejoy, S., Schmitt, F., Ghigisinskaya, Y., & Marsan, D. 1997, *Fractals*, 5, 427
- Schmittbuhl, J., Violette, J.P., & Roux, S.G. 1995, *Phys. Rev. E*, 51, 131
- Scotti, A., Meneveau, C., & Saddoughi, S.G. 1995, *Phys. Rev. E*, 51, 5594
- Simonson, S.C. 1976, *A&A*, 46, 261
- Sornette, D. 2000, in *Critical Phenomena in Natural Sciences. Chaos, Fractals, Self-Organization and Disorder: Concepts and Tools*, Series in Synergetics, ed. H. Haken (Berlin: Springer-Verlag)
- Spicker, J., & Feitzinger, J.V. 1986, *A&A*, 163, 43
- Stanimirovic, S., Staveley-Smith, L., Sault, R.J., Dickey, J., & Snowden, S. 1998, *IAUS*, 190, 61
- Stanimirovic, S. & Lazarian, A. 2001, *ApJ*, 551, L53
- Stutzki, J., Bensch, F., Heithausen, A., Ossenkopf, V., & Zielinsky, M. 1998, *A&A*, 336, 697
- Taylor, A.R. et al. 2003, *AJ*, 125, 3145
- Toomre, A. 1977, *ARA&A*, 15, 437
- Vázquez-Semadeni, E. 2003, in *Turbulence and Magnetic Fields in Astrophysics*, eds. Edith Falgarone & Thierry Passot (Berlin:Springer), 213
- Vergassola, M., Benzi, R., Biferale, L., & Pisarenko, D. 1993, *J. Phys. A*, 26, 6093
- Vicsek, T. 1989, *Fractal Growth Phenomena* (Singapore: World Scientific)
- Vogelaar, M.G.R., & Wakker, B.P. 1994, *A&A*, 291, 557
- Wada, K., Meurer, G., & Norman, C.A. 2002, *ApJ*, 577, 197
- West, B.J. 1990, *Fractal Physiology and Chaos in Medicine* (Singapore: World Scientific)
- Westpfahl, D.J., Coleman, P.H., Alexander, J., & Tongue, T. 1999, *AJ*, 117, 868

Table 1. Five H I Mosaics

Mosaic	Distance (pc)	Galactic Longitude (°)	Velocity Range (km/s)
Local	~ 1000	[98, 146]	[0.19, -20.43]
Inter I	~ 2500	[98, 146]	[-20.43, -34.44]
Perseus	~ 3500	[98, 146]	[-34.44, -50.11]
Inter II	~ 4700	[98, 115]	[-77.31, -88.03]
		[115, 119]	[-74.02, -83.08]
		[119, 123]	[-71.54, -81.44]
		[123, 127]	[-69.07, -78.96]
		[127, 130]	[-66.60, -76.49]
		[130, 146]	[-64.12, -74.84]
		[98, 103]	[-88.86, -111.12]
Outer	~ 6300	[103, 107]	[-88.86, -107.82]
		[107, 111]	[-88.86, -105.35]
		[111, 115]	[-88.86, -102.05]
		[115, 119]	[-83.91, -100.40]
		[119, 123]	[-82.26, -97.10]
		[123, 127]	[-79.79, -95.45]
		[127, 130]	[-77.31, -92.15]
[130, 146]	[-74.02, -85.56]		

Table 2. Hurst Exponents for the Five H I Mosaics

Mosaic	Distance (pc)	Physical Scale <sup>a</sup> (pc)	Global $H$ (Gau) ( $\pm 0.03$ )	$(H_x, H_y)$ (Gau) ( $\pm 0.03$ )	$(H_x, H_y)$ (Mex) ( $\pm 0.03$ )
Local	$\sim 1000$	$\sim 2 - 4$	0.52	(0.42, 0.52)	(0.41, 0.52)
Inter I	$\sim 2500$	$\sim 6 - 16$	0.44	(0.45, 0.44)	(0.41, 0.43)
Perseus	$\sim 3500$	$\sim 8 - 24$	0.53	(0.42, 0.52)	(0.40, 0.50)
Inter II	$\sim 4700$	$\sim 11 - 43$	0.45	(0.42, 0.45)	(0.42, 0.45)
Outer	$\sim 6300$	$\sim 14 - 44$	0.51	(0.43, 0.52)	(0.41, 0.48)

*a. Range of physical scales used to estimate the scaling exponents with the 2D WTMM method.*

Table 3. Power Spectral Indices as a Function of the Number of Velocity Channels for the Local Arm H I Mosaic over the range  $1 \lesssim \log_2(k) \lesssim 4$

# of Channels	Avg $\beta$ from ind. slopes	$\sigma$	$\beta$ from avg slopes
1	2.98	0.22	$2.98 \pm 0.08$
2	3.02	0.20	$3.02 \pm 0.08$
3	3.02	0.17	$3.02 \pm 0.08$
4	3.01	0.14	$3.01 \pm 0.08$
5	3.00	0.12	$3.00 \pm 0.09$
6	2.98	0.12	$2.98 \pm 0.09$
7	2.97	0.12	$2.97 \pm 0.10$
8	2.97	0.13	$2.97 \pm 0.10$
9	2.97	0.13	$2.97 \pm 0.09$
10	2.97	0.13	$2.97 \pm 0.09$
11	2.97	0.13	$2.97 \pm 0.09$
12	2.97	0.12	$2.97 \pm 0.09$
13	2.97	0.12	$2.97 \pm 0.09$
14	2.97	0.11	$2.97 \pm 0.09$
15	2.98	0.10	$2.98 \pm 0.09$
16	2.98	0.11	$2.98 \pm 0.10$
17	2.99	0.11	$2.99 \pm 0.10$
18	2.99	0.10	$2.99 \pm 0.10$
19	3.00	0.08	$2.99 \pm 0.10$
20	2.99	0.06	$2.99 \pm 0.10$
21	2.99	0.06	$2.99 \pm 0.10$
22	2.98	0.06	$2.98 \pm 0.10$
23	3.00	0.07	$3.00 \pm 0.10$
24	2.98	0.07	$2.98 \pm 0.10$
25	2.98	0.07	$2.98 \pm 0.10$
26	2.98	0.07	$2.98 \pm 0.10$



Table 4. Power Spectral Indices as a Function of the Number of Velocity Channels for the Local Arm H I Mosaic over the range  $1 \lesssim \log_2(k) \lesssim 5$

# of Channels	Avg $\beta$ from ind. slopes	$\sigma$	$\beta$ from avg slopes
11	2.93	0.15	$2.93 \pm 0.05$
12	2.91	0.15	$2.91 \pm 0.05$
13	2.91	0.14	$2.91 \pm 0.05$
14	2.92	0.12	$2.92 \pm 0.05$
15	2.93	0.11	$2.93 \pm 0.05$
16	2.94	0.10	$2.94 \pm 0.05$
17	2.95	0.09	$2.95 \pm 0.05$
18	2.96	0.09	$2.96 \pm 0.05$
19	2.96	0.08	$2.96 \pm 0.05$
20	2.95	0.07	$2.95 \pm 0.05$
21	2.96	0.07	$2.96 \pm 0.05$
22	2.96	0.07	$2.96 \pm 0.05$
23	2.95	0.08	$2.95 \pm 0.05$
24	2.95	0.08	$2.95 \pm 0.05$
25	2.95	0.08	$2.95 \pm 0.05$
26	2.95	0.07	$2.95 \pm 0.05$

Table 5. Power Spectral Indices for the Five H I Mosaics

Mosaic	Avg $\beta$ from ind. slopes	$\sigma$	Smallest $\beta$	Largest $\beta$	$\beta$ from avg slopes
Local	2.95	0.07	$2.80 \pm 0.06$	$3.10 \pm 0.08$	$2.95 \pm 0.05$
Inter I	2.93	0.08	$2.78 \pm 0.04$	$3.08 \pm 0.06$	$2.93 \pm 0.05$
Perseus	2.97	0.10	$2.81 \pm 0.04$	$3.19 \pm 0.05$	$2.97 \pm 0.04$
Inter II	2.94	0.09	$2.80 \pm 0.06$	$3.09 \pm 0.06$	$2.94 \pm 0.05$
Outer	2.94	0.06	$2.89 \pm 0.08$	$3.08 \pm 0.07$	$2.94 \pm 0.05$

*The values for the  $\beta$  indices were taken from the fitted slopes of the power spectra, over the range  $1 \lesssim \log_2(k) \lesssim 5$ .*

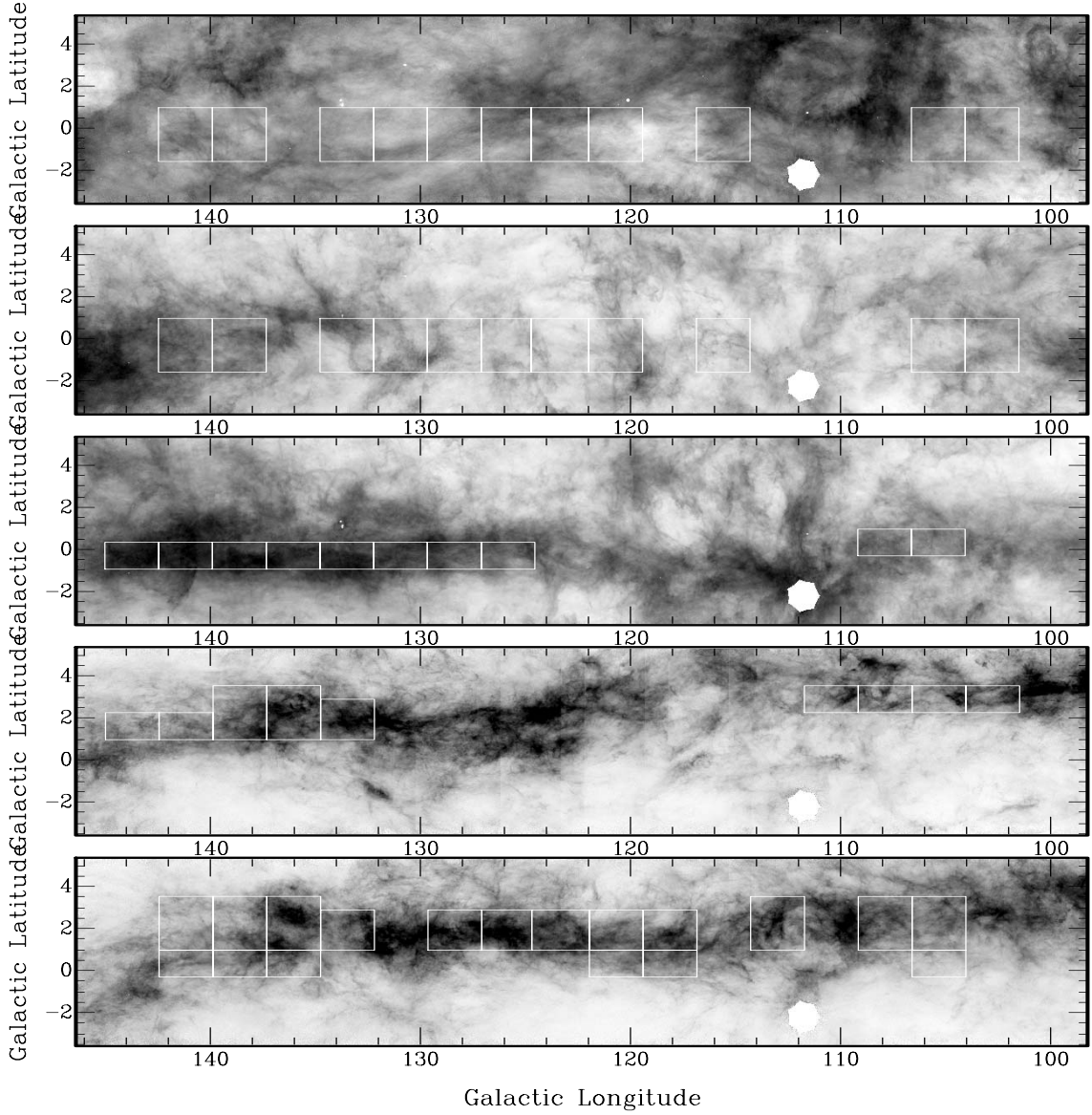


Fig. 1.— From top to bottom, the mosaics Local, Inter I, Perseus, Inter II, and Outer. The range of intensities (from white to black), which vary from one mosaic to another, are  $[22, 85]$ ,  $[2, 87]$ ,  $[2, 103]$ ,  $[0, 50]$ , and  $[0, 41]$   $\text{K km s}^{-1}$  respectively. White rectangles represent the sub-areas analyzed (see text for a discussion on the choice of these sub-areas).

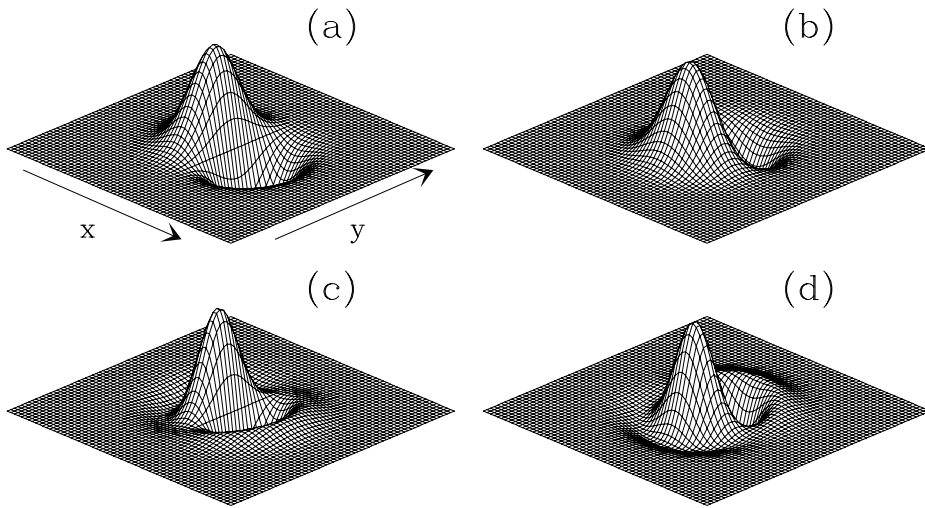


Fig. 2.— The first-order analyzing wavelets (a)  $\psi_1$  and (b)  $\psi_2$  defined in §3.1, obtained from a Gaussian smoothing function  $\phi_{\text{Gau}}$  (Eq. (1)). Third-order analyzing wavelets (c)  $\psi_1$  and (d)  $\psi_2$  defined in §3.1, obtained from the Mexican hat smoothing function  $\phi_{\text{Mex}}$  (Eq. (4)). Figure taken from Arneodo, Decoster & Roux (2000).

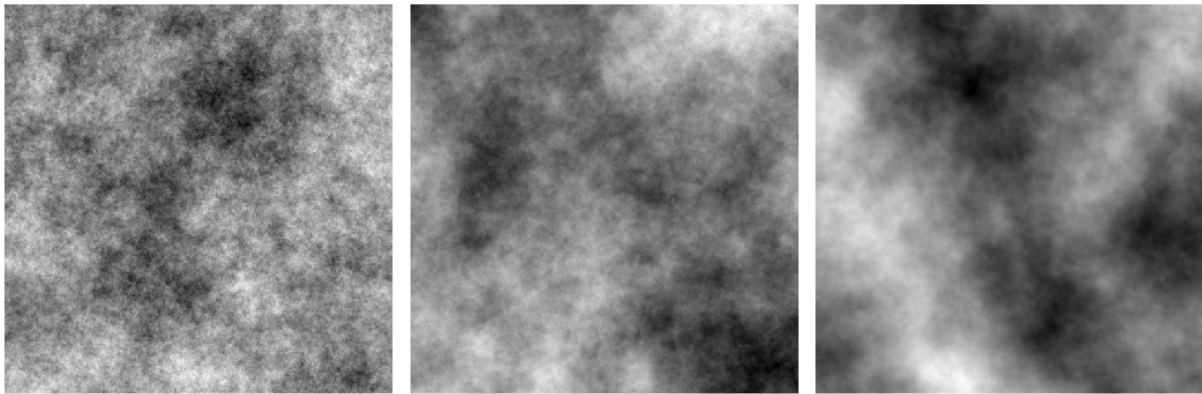


Fig. 3.— FBm surfaces  $B_H(\mathbf{x})$  generated with the Fourier transform filtering synthesis method.  $H = 0.2$  (left);  $H = 0.5$  (center);  $H = 0.8$  (right).

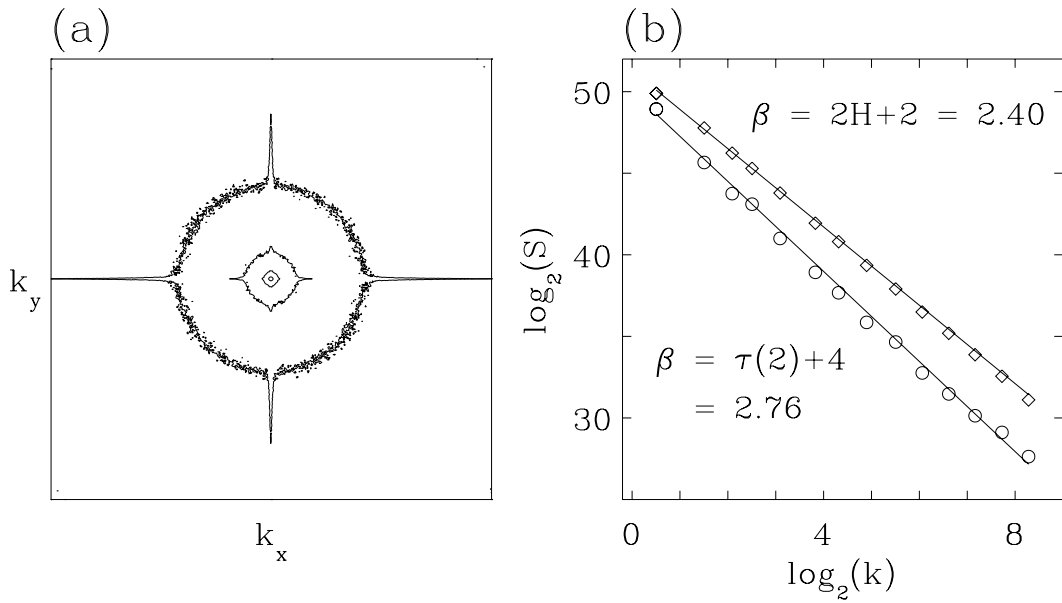


Fig. 4.— Fourier analysis of the  $512 \times 512$  central parts of 32 ( $1024 \times 1024$ ) monofractal and multifractal rough surfaces. (a) Some contour plots of  $\ln|\hat{B}_{0.2}(\mathbf{k})|$ . (b) The power spectrum  $S(|\mathbf{k}|)$  vs  $|\mathbf{k}|$  in a logarithmic representation for the fBm surfaces  $B_{H=0.2}(\mathbf{x})$  ( $\diamond$ ) and the multifractal surfaces ( $\circ$ ) respectively. The solid lines correspond to the power-law theoretical predictions. In (b), the curve corresponding to the multifractal surfaces ( $\circ$ ) was shifted vertically.

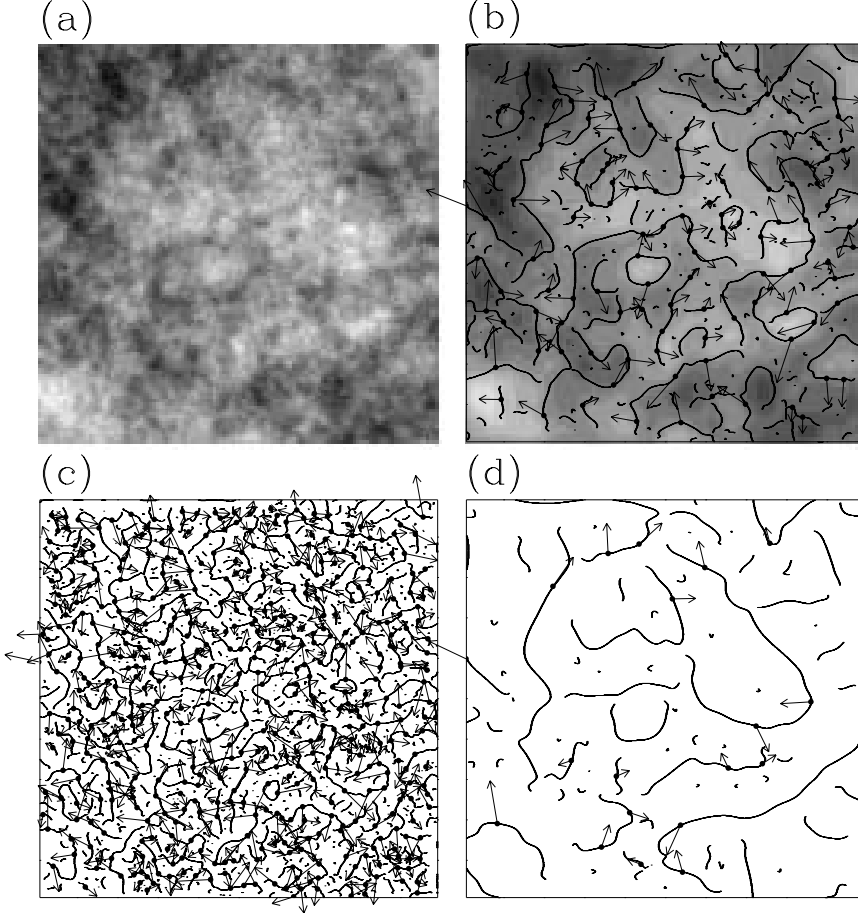


Fig. 5.— 2D wavelet transform analysis of  $B_{H=0.2}(\mathbf{x})$ .  $\psi$  is a first-order radially symmetric analyzing function (see Fig. 2). (a) 32 grey-scale coding of the original image. In (b)  $a = 2^{2.9}\sigma_W$ , (c)  $a = 2^{1.9}\sigma_W$  and (d)  $a = 2^{3.9}\sigma_W$  (where  $\sigma_W = 13$  pixels), are shown the maxima chains; the local maxima of  $\mathcal{M}_\psi$  along these chains are indicated by  $(\bullet)$  from which originate an arrow whose length is proportional to  $\mathcal{M}_\psi$  and its direction (with respect to the  $x$ -axis) is given by  $\mathcal{A}_\psi$ . In (b), the smoothed image  $\phi_{\mathbf{b},a} * B_{H=0.2}$  (Eq. (3)) is shown as a grey-scale coded background from white (min) to black (max).

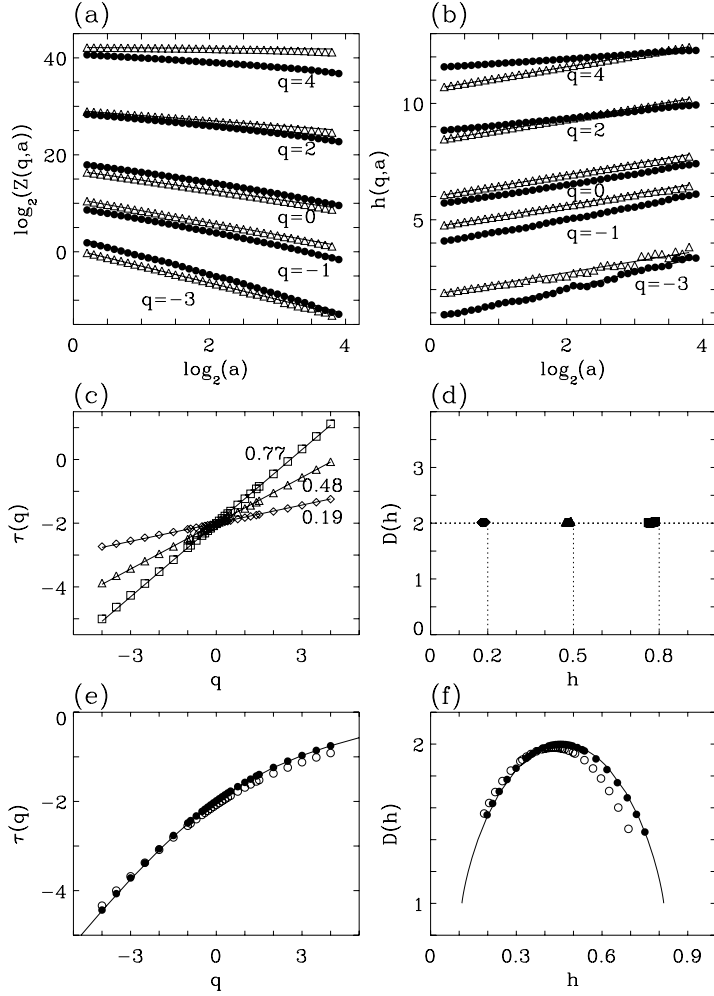


Fig. 6.— Determination of the  $\tau(q)$  and  $D(h)$  spectra of 2D fBm  $B_H(\mathbf{x})$  ( $\diamond, \triangle, \square$ ) and multifractal ( $\circ, \bullet$ ) rough surfaces with the 2D WTMM method. (a)  $\log_2 Z(q, a)$  vs  $\log_2 a$ ; (b)  $h(q, a)$  vs  $\log_2 a$ . The solid lines in (a) and (b) correspond to the theoretical predictions. (c)  $\tau(q)$  vs  $q$  for  $B_H(\mathbf{x})$  with  $H = 0.2$  ( $\diamond$ ),  $0.5$  ( $\triangle$ ) and  $0.8$  ( $\square$ ); the solid lines correspond to linear regression fit estimates of  $H$ . (d)  $D(h)$  vs  $h$  for  $B_H(\mathbf{x})$  as obtained from the scaling behavior of  $h(q, a)$  and  $D(q, a)$  vs  $\log_2 a$  (Eqs. (20) and (21)); the symbols have the same meaning as in (c). (e)  $\tau(q)$  vs  $q$  for the multifractal surfaces. (f)  $D(h)$  vs  $h$  for the multifractal surfaces. The solid lines in (e) and (f) correspond to the theoretical spectrum and its Legendre transform respectively. The analyzing wavelet is the first-order ( $\diamond, \triangle, \square, \circ$ ) and third-order ( $\bullet$ ) radially symmetric analyzing wavelets defined in Figure 2. These results correspond to an averaging over 32 ( $1024 \times 1024$ ) images.  $a$  is expressed in  $\sigma_W$  units, with  $\sigma_W = 13$  pixels. In (a) and (b), all curves were shifted vertically.

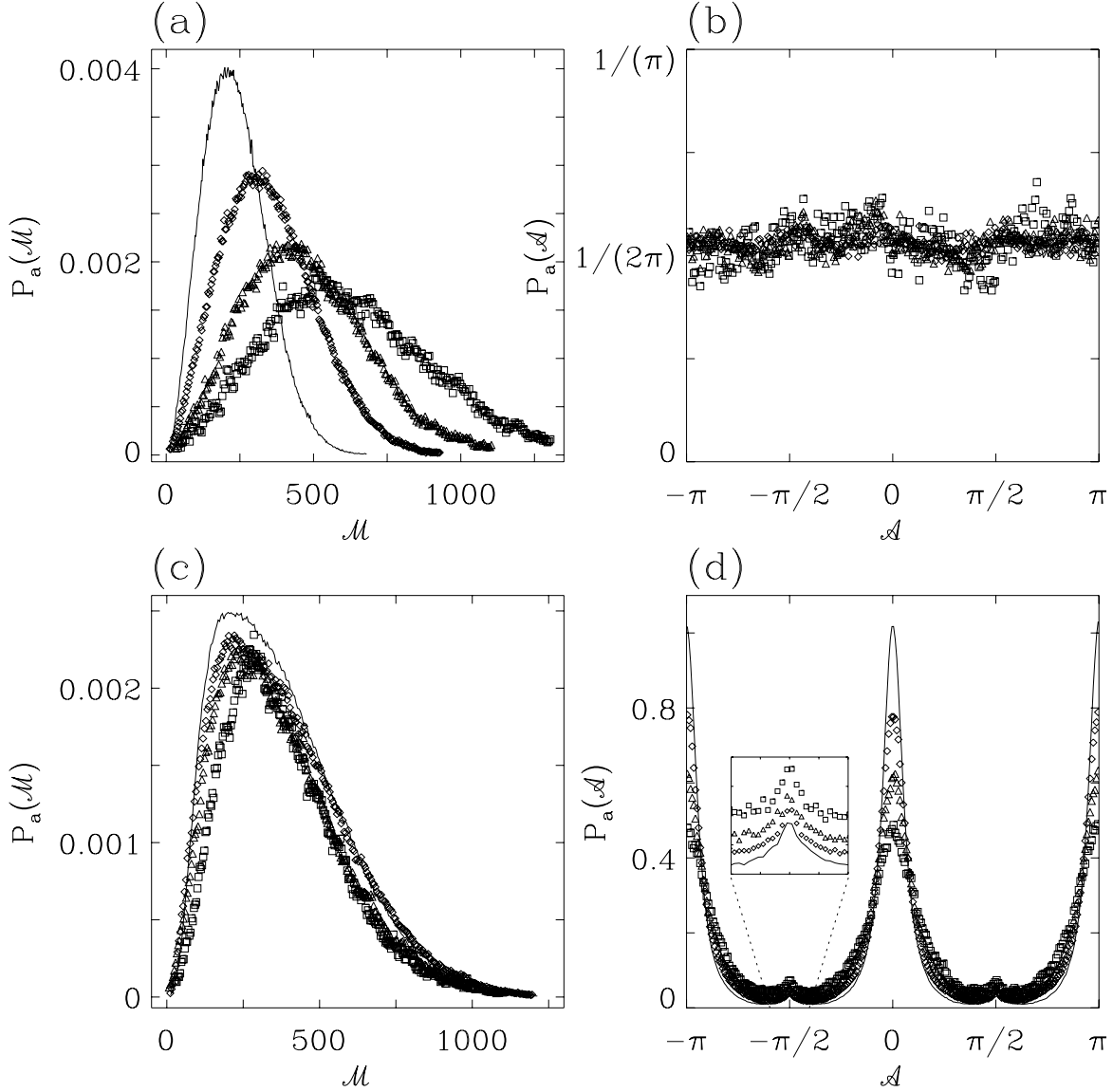


Fig. 7.— Pdfs of the WTMMM coefficients as computed at different scales  $a = 1$  (full line), 2 ( $\diamond$ ), 4 ( $\triangle$ ), 8 ( $\square$ ) (in  $\sigma_W = 13$  units) with the first-order analyzing wavelet shown in Figure 2. FBM rough surfaces  $B_{H=0.2}(\mathbf{x})$ : (a)  $P_a(\mathcal{M})$  vs  $\mathcal{M}$ ; (b)  $P_a(\mathcal{A})$  vs  $\mathcal{A}$ . FBs anisotropic surfaces  $B_{H_x=0.10, H_y=0.50}(\mathbf{x})$ : (c)  $P_a(\mathcal{M})$  vs  $\mathcal{M}$ ; (d)  $P_a(\mathcal{A})$  vs  $\mathcal{A}$ . These results correspond to averaging over 32 ( $1024 \times 1024$ ) images.

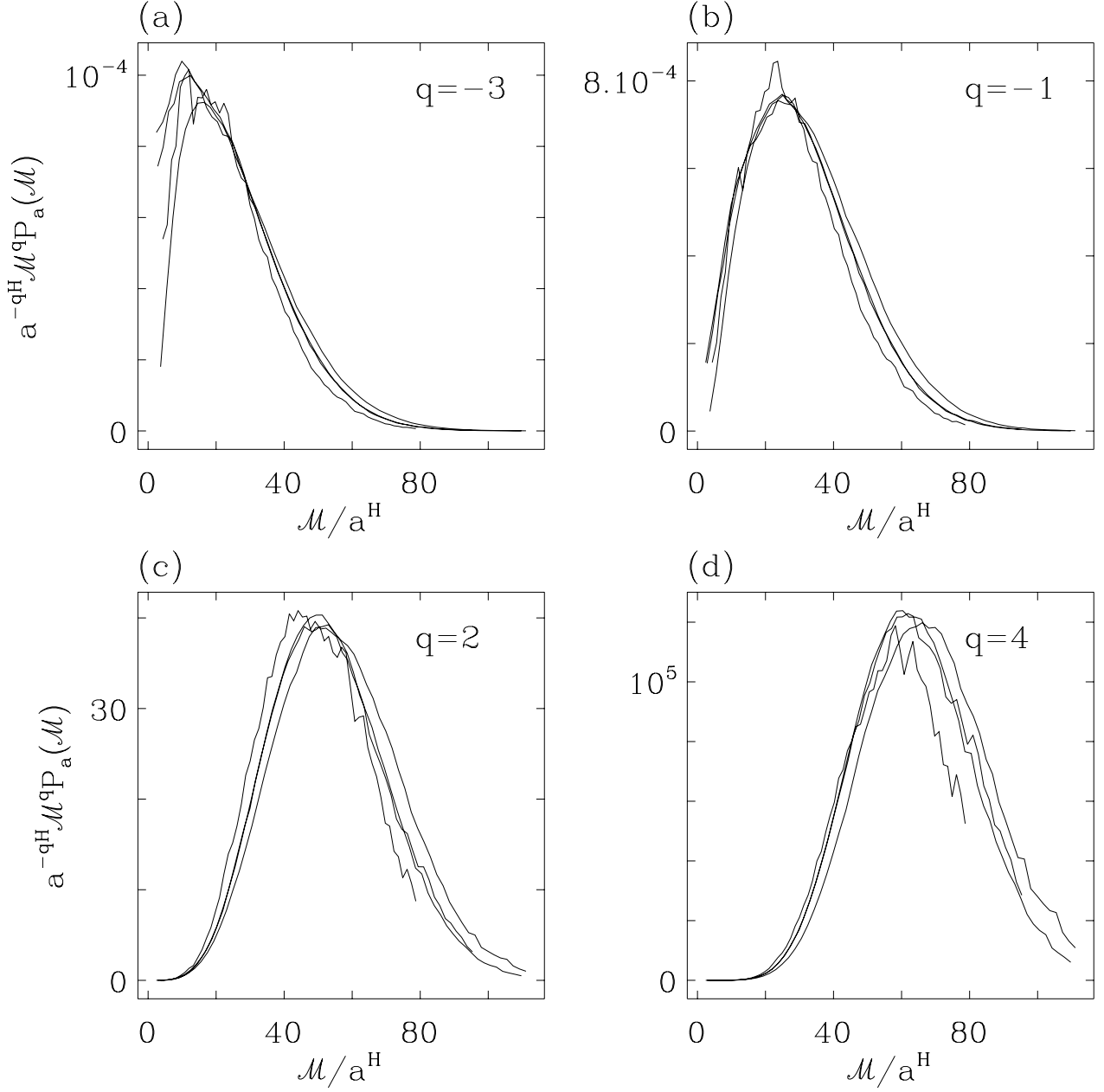


Fig. 8.— Pdfs of the WTMM coefficients of  $B_{H=0.2}(\mathbf{x})$  as computed at different scales  $a = 1, 2, 4, 8$  (in  $\sigma_W = 13$  units).  $a^{-qH} \mathcal{M}^q P_a(\mathcal{M})$  vs  $\mathcal{M}/a^H$  for  $q = -3$  (a),  $q = -1$  (b),  $q = 2$  (c), and  $q = 4$  (d). Same 2D WTMM computations for  $B_{H=0.2}(\mathbf{x})$  as in Figure 7.

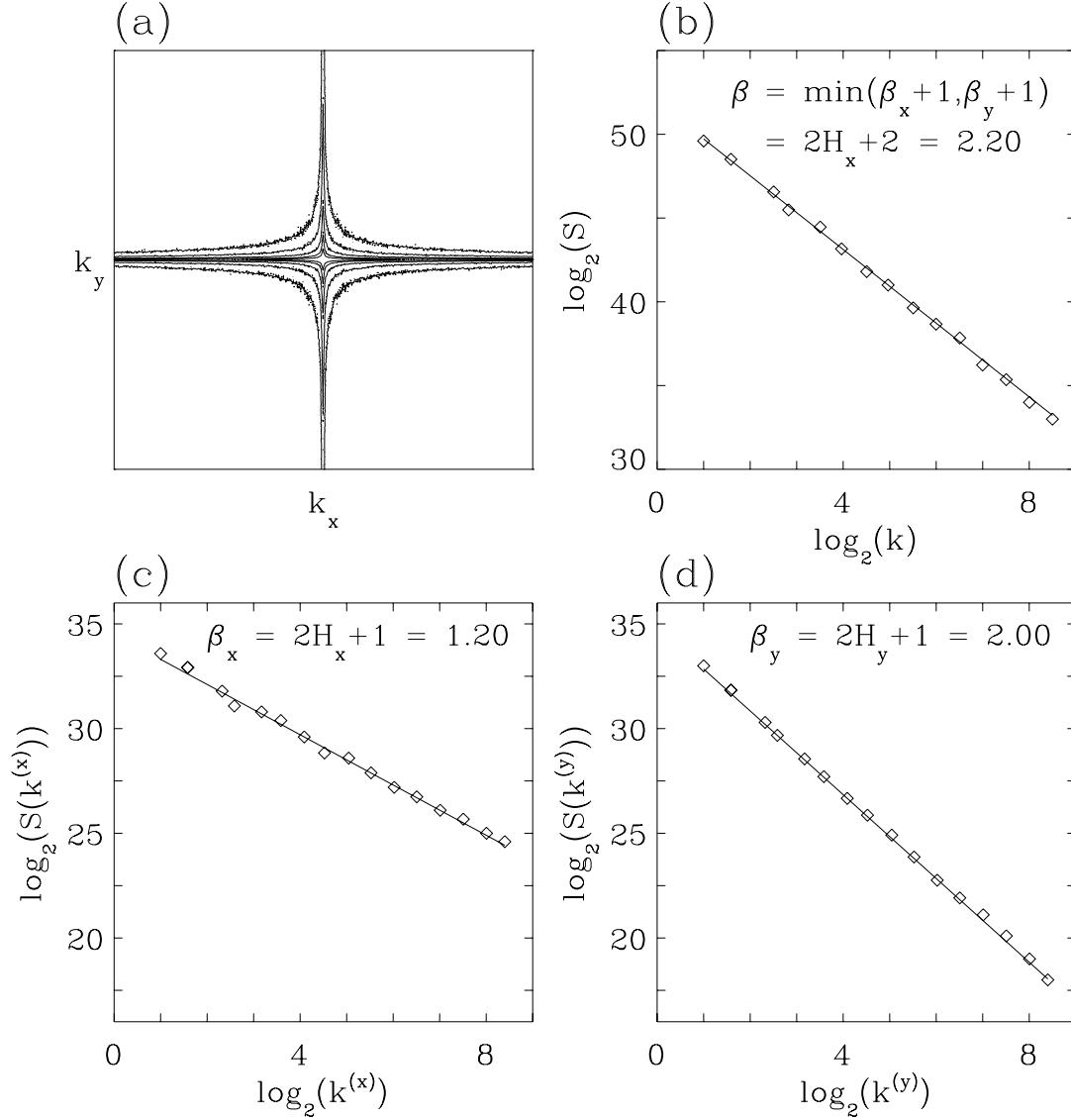


Fig. 9.— Fourier analysis of the  $512 \times 512$  central parts of 32 ( $1024 \times 1024$ ) synthetic anisotropic fBs surfaces  $B_{H_x=0.10, H_y=0.50}(\mathbf{x})$ . (a) Contour plots of  $\ln|\hat{B}_{H_x=0.10, H_y=0.50}(\mathbf{k})|$ . (b) The power spectrum  $S(|\mathbf{k}|)$  vs  $|\mathbf{k}|$  in a logarithmic representation. (c) The averaged power spectrum of the one-dimensional  $x$ -cuts. (d) The averaged power spectrum of the one-dimensional  $y$ -cuts. The solid lines in (b), (c), and (d) correspond to the power-law theoretical predictions  $\beta = 2 \min(H_x, H_y) + 2$ ,  $\beta_x = 2H_x + 1$ ,  $\beta_y = 2H_y + 1$  respectively.

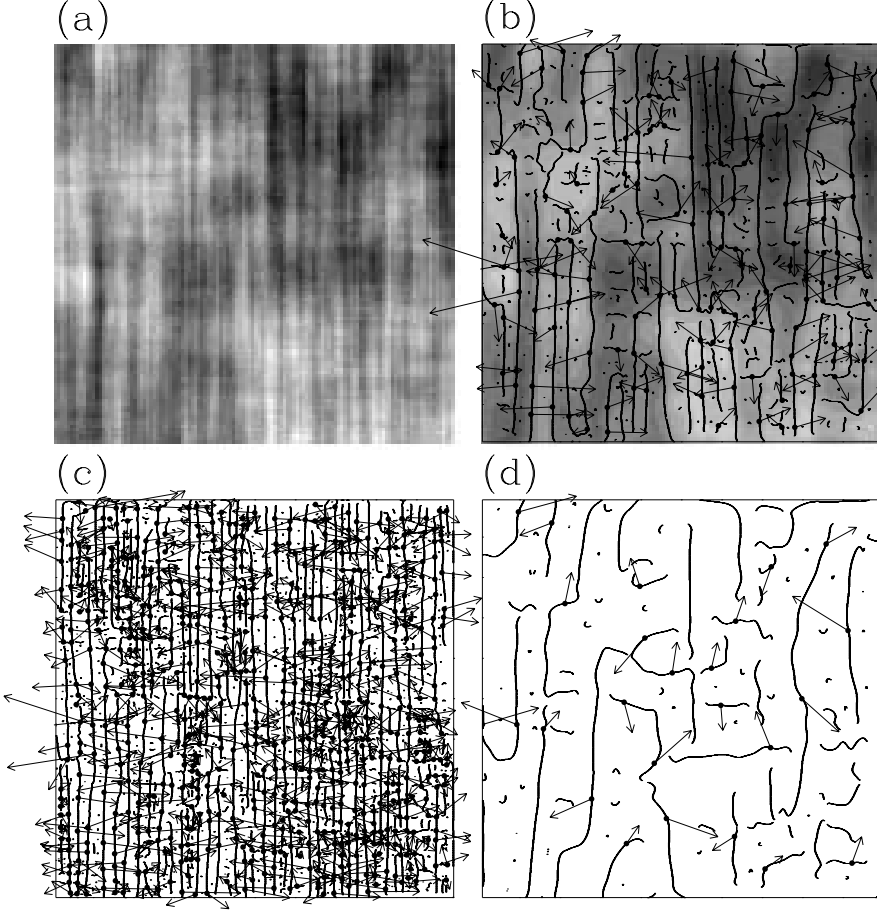


Fig. 10.— 2D wavelet transform analysis of  $B_{H_x=0.10, H_y=0.50}(\mathbf{x})$ .  $\psi$  is the first-order radially symmetric analyzing function shown in Figures 2a and 2b. (a) 32 grey-scale coding of the original image. In (b)  $a = 2^{2.9}\sigma_W$ , (c)  $a = 2^{1.9}\sigma_W$  and (d)  $a = 2^{3.9}\sigma_W$  ( $\sigma_W = 13$  pixels), are shown the maxima chains; the local maxima of  $\mathcal{M}_\psi$  along these chains are indicated by ( $\bullet$ ) from which originate an arrow whose length is proportional to  $\mathcal{M}_\psi$  and its direction (with respect to the  $x$ -axis) is given by  $\mathcal{A}_\psi$ . In (b), the smoothed image  $\phi_{\mathbf{b},a} * B_{H_x=0.10, H_y=0.50}$  is shown as a grey-scale coded background from white (min) to black (max).

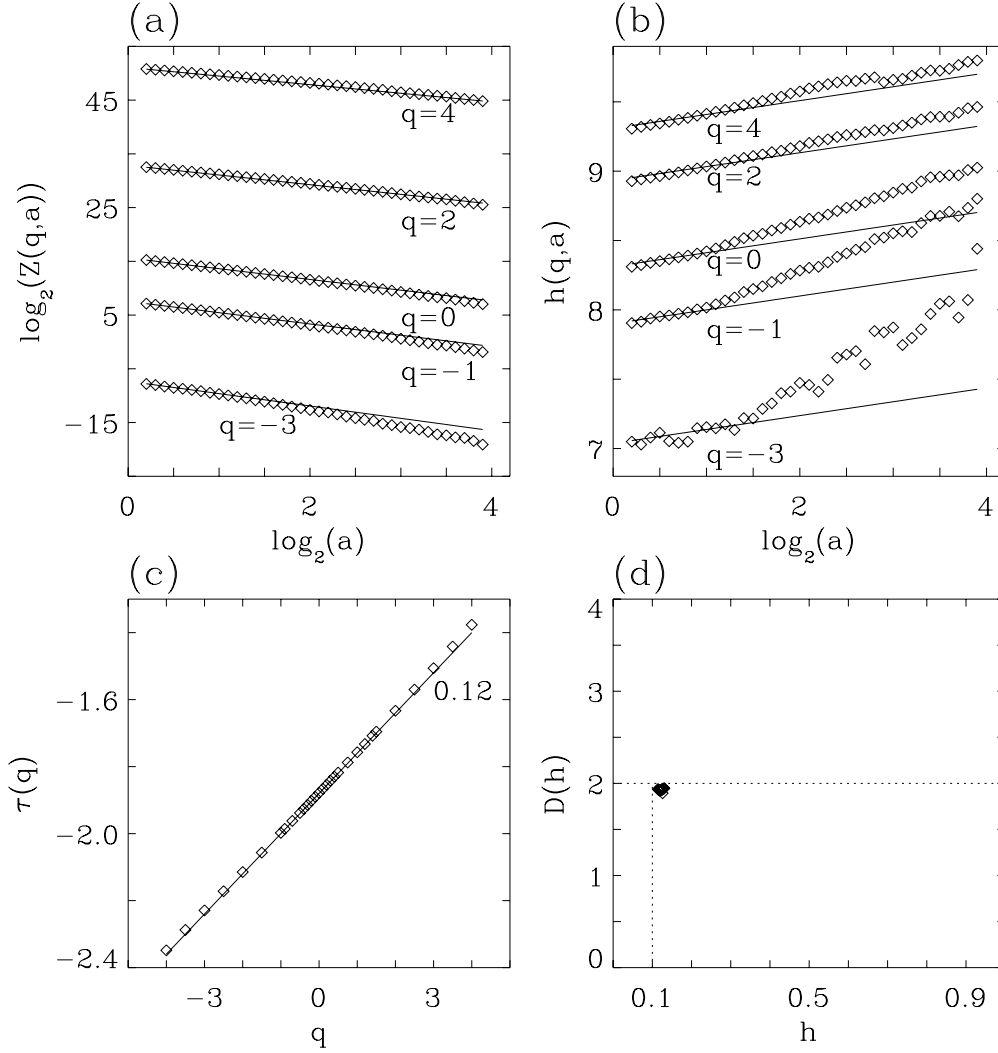


Fig. 11.— Determination of the  $\tau(q)$  and  $D(h)$  spectra of the fBs  $B_{H_x=0.10, H_y=0.50}(\mathbf{x})$  with the 2D WTMM method. (a)  $\log_2 \mathcal{Z}(q, a)$  vs  $\log_2 a$ ; the solid lines correspond to the theoretical predictions  $\tau(q) = qH - 2$  (Eq. (30)) with  $H = \min(H_x, H_y) = 0.10$ . (b)  $h(q, a)$  vs  $\log_2 a$ ; the solid lines correspond to the theoretical slope  $H = \min(H_x, H_y) = 0.10$ . (c)  $\tau(q)$  vs  $q$ ; the solid line corresponds to a linear regression fit estimate of  $H$ . (d)  $D(h)$  vs  $h$  as obtained from the scaling behavior of  $h(q, a)$  and  $D(q, a)$  vs  $\log_2 a$  (Eqs. (20) and (21)). These results correspond to an averaging over 32 ( $1024 \times 1024$ ) synthetic rough surfaces. The analyzing wavelet is the radially isotropic first-order analyzing wavelet (Figs. 2a and 2b);  $a$  is expressed in  $\sigma_W = 13$  units.

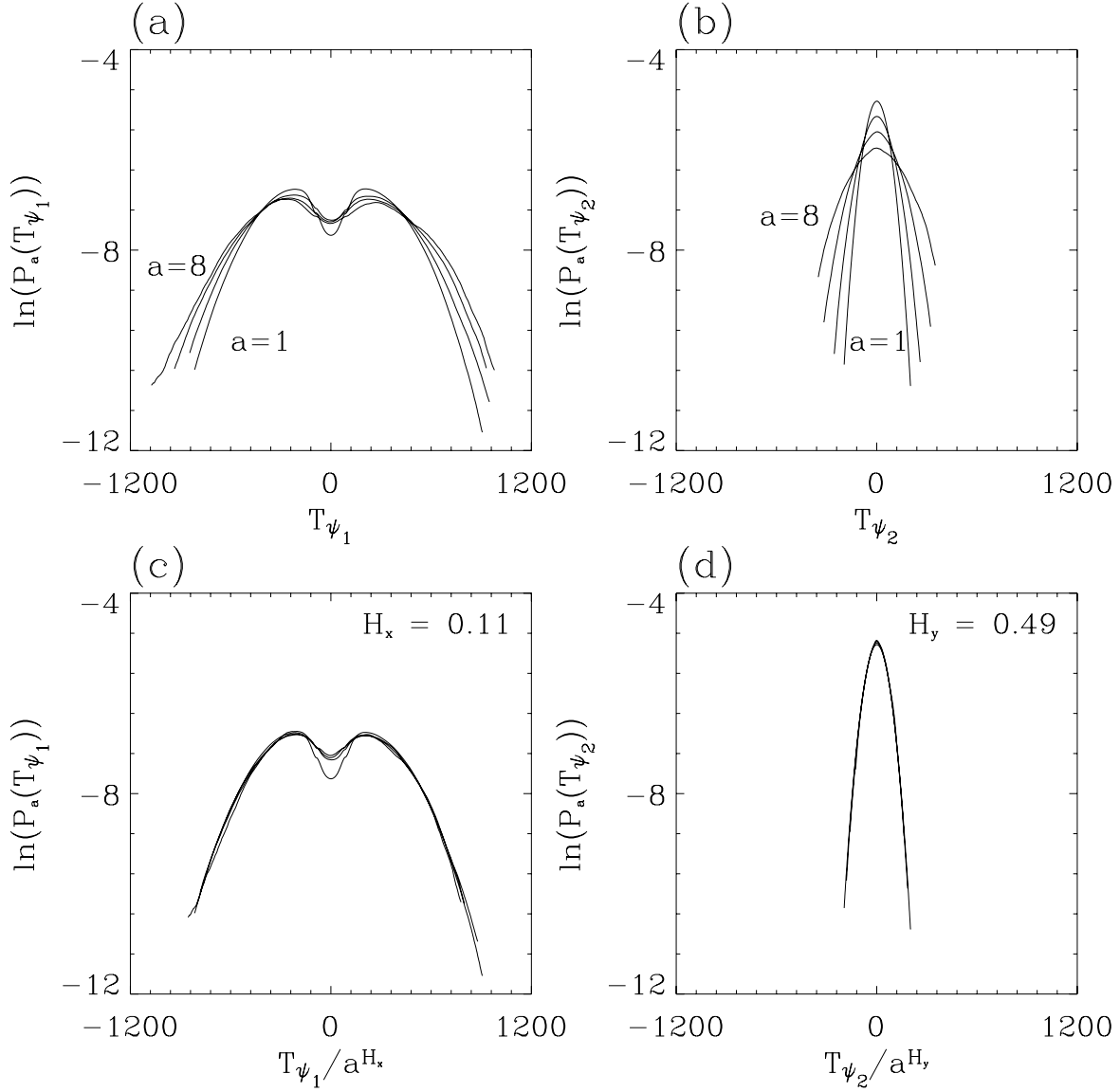


Fig. 12.— Pdfs of the  $x$  and  $y$  components of the WTMMM coefficients of  $B_{H_x=0.10, H_y=0.50}(\mathbf{x})$  as computed with the first-order wavelet at the scales  $a = 1, 2, 4,$  and  $8$  (in  $\sigma_W = 13$  units). (a)  $\ln(P_a(T_{\psi_1}))$  vs  $T_{\psi_1}$ ; (b)  $\ln(P_a(T_{\psi_2}))$  vs  $T_{\psi_2}$ . In (c) and (d),  $T_{\psi_1}$  and  $T_{\psi_2}$  are rescaled by  $a^{H_x}$  and  $a^{H_y}$  with  $H_x = 0.11$  and  $H_y = 0.49$  respectively.

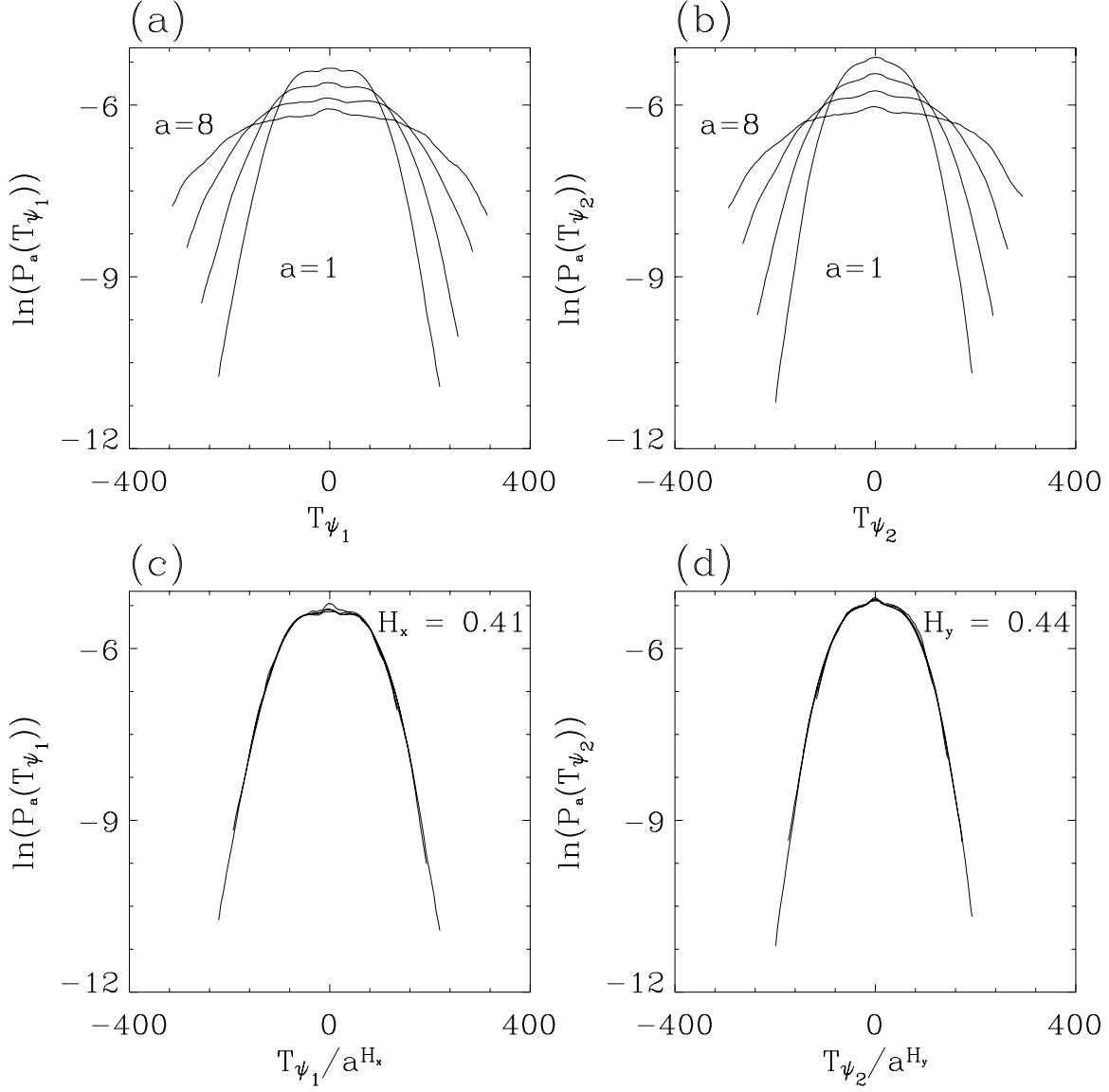


Fig. 13.— Pdfs of the  $x$  and  $y$  components of the WTMMM coefficients of  $B_{H_x=0.41, H_y=0.44}(\mathbf{x})$  as computed with the first-order wavelet at the scales  $a = 1, 2, 4$ , and  $8$  (in  $\sigma_W = 13$  units). (a)  $\ln(P_a(T_{\psi_1}))$  vs  $T_{\psi_1}$ ; (b)  $\ln(P_a(T_{\psi_2}))$  vs  $T_{\psi_2}$ . In (c) and (d),  $T_{\psi_1}$  and  $T_{\psi_2}$  are rescaled by  $a^{H_x}$  and  $a^{H_y}$  with  $H_x = 0.41$  and  $H_y = 0.44$  respectively.

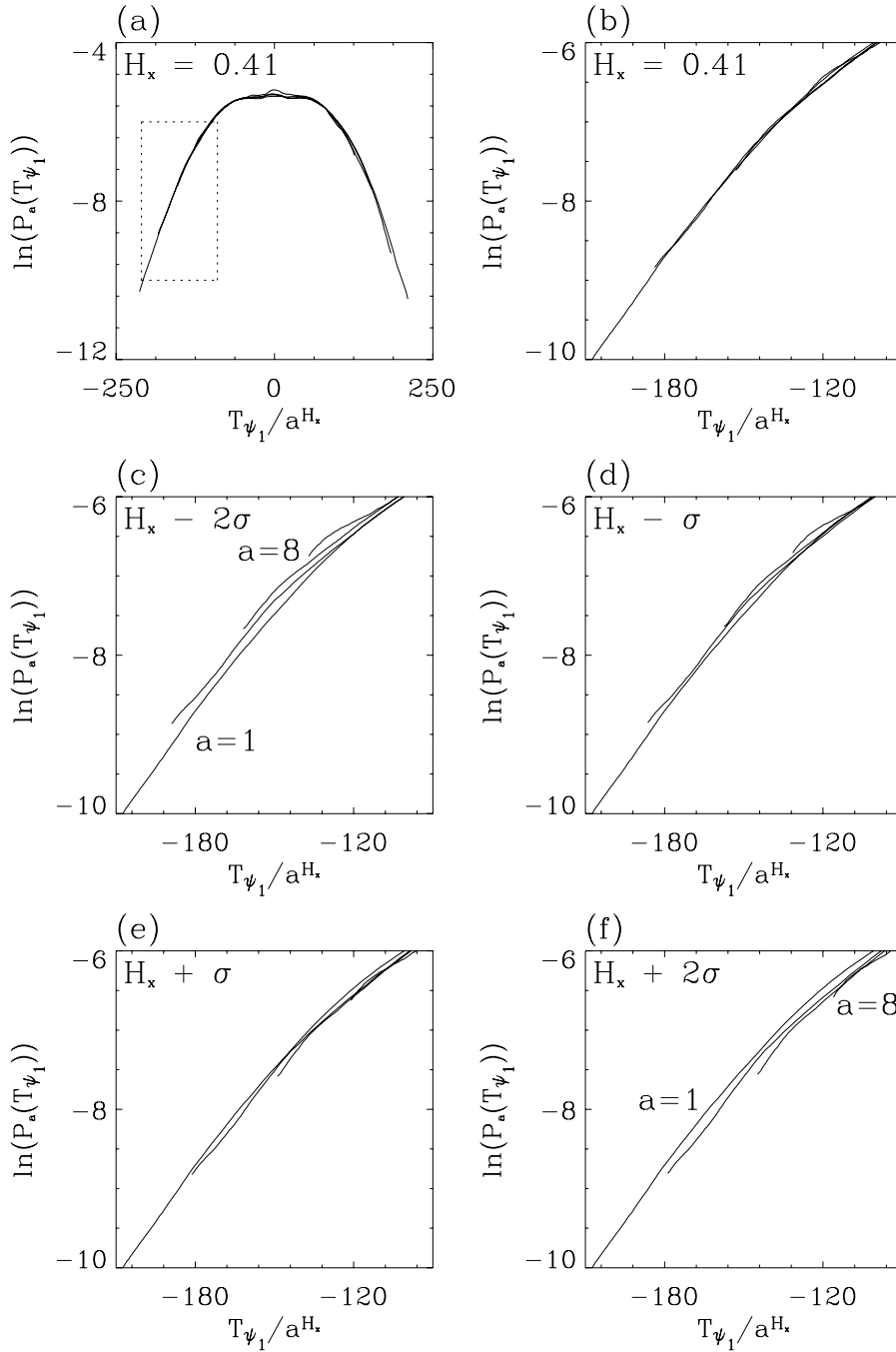


Fig. 14.— Rescaled pdfs of the  $x$  components of the WTMM coefficients of  $B_{H_x=0.41, H_y=0.44}(\mathbf{x})$  as computed with the first-order wavelet at the scales  $a = 1, 2, 4,$  and  $8$  (in  $\sigma_W = 13$  units). Figure 13c is reported in (a). (b) is a zoom-in corresponding to the dashed rectangle in (a). In (c)-(f),  $T_{\psi_1}$  is rescaled with neighboring values of  $H_x$ , namely  $H_x - 2\sigma, H_x - \sigma, H_x + \sigma,$  and  $H_x + 2\sigma$ , with  $\sigma = 0.01$ .

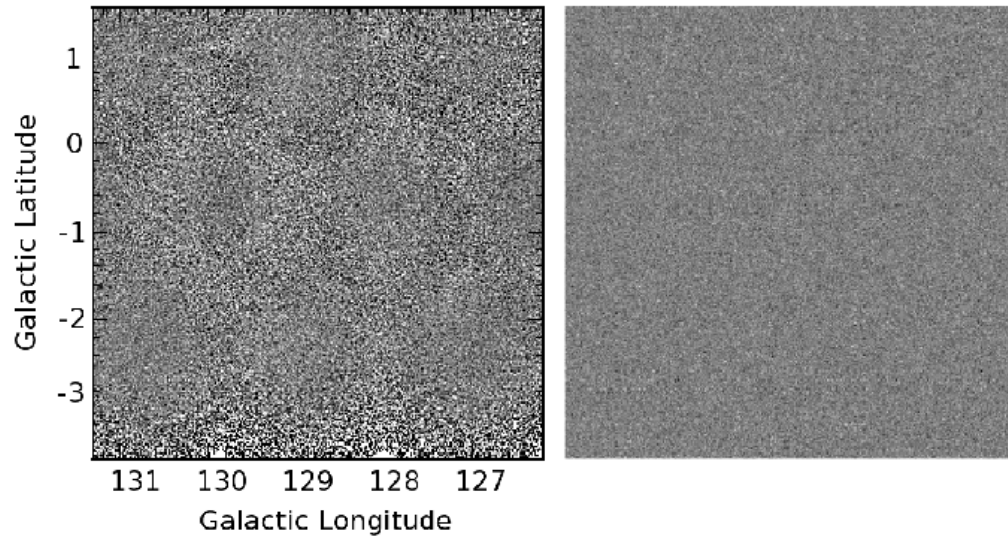


Fig. 15.—  $512 \times 512$  sample noise images. DRAO noise (left); Synthetic noise (right).

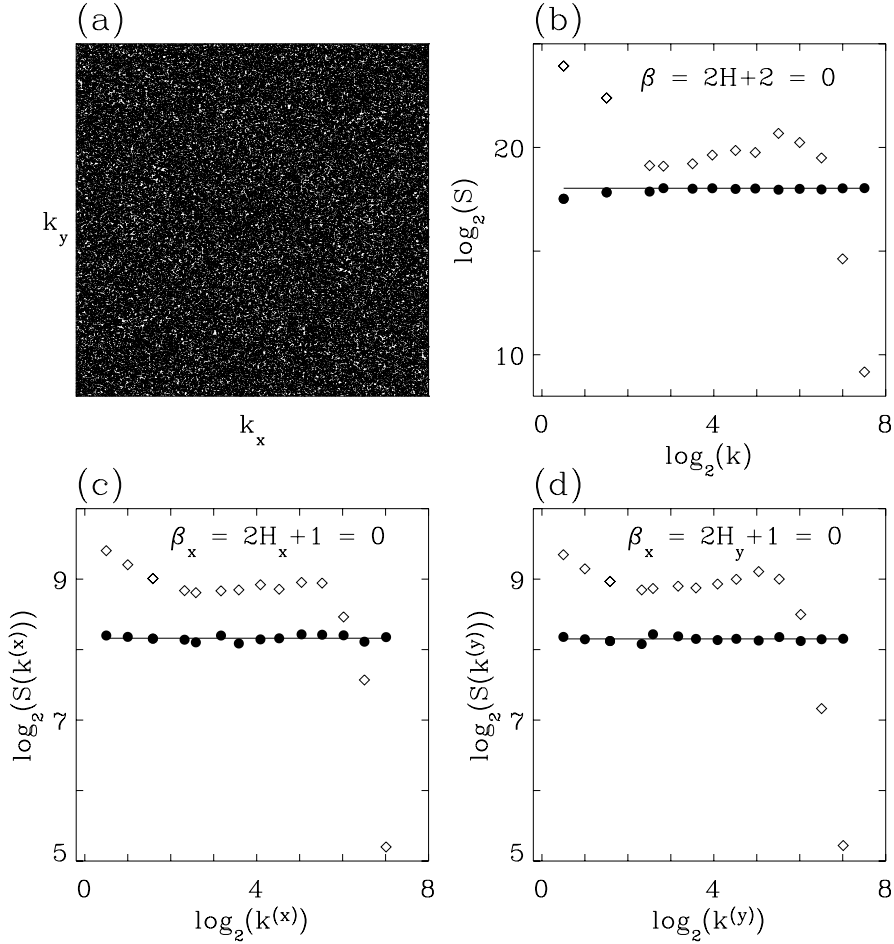


Fig. 16.— Fourier analysis of the  $512 \times 512$  central part of the DRAO ( $\diamond$ ) and synthetic ( $\bullet$ ) noise surfaces. (a) A contour plot of the Fourier transform of a synthetic noise surface. (b) The power spectra  $S(|\mathbf{k}|)$  vs  $|\mathbf{k}|$  in a logarithmic representation. (c) The averaged power spectra of the one-dimensional  $x$ -cuts. (d) The averaged power spectra of the one-dimensional  $y$ -cuts. The solid lines correspond to the power-law theoretical predictions for the synthetic noise. These results correspond to an averaging over 16 surfaces (instead of the usual 32).

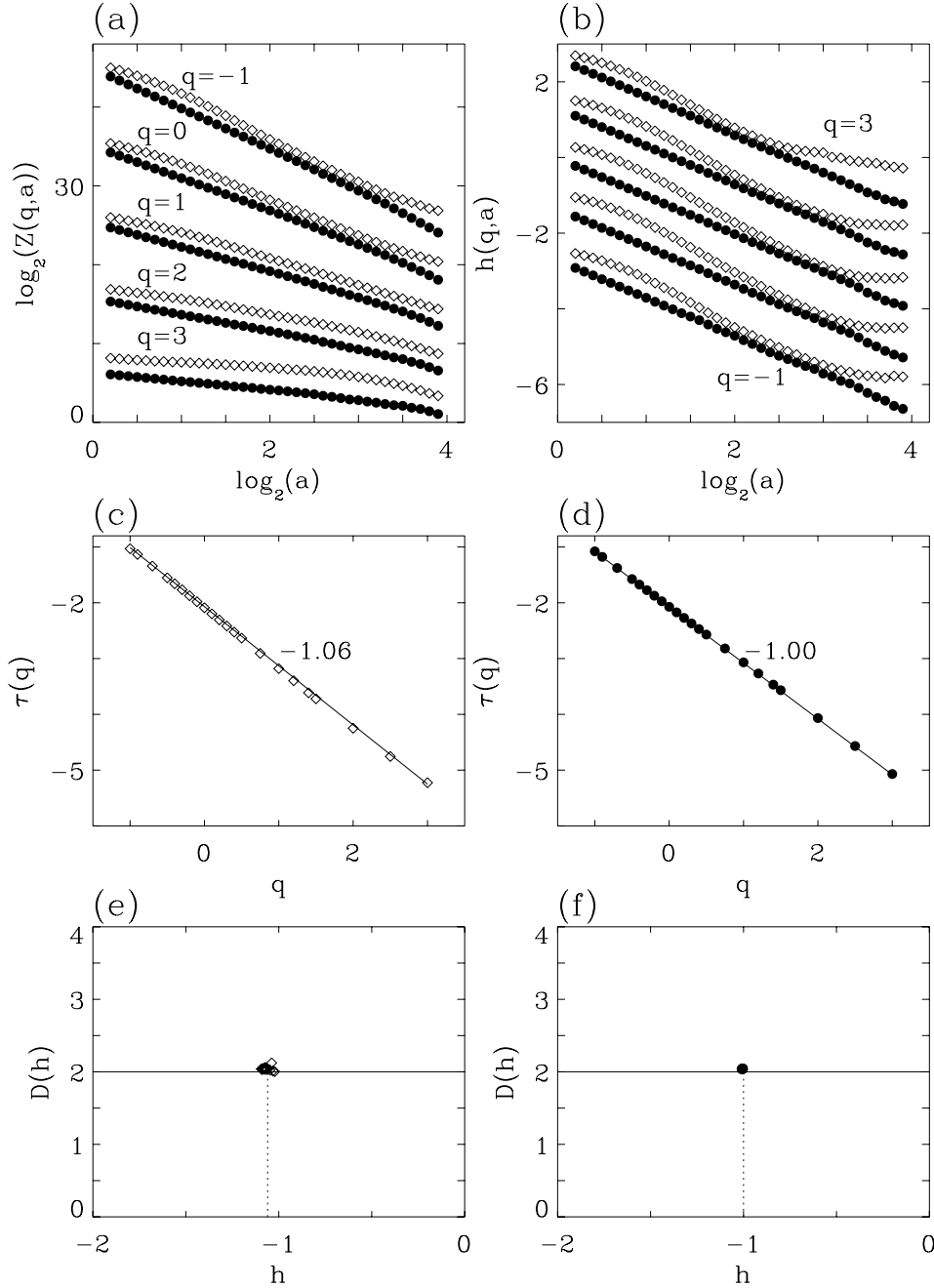


Fig. 17.— Determination of the  $\tau(q)$  and  $D(h)$  spectra of the DRAO ( $\diamond$ ) and synthetic ( $\bullet$ ) noise mosaics with the 2D WTMM method. (a)  $\log_2 \mathcal{Z}(q, a)$  vs  $\log_2 a$ . (b)  $h(q, a)$  vs  $\log_2 a$ .  $\tau(q)$  vs  $q$  for the DRAO (c) and synthetic (d) noise surfaces; the solid lines corresponds to a linear regression fit estimate of  $H$ .  $D(h)$  vs  $h$  as obtained from the scaling behavior of  $D(q, a)$  vs  $\log_2 a$  (Eq. (21)) for the DRAO (e) and synthetic (f) noise surfaces. First-order analyzing wavelets. These results correspond to an averaging over 16 ( $1024 \times 1024$ ) surfaces.  $a$  is expressed in  $\sigma_W$  units, where  $\sigma_W = 13$  pixels.

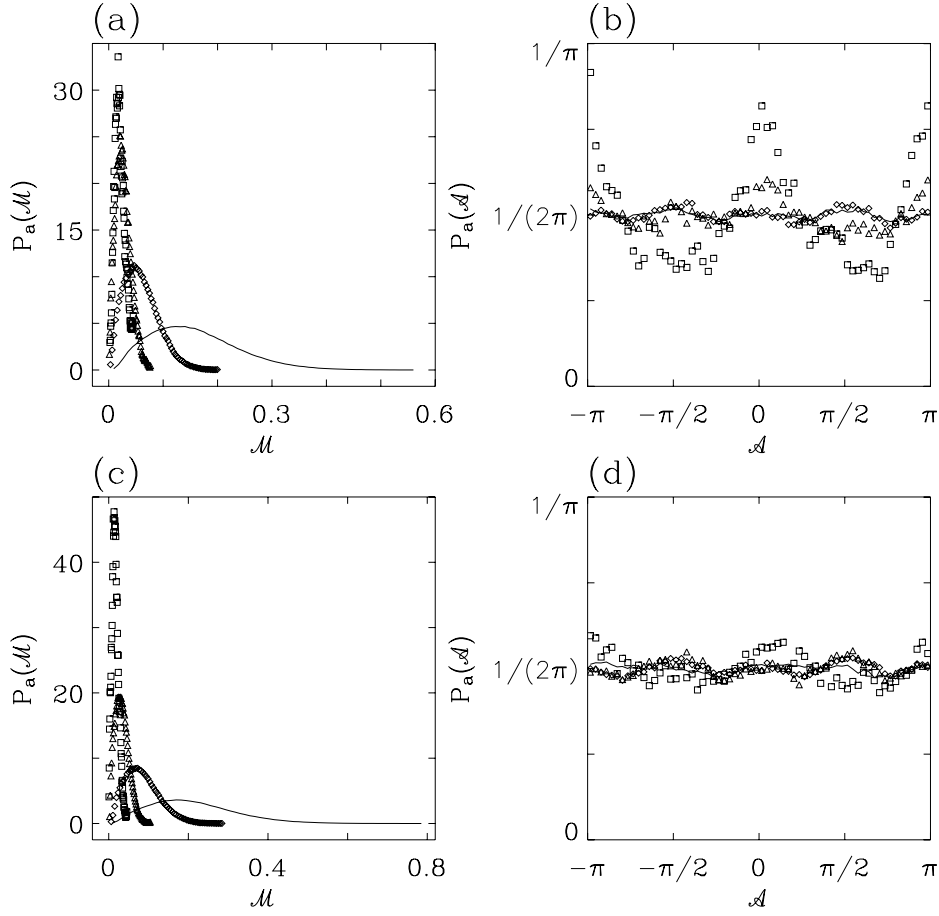


Fig. 18.— Pdfs of the WTMMM coefficients of the DRAO noise surfaces as computed at different scales  $a = 1$  (full line), 2 ( $\diamond$ ), 4 ( $\triangle$ ), 8 ( $\square$ ) (in  $\sigma_W = 13$  units). (a)  $P_a(\mathcal{M})$  vs  $\mathcal{M}$ . (b)  $P_a(\mathcal{A})$  vs  $\mathcal{A}$ ;  $\psi$  is the first-order analyzing wavelet. (c)  $P_a(\mathcal{M})$  vs  $\mathcal{M}$ . (d)  $P_a(\mathcal{A})$  vs  $\mathcal{A}$ ;  $\psi$  is the third-order analyzing wavelet. These results correspond to an averaging over 16 ( $1024 \times 1024$ ) surfaces.

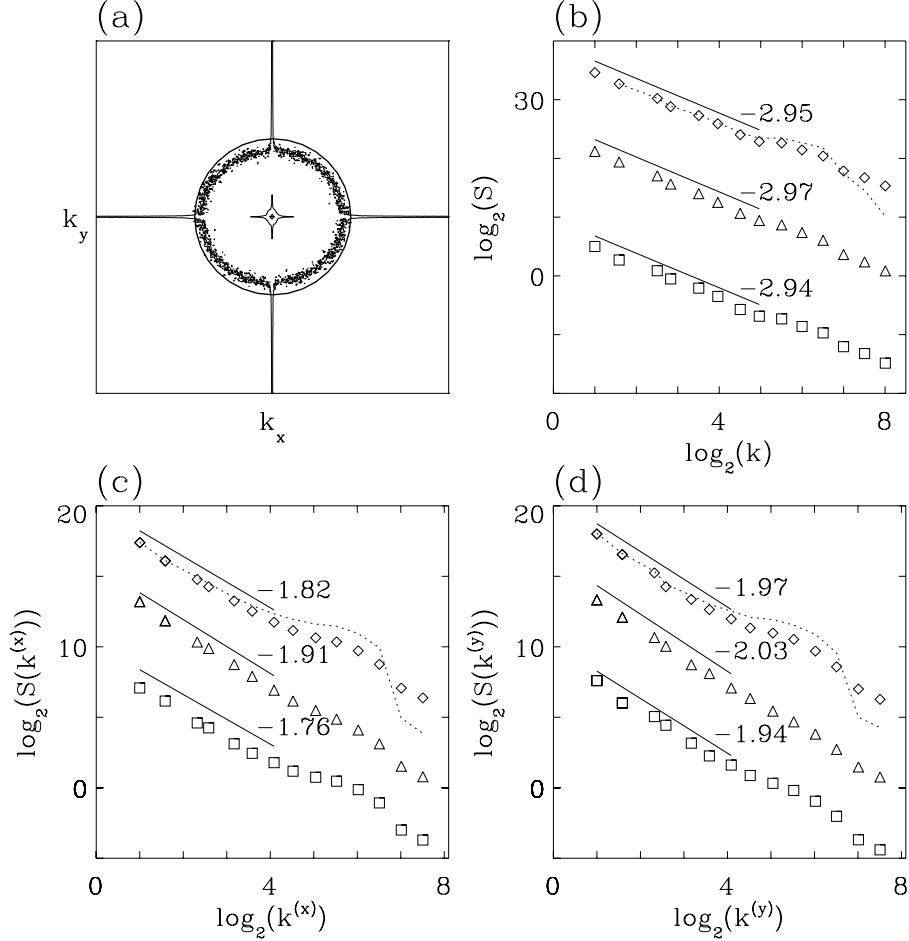


Fig. 19.— Fourier analysis of the Local ( $\diamond$ ), Perseus ( $\triangle$ ), and Outer ( $\square$ ) arm subregions. (a) Contour plots of the 2D Fourier transform of the Local subregions similar to Figure 4a, where a black circle was added to help the reader see the slight ellipticity of the contours. (b) The power spectrum  $S(|\mathbf{k}|)$  vs  $|\mathbf{k}|$  in a logarithmic representation; the solid lines correspond to power-law fits with exponents  $\beta = 2.95$  ( $\diamond$ ),  $2.97$  ( $\triangle$ ), and  $2.94$  ( $\square$ ). (c) The averaged power spectra of the one-dimensional  $x$ -cuts; the solid lines correspond to power-law fits with exponents  $\beta_x = 1.82$  ( $\diamond$ ),  $1.91$  ( $\triangle$ ), and  $1.76$  ( $\square$ ). (d) The averaged power spectra of the one-dimensional  $y$ -cuts; the solid lines correspond to power-law fits with exponents  $\beta_y = 1.97$  ( $\diamond$ ),  $2.03$  ( $\triangle$ ), and  $1.94$  ( $\square$ ). The dashed curves in (b), (c), and (d) represent the corresponding results obtained from the unfiltered data (Local arm). In (b), (c), and (d), the curves corresponding to the Perseus ( $\triangle$ ) and Outer ( $\square$ ) mosaics were shifted vertically.

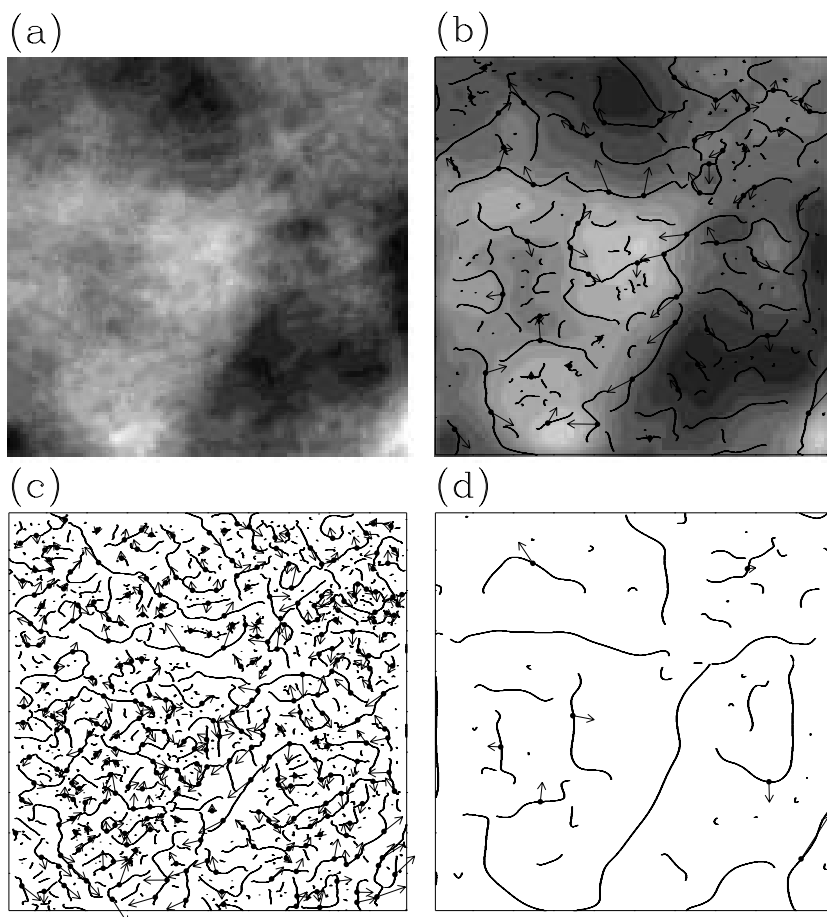


Fig. 20.— 2D wavelet transform analysis of one Local arm subregion.  $\psi$  is the first-order radially symmetric analyzing function shown in Figures 2a and 2b. (a) 32 grey-scale coding of the original image. In (b)  $a = 2^{2.9}\sigma_W$ , (c)  $a = 2^{1.9}\sigma_W$  and (d)  $a = 2^{3.9}\sigma_W$  ( $\sigma_W = 13$  pixels), are shown the maxima chains; the local maxima of  $\mathcal{M}_\psi$  along these chains are indicated by ( $\bullet$ ) from which originate an arrow whose length is proportional to  $\mathcal{M}_\psi$  and its direction (with respect to the  $x$ -axis) is given by  $\mathcal{A}_\psi$ . In (b), the smoothed image is shown as a grey-scale coded background from white (min) to black (max).

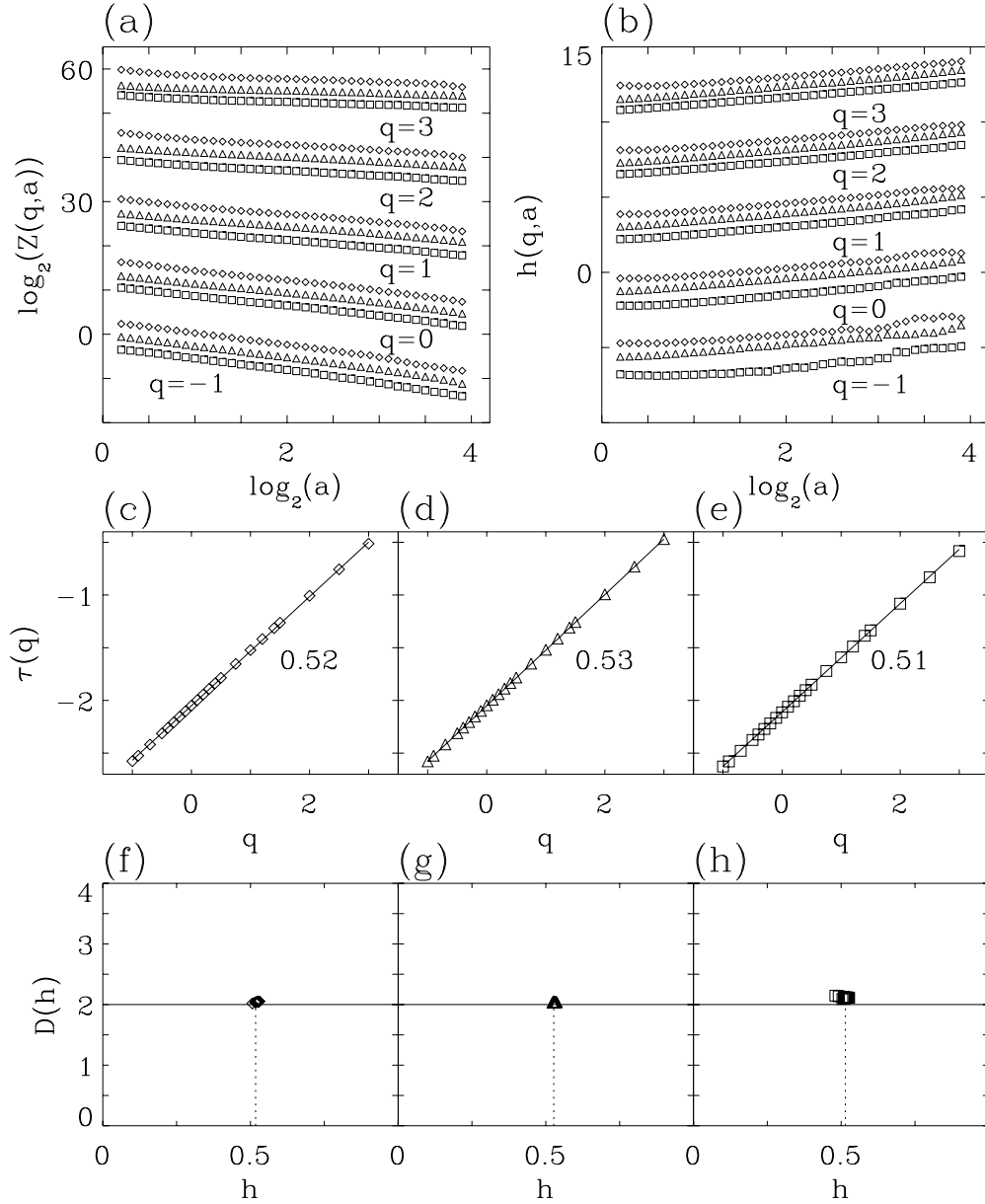


Fig. 21.— Determination of the  $\tau(q)$  and  $D(h)$  spectra of the Local ( $\diamond$ ), Perseus ( $\triangle$ ), and Outer ( $\square$ ) arm subregions with the 2D WTMM method. (a)  $\log_2 \mathcal{Z}(q, a)$  vs  $\log_2 a$ . (b)  $h(q, a)$  vs  $\log_2 a$ . (c)-(e)  $\tau(q)$  vs  $q$ ; the solid lines correspond to the linear spectrum  $\tau(q) = qH - 2$ , with  $H = 0.52$  ( $\diamond$ ),  $H = 0.53$  ( $\triangle$ ),  $H = 0.51$  ( $\square$ ). (f)-(h)  $D(h)$  vs  $h$  as obtained from the scaling behavior of  $h(q, a)$  and  $D(q, a)$  vs  $\log_2 a$  (Eqs. (20) and (21)); the vertical dashed lines correspond to the values of  $H$  found in (c), (d), and (e) respectively. These results correspond to an averaging over all subregions outlined in white in Figures 1a, 1c, and 1e respectively. The analyzing wavelet is the radially symmetric first-order analyzing wavelet (Figs. 2a and 2b).  $a$  is expressed in  $\sigma_W = 13$  units. In (a) and (b), all curves were shifted vertically.

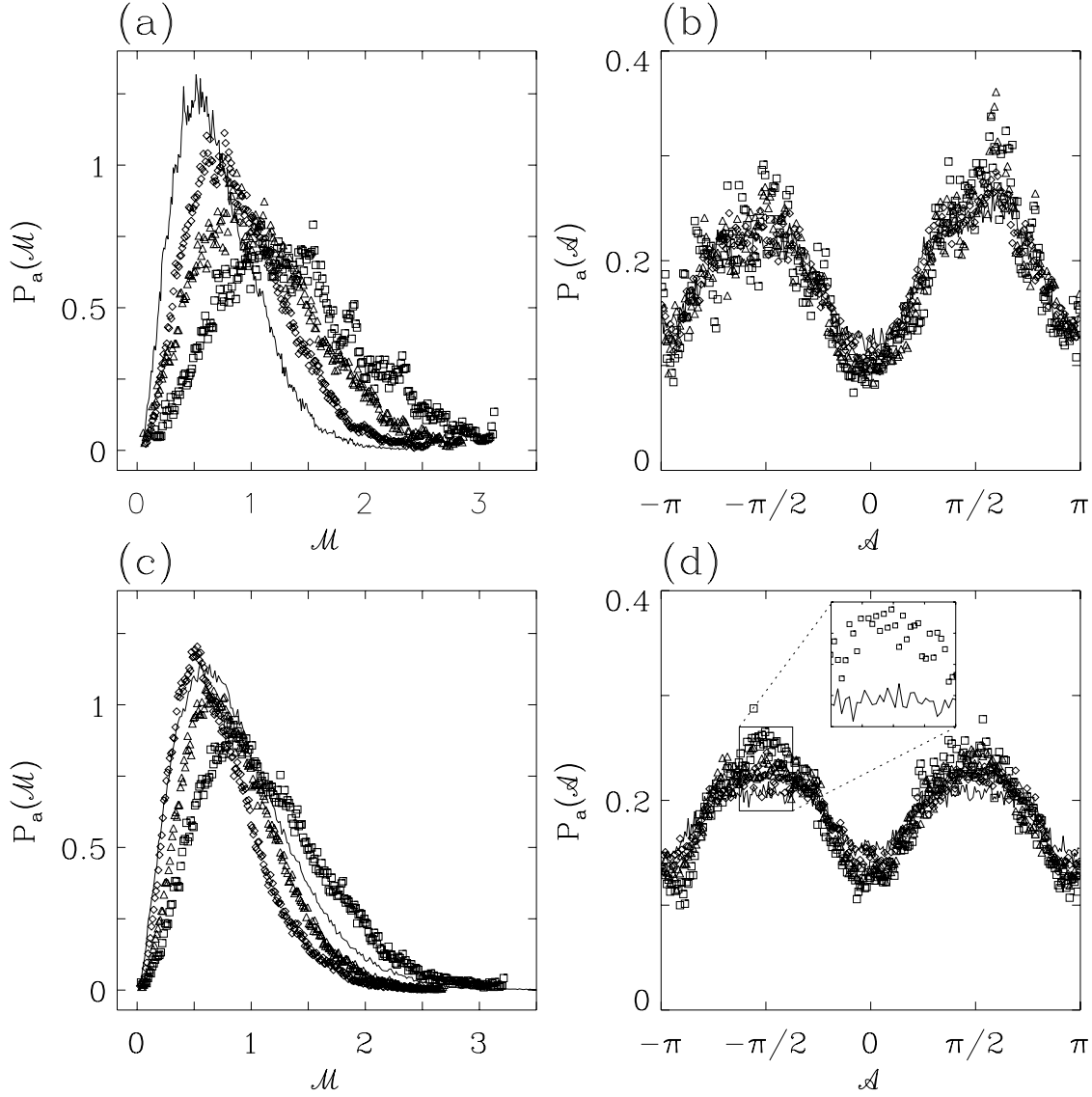


Fig. 22.— Pdfs of the WTMMM coefficients of the Local arm subregions as computed at different scales  $a = 2^{1.0}$  (full line),  $2^{1.5}$  ( $\diamond$ ),  $2^{2.0}$  ( $\triangle$ ),  $2^{2.5}$  ( $\square$ ) (in  $\sigma_W$  units, where  $\sigma_W = 13$  pixels). (a)  $P_a(\mathcal{M})$  vs  $\mathcal{M}$ ; (b)  $P_a(\mathcal{A})$  vs  $\mathcal{A}$ , where  $\psi$  is the first-order analyzing wavelet (Figs. 2a and 2b). (c)  $P_a(\mathcal{M})$  vs  $\mathcal{M}$ . (d)  $P_a(\mathcal{A})$  vs  $\mathcal{A}$ , where  $\psi$  is the third-order analyzing wavelet (Figs. 2c and 2d). These results correspond to an averaging over all subregions outlined in white in Figure 1a.

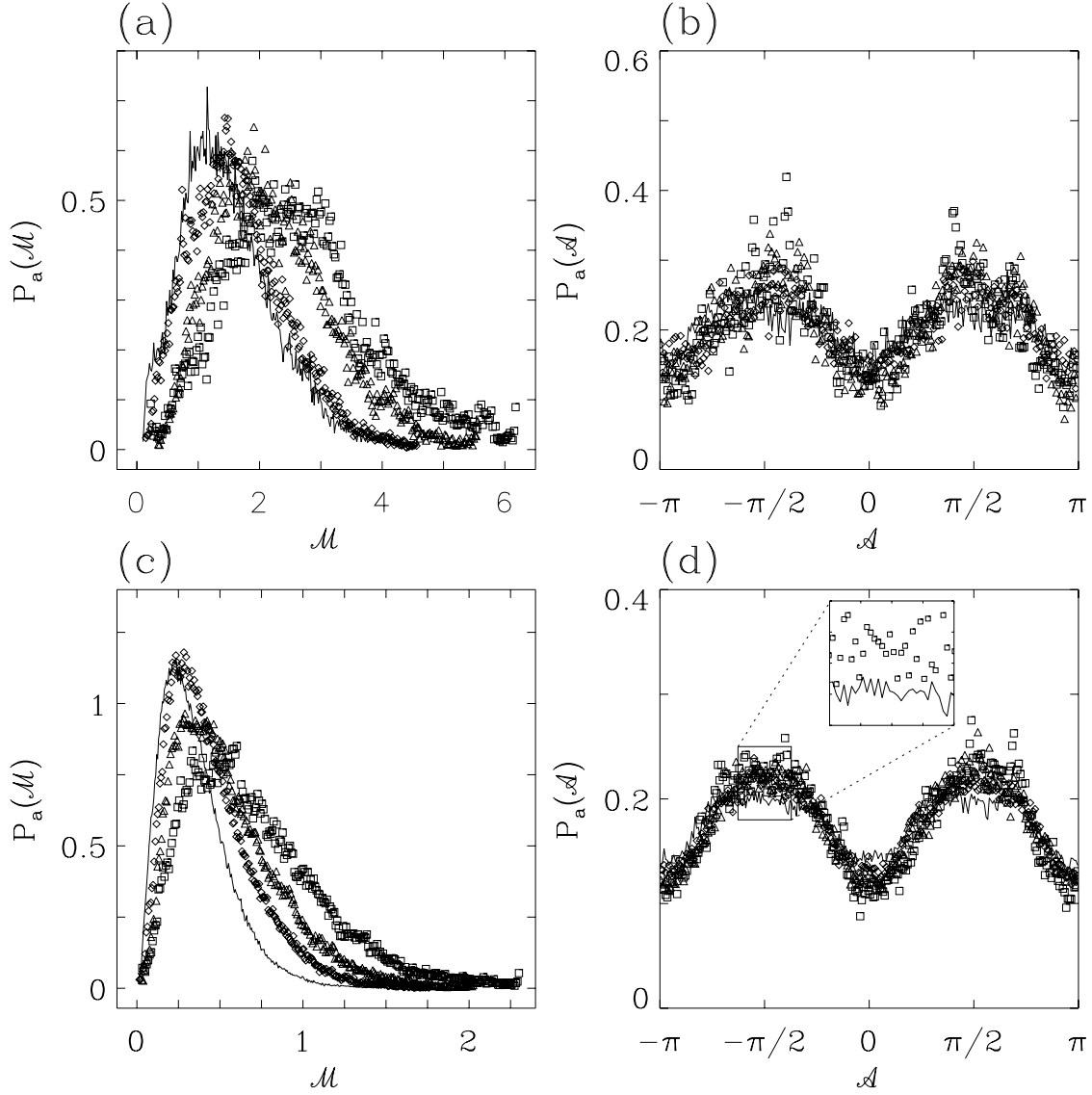


Fig. 23.— Pdfs of the WTMMM coefficients of the Perseus and Outer arm subregions as computed at different scales  $a = 2^{1.0}$  (full line),  $2^{1.5}$  ( $\diamond$ ),  $2^{2.0}$  ( $\triangle$ ),  $2^{2.5}$  ( $\square$ ) (in  $\sigma_W$  units). Perseus arm: (a)  $P_a(\mathcal{M})$  vs  $\mathcal{M}$ ; (b)  $P_a(\mathcal{A})$  vs  $\mathcal{A}$ . Outer arm: (c)  $P_a(\mathcal{M})$  vs  $\mathcal{M}$ . (d)  $P_a(\mathcal{A})$  vs  $\mathcal{A}$ , with the third-order analyzing wavelet (Figs. 2c and 2d). These results correspond to an averaging over all subregions outlined in white in Figures 1c and 1e respectively.

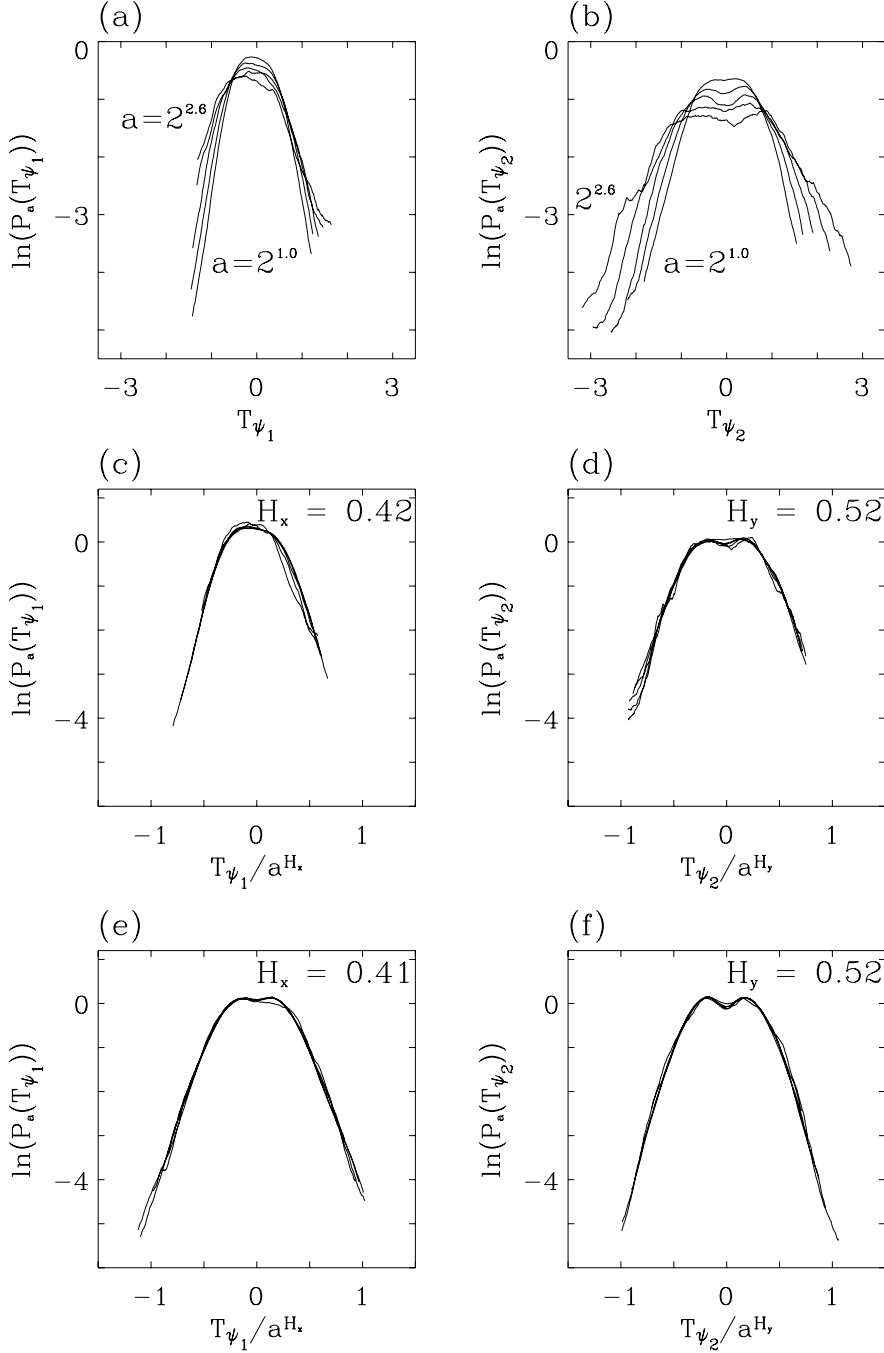


Fig. 24.— Pdfs of the  $x$  and  $y$  components of the WTMMM coefficients of the Local arm subregions as computed at the scales  $a = 2^{1.0}$ ,  $2^{1.4}$ ,  $2^{1.8}$ ,  $2^{2.2}$ , and  $2^{2.6}$  (in  $\sigma_W$  units, where  $\sigma_W = 13$  pixels). First-order analyzing wavelet: (a)  $\ln(P_a(T_{\psi_1}))$  vs  $T_{\psi_1}$ ; (b)  $\ln(P_a(T_{\psi_2}))$  vs  $T_{\psi_2}$ ; in (c) and (d),  $T_{\psi_1}$  and  $T_{\psi_2}$  are rescaled by  $a^{H_x}$  and  $a^{H_y}$  with  $H_x = 0.42$  and  $H_y = 0.52$  respectively. Third-order analyzing wavelet: (e) and (f),  $T_{\psi_1}$  and  $T_{\psi_2}$  are rescaled by  $a^{H_x}$  and  $a^{H_y}$  with  $H_x = 0.41$  and  $H_y = 0.52$  respectively.

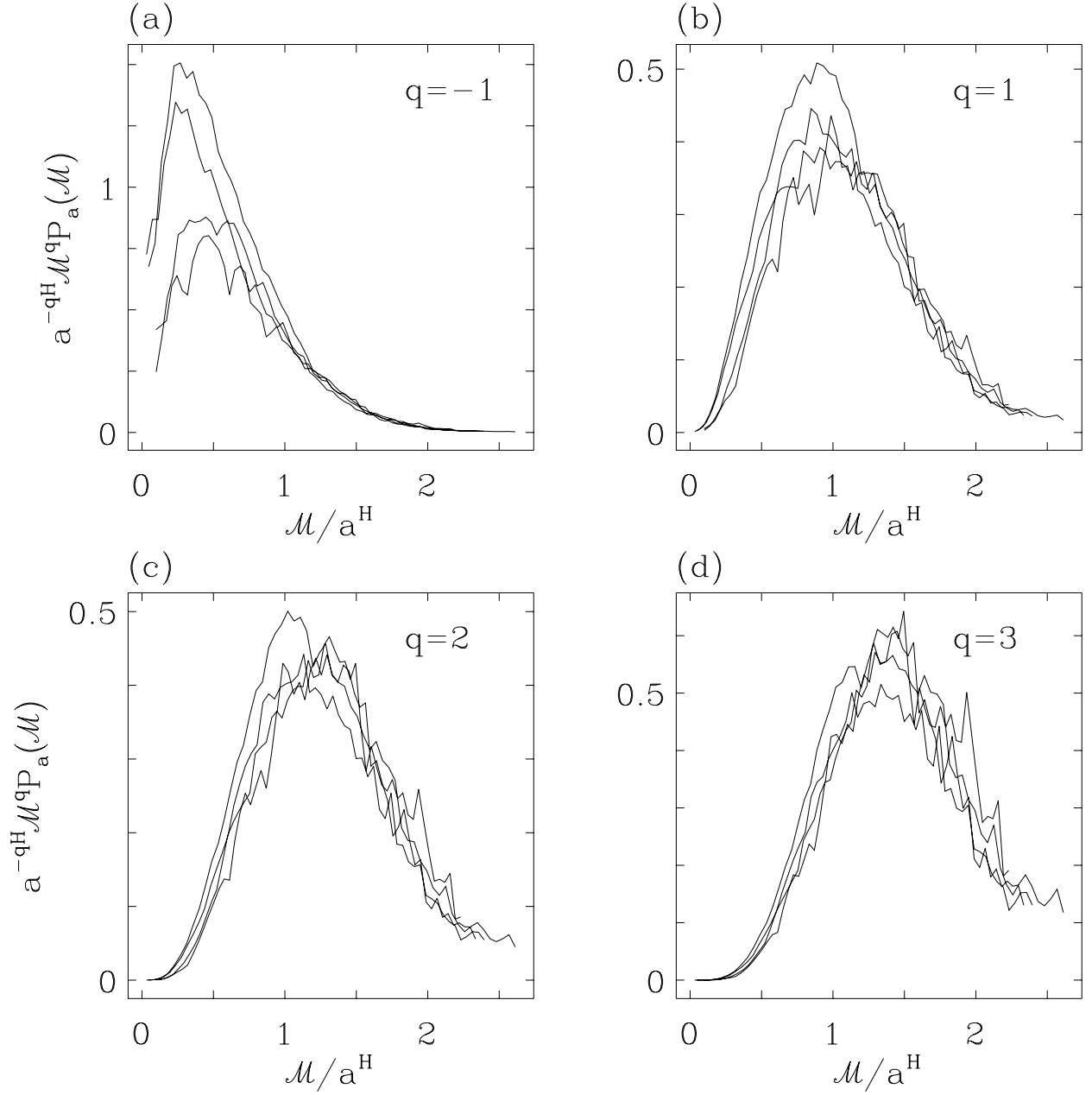


Fig. 25.— Pdfs of the WTMM coefficients for the Local arm mosaic as computed at different scales  $a = 2^{1.0}, 2^{1.5}, 2^{2.0}, 2^{2.5}$  (in  $\sigma_W = 13$  units).  $a^{-qH} \mathcal{M}^q P_a(\mathcal{M})$  vs  $\mathcal{M}/a^H$  for  $q = -1$  (a),  $q = 1$  (b),  $q = 2$  (c), and  $q = 3$  (d). Same 2D WTMM computations as in Figure 22.

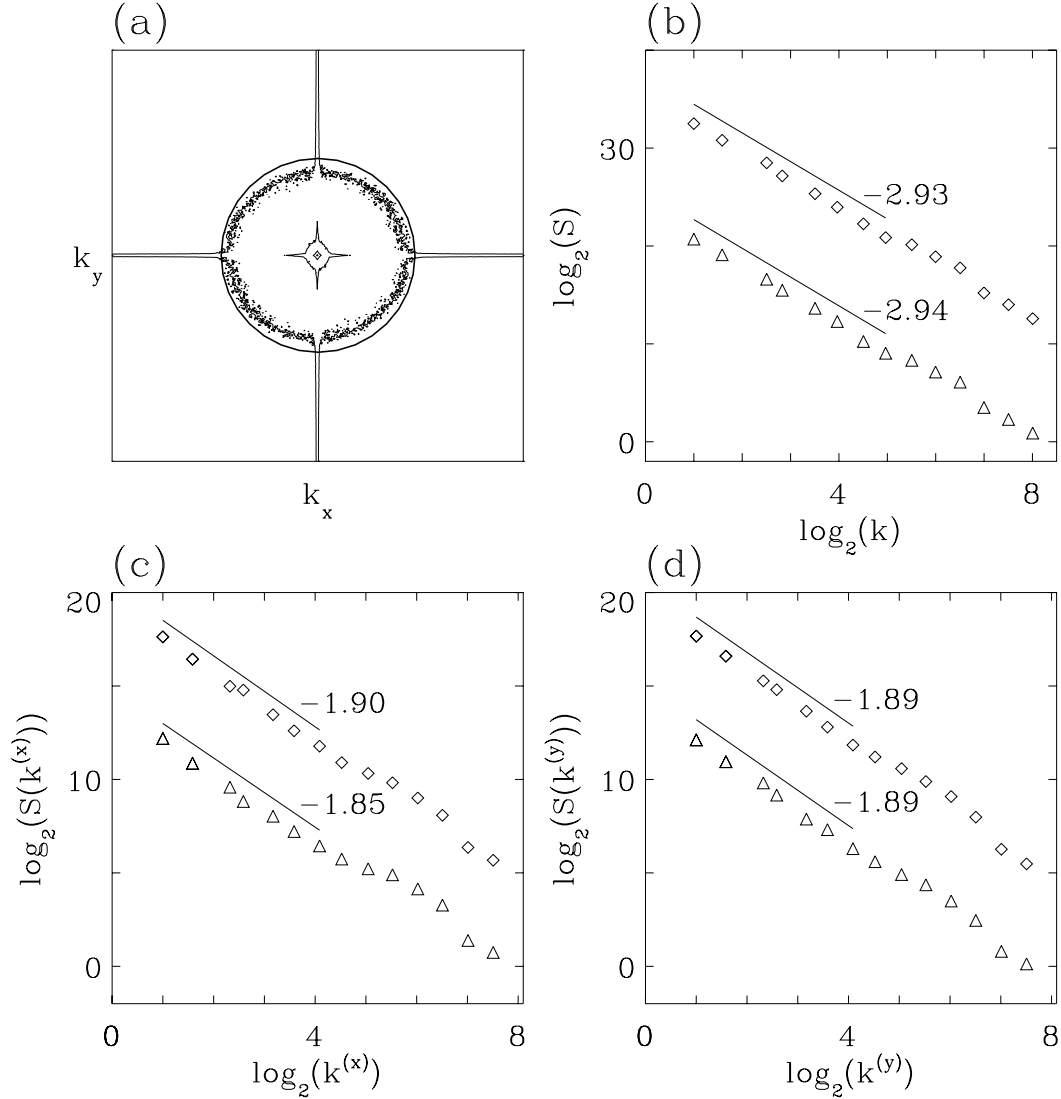


Fig. 26.— Fourier analysis of the Inter I ( $\diamond$ ) and Inter II ( $\triangle$ ) subregions. (a) Contour plots of the 2D Fourier transform of the Inter I subregions, where a black circle was added to help the reader see a slight ellipticity of the contour. (b) The power spectrum  $S(|\mathbf{k}|)$  vs  $|\mathbf{k}|$  in a logarithmic representation; the solid lines correspond to power-law fits with exponents  $\beta = 2.93$  ( $\diamond$ ) and  $2.94$  ( $\triangle$ ). (c) The averaged power spectrum of the one-dimensional  $x$ -cuts; the solid lines correspond to power-law fits with exponents  $\beta_x = 1.90$  ( $\diamond$ ) and  $1.85$  ( $\triangle$ ). (d) The averaged power spectrum of the one-dimensional  $y$ -cuts; the solid lines correspond to power-law fits with exponents  $\beta_y = 1.89$  ( $\diamond$ ) and  $1.89$  ( $\triangle$ ). In (b), (c), and (d), the curves corresponding to the Inter II subregions ( $\triangle$ ) were shifted vertically.

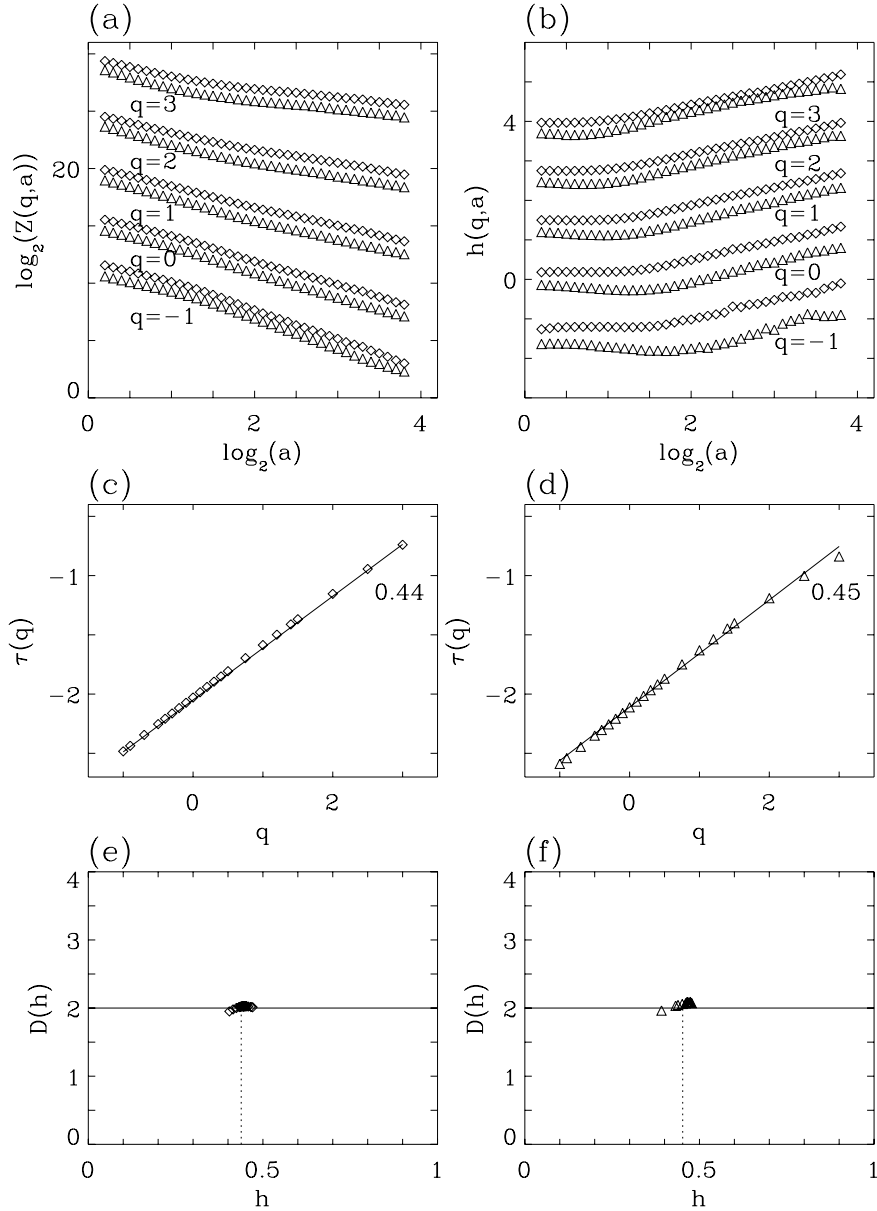


Fig. 27.— Determination of the  $\tau(q)$  and  $D(h)$  spectra of the Inter I ( $\diamond$ ) and Inter II ( $\triangle$ ) subregions with the 2D WTMM method. (a)  $\log_2 \mathcal{Z}(q, a)$  vs  $\log_2 a$ ; (b)  $h(q, a)$  vs  $\log_2 a$ . (c, d)  $\tau(q)$  vs  $q$ ; the solid lines correspond to the linear spectrum  $\tau(q) = qH - 2$ , with  $H = 0.44$  ( $\diamond$ ) and  $0.45$  ( $\triangle$ ). (e, f)  $D(h)$  vs  $h$  as obtained from the scaling behavior of  $h(q, a)$  and  $D(q, a)$  vs  $\log_2 a$  (Eqs. (20) and (21)); the vertical dashed lines correspond to the values of  $H$  found in (c) and (d) respectively. These results correspond to an averaging over all subregions outlined in white in Figures 1b and 1d. The analyzing wavelet is the radially symmetric first-order analyzing wavelet;  $a$  is expressed in  $\sigma_W = 13$  units. In (a) and (b), all curves were shifted vertically.

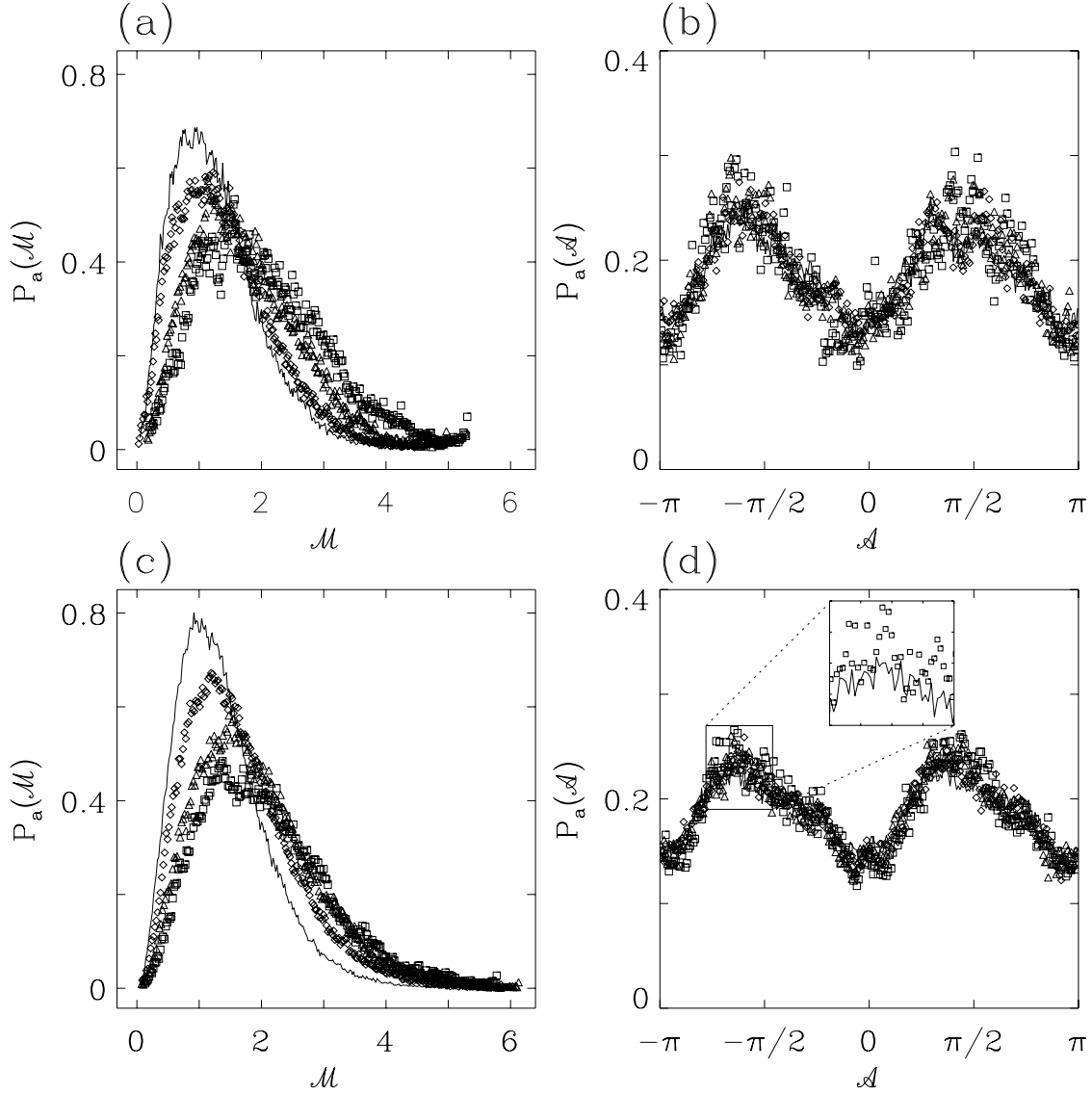


Fig. 28.— Pdfs of the WTMM coefficients of the Inter I subregions as computed at different scales  $a = 2^{1.0}$  (full line),  $2^{1.5}$  ( $\diamond$ ),  $2^{2.0}$  ( $\triangle$ ),  $2^{2.5}$  ( $\square$ ) (in  $\sigma_W$  units, where  $\sigma_W = 13$  pixels). (a)  $P_a(\mathcal{M})$  vs  $\mathcal{M}$ ; (b)  $P_a(\mathcal{A})$  vs  $\mathcal{A}$ , where  $\psi$  is the first-order analyzing wavelet. (c)  $P_a(\mathcal{M})$  vs  $\mathcal{M}$ ; (d)  $P_a(\mathcal{A})$  vs  $\mathcal{A}$ , where  $\psi$  is the third-order analyzing wavelet. These results correspond to an averaging over all subregions outlined in white in Figure 1b.

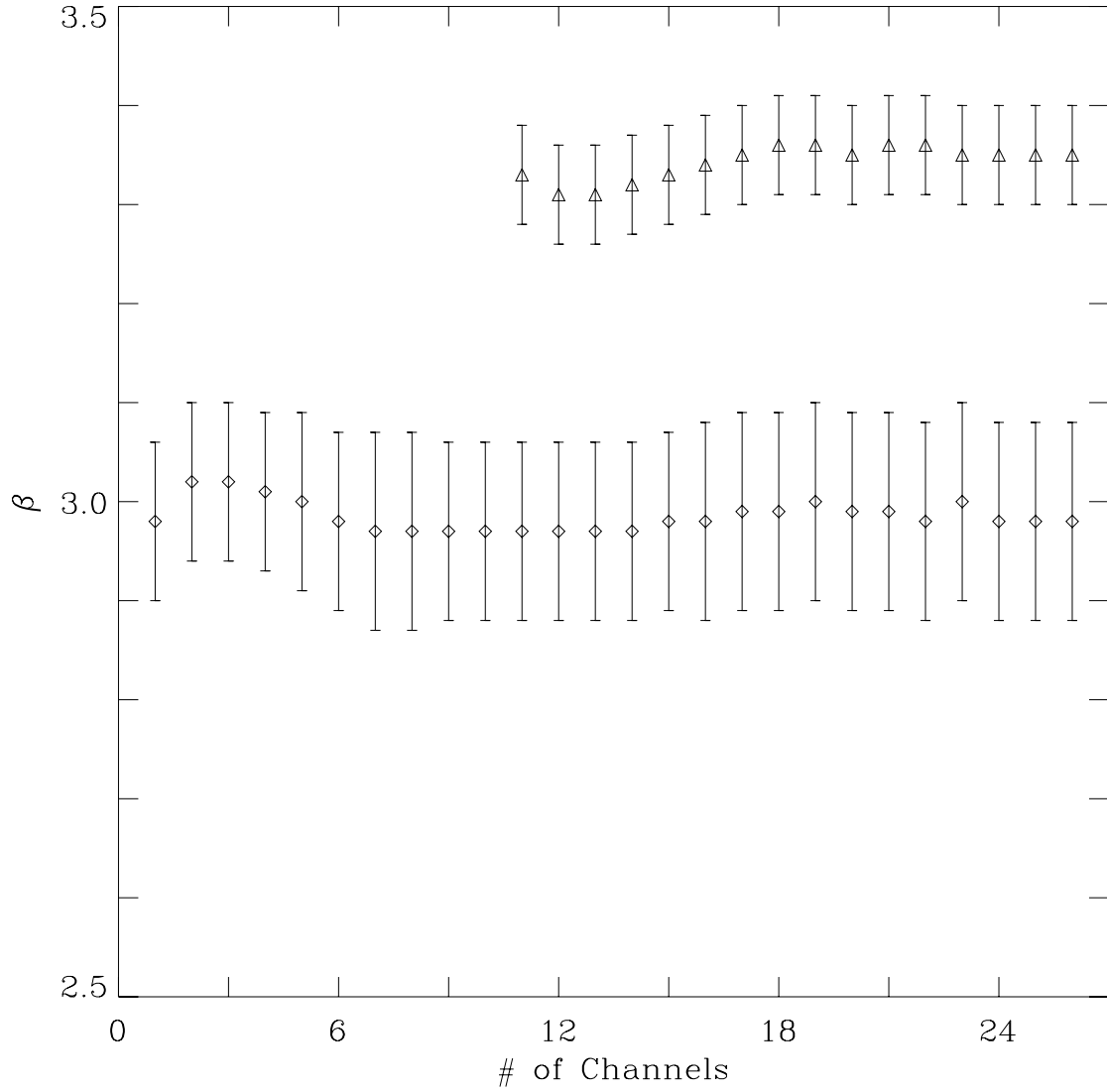


Fig. 29.— Power Spectral Indices as a Function of the Number of Velocity Channels for the Local Arm H I Mosaic over the range  $1 \lesssim \log_2(k) \lesssim 5$  ( $\diamond$ ) and  $1 \lesssim \log_2(k) \lesssim 4$  ( $\triangle$ ), where the latter values were shifted vertically.